HIGH-PRECISION MASS MEASUREMENT OF ^{38}Ca AND DEVELOPMENT OF THE LEBIT 9.4-T PENNING TRAP SYSTEM

By

Ryan Ringle

A DISSERTATION

Submitted to
Michigan State University
in partial fulfillment of the requirements
for the degree of

DOCTOR OF PHILOSOPHY

Department of Physics and Astronomy

2006

ABSTRACT

HIGH-PRECISION MASS MEASUREMENT OF ^{38}Ca AND DEVELOPMENT OF THE LEBIT 9.4-T PENNING TRAP SYSTEM

By

Ryan Ringle

The Low-Energy Beam and Ion Trap facility, LEBIT, has been designed to facilitate a variety of experiments at low energies with rare isotopes produced by fast-beam fragmentation. Gas stopping of the fast-fragment beams and modern ion manipulation techniques are used. The first experiments to be performed are high-precision mass measurements made possible with a 9.4 T Penning trap mass spectrometer. LEBIT has been commissioned and first experiments on stable and unstable nuclides have been performed. Here I present the results of a mass measurement on the unstable ^{38}Ca isotope, measured with a precision of better than δm/m=1×10^{-8}. ^{38}Ca was the first successful radioactive nuclide measured with LEBIT. It is of particular interest as it is a $0^+ \rightarrow 0^+$ emitter, which makes it a possible test candidate for the Conserved Vector Current (CVC) hypothesis [1].

Also presented are design and commissioning details of the 9.4 T Penning trap system and mass measurements of the stable krypton isotopes, ^{83,84}Kr, leading to improved mass values. In the interest of pushing the current limits of Penning trap mass spectrometry two new methods will be introduced. The first is a new excitation scheme of the ion motion using an octupolar radiofrequency field. The second, using the Lorentz steerer, is a fast preparation of ions previous to their capture in the Penning trap. Both methods have the potential to reduce the necessary measurement time, thus making high-precision measurements of shorter-lived species possible.

ACKNOWLEDGMENTS

To begin, I would like to offer my heartfelt gratitude to the NSCL at large. Without the assistance of all of the employees working here the completion of LEBIT could not have been realized. Making mass measurements of radioactive species is certainly not accomplished by one group, alone. Thank you so very much for running a world-class facility and offering the best support a researcher could ask for. You've made my time here pleasant and productive.

Next I would like to thank those in the design and machining departments who helped me to bring the LEBIT Penning trap from conception to reality. Thank you Don Lawton, Jim Moskalik, and Keith Leslie. Your exceptional efforts were integral to the success of the LEBIT program.

Thank you to the gas cell team, led by Prof. Dave Morrissey, for all of your efforts. Without the close collaboration of this group we would never have made a radioactive mass measurement.

I'd like to finish by acknowledging those I've worked closest to during my tenure at the NSCL. Although I was the first student on the LEBIT project (by two weeks, Pete!), the first generation LEBIT team expanded to three students (me, Peter Schury and Tao Sun) and a post-doc (Stefan Schwarz). By now you all feel like family to me. Thank you for your assistance and strong efforts. Without you I doubt that LEBIT would have been such a tremendous success in the timeframe we managed to squeeze it all into. I would also like to thank the next generation of LEBIT students (Josh, Amanda, Ania, and Greg) for (somewhat) gently removing me from the lab, thus

forcing me to write. I would like to offer special thanks to Prof. Georg Bollen, my advisor. Thank you for always making yourself available and involved. Your guidance and encouragement have meant more to me than I have words to express.

TABLE OF CONTENTS

LIST OF TABLES

LIST OF FIGURES

Images in this dissertation are presented in color.

CHAPTER 1

Introduction

High-precision mass measurements of short-lived, radioactive nuclides have an impact on various branches of nuclear physics, such as nuclear structure studies, the study of astrophysical nucleosynthesis, and the test of fundamental interactions.

One of the most important recent developments in mass spectrometry is the use of Penning traps. Penning traps, used for many years in mass spectrometry of stable charged particles, have proven themselves invaluable for their accuracy, efficiency and reliability [4]. For the study of short-lived, rare isotopes several Penning trap mass spectrometers have been installed at low-to-medium energy radioactive-beam facilities around the world. The Low Energy Beam and Ion Trap facility (LEBIT) at the National Superconducting Cyclotron Lab (NSCL) is the first to implement Penning trap mass spectrometry at a high-energy, rare-isotope facility using projectile fragmentation. In terms of reach far from the valley of stability this production mechanism provides advantages over lower-energy techniques.

1.1 Significance of nuclear mass measurements

One of the most fundamental properties of an atomic nucleus is its mass. Since it is simply defined as the sum of its constituent nucleons minus the binding energy,

measuring the mass of a nucleus essentially tells us how tightly the nucleons are bound, i.e., it serves as a probe of the total Hamiltonian of the nucleus.

Nuclear structure effects can be explored by the systematic measurement of nuclear masses. Shell effects distinguish themselves as a break in the smooth trend of nuclear binding energy as a function of the number of protons or neutrons. Near the valley of stability these closures happen at very specific magic numbers. Mass measurements provided the first evidence that nuclei outside of the valley show an evolution of shell structure, such as shell quenching and the emergence of new magic numbers. The first observance of such an effect was in 1975 in mass measurements on neutron rich sodium isotopes [5], giving the first indication of the erosion of the magicity at N = 20. This region of the nuclear chart is still of interest today.

As one moves toward the driplines on the chart of nuclides, the nuclei become more weakly bound, resulting in diffuse or halo nuclei [6]. Halo nuclei consist of a tightly-bound core and one or two loosely-bound valence nucleons whose wave functions extend out much further than those of the core. Measurements of neutron-rich lithium isotopes [5] provided the first experimental evidence of the loosely bound nature of these systems. To date, several light, neutron-rich nuclei have been found to possess halo ground states, such as ^{11}Li, ^{14}Be, and ^{6}He . Although these halo nuclei are short lived, the first two having half lives of $T_{1/2} < 10$ ms, they are not beyond of the reach of precision mass spectrometry [7] and future Penning trap mass measurements of these rare isotopes are planned.

Another interesting nuclear structure phenomenon that is currently under investigation is neutron-proton pairing, also associated with the so-called Wigner energy [8]. Even-even and odd-odd nuclei near the N = Z line of the chart of nuclides exhibit a cusp in the trend of binding energies. This effect is associated with an additional binding energy in nuclei in which protons and neutrons occupy the same nuclear shell. Some of the most recent LEBIT mass measurements in the $N \approx Z \approx 33$ [9] region

will contribute to these studies.

Isospin is a key concept in nuclear physics. With respect to the strong nuclear force, nuclear systems with the same isospin should have the same wavefunctions and energies. The Isobaric Multiplet Mass Equation (IMME), first introduced by Wigner [10] in 1957, predicts the mass excesses of each isobaric multiplet as a unique isospin-dependent function. High-precision mass measurements have been performed on multiplet isotopes to test the validity of this equation, and the improved ^{37}Ca mass value obtained with LEBIT [11] contributes to such tests.

High-precision mass measurements also play an important role in nuclear astrophysics. Stellar nucleosynthesis beyond the iron region, Z = 26, is carried out via neutron [12, 13] and proton [14] capture processes. The r process takes place on the very-neutron-rich side of the nuclear chart and synthesizes a heavier element by the capture of a neutron followed by a β^- decay. Proton capture occurs via the rp process and occurs on the proton-rich side of the nuclear chart. Here single protons are captured and followed by a subsequent β^+ decay, synthesizing a heavier isotope. Modeling these processes require neutron and proton separation energies, obtained from mass differences, as input parameters. Ideally the masses are obtained experimentally. In particular, in the case of the r process, which involves nuclides far from the valley of stability which beyond the reach of present-day facilities, mass predictions are important. Mass models are employed to make mass predictions when the nuclides of interest are beyond experimental reach.

Several mass models and semi-empirical mass formulas have been introduced. A general feature of these models is a tendency to agree with one another in the region of known masses. However, their predictions begin to diverge once you enter terra incognita [15]. In order to test the predictive power of these models, and to help to improve their accuracy, more mass measurements are required in these areas of interest.

High-precision mass measurements also play an important role in weak interaction studies, such as the mass measurement of ^{38}Ca, presented in this work. Nuclear beta decay provides us with a convenient laboratory for exploration fundamental interactions and symmetries. One example is the test of the Conserved Vector Current (CVC) hypothesis which asserts that the vector part of the weak interaction is independent of the nuclear interaction. This means that the β-decay strength, or ft value, should be constant in super-allowed $0^+ \rightarrow 0^+$ transitions. In order to measure the ft values of these decays, three experimental quantities are required: the half life of the species, the branching ratio, and the Q_{EC} of the $0^+ \rightarrow 0^+$ decay. Certain corrections to the ft value are also required as the decay takes place within the nucleus, yielding a modified ft, or $\mathcal{F}$t, value which, according to the CVC hypothesis, should be constant. To date there are 12 well-known CVC test candidates from which a mean $\mathcal{F}$t value [1] is calculated, verifying the CVC hypothesis to a level of 3×10^{-4}. Using the mean $\mathcal{F}$t value the vector coupling constant G_v can be calculated. G_v can be used to calculate the up-down quark matrix element, V_{ud}, of the Cabibbo-Kobayashi-Maskawa (CKM) matrix. Together with the other two elements, V_{us} and V_{ub}, the unitarity of the CKM matrix (required by the Standard Model) can be tested. In the interest of increasing the precision of G_v, more CVC candidates are desirable. ^{38}Ca, whose mass was measured to sufficient precision in this work, is such a potential candidate.

1.2 Mass measurement techniques for rare isotopes

Today there are two different techniques for mass measurements of radioactive species. The indirect technique involves reaction and decay measurements, whereas the direct technique usually involves a time-of-flight measurement, cyclotron frequency determination, or both. The indirect technique is called as such because it yields mass

differences, although direct mass measurements are not absolute and must be calibrated with some reference mass. This naming scheme is a long-standing convention and will be preserved here.

1.2.1 Production methods

There are several production methods for rare isotopes. They all possess specific advantages and complement one another. The isotope separation online (ISOL) technique uses a high-energy primary beam of light ions to bombard a thick target of heavier elements to produce rare isotopes via spallation, fission, and fragmentation. The targets are maintained at high temperatures so that the reaction products can be diffused out and into an ion source, where they are ionized. Afterwards they are accelerated to an energy of a few tens of keV, a beam energy well suited for Penning trap mass spectrometry. Very intense beams with excellent beam properties for certain elements are available, but chemical selectivity and decay losses in the target ultimately limit the range of secondary beams available [16].

Rare isotopes can also be produced by fusion or fusion-evaporation by bombarding a thin target with a low-to-medium energy primary beam, typically with energies of a few MeV/u. The heaviest elements are produced by fusion reactions. SHIP [17] at GSI utilizes a thin target of heavy metal, Pb or Bi, to produce heavy elements by fusion of the target and projectile. A primary beam, delivered by the UNILAC facility, is impinged on the target where fusion products exit from the other side at a few 100 keV/u. The ATLAS facility at Argonne National Lab produces rare isotope beams by fusion evaporation and in-flight separation. The ion guide isotope separation online (IGISOL) method [18] at JYFL produces rare isotopes by using a primary beam to bombard a thin target located within a gas cell. The reaction products exit the target and are thermalized in the buffer gas and extracted with electric fields. The advantage over the ISOL method is that it is not chemically

selective and the extraction times are in the sub-ms range, minimizing decay losses.

A powerful method of rare isotope production is the fragmentation of fast, heavy-ion beams after impinging on a light, thin target, which are then mass separated in flight. This is the method employed at the NSCL. The benefits of this method are many fold. The process produces fragments lighter than the projectile with no dependence on chemistry. Also, as there are no delay times associated with diffusion out of a target, shorter-lived nuclei are available from the fragmentation technique than from the ISOL technique. This method is very sensitive and can be used for the detection of rare isotopes with production rates on the order of a few per day. The resulting fragmentation beam still possesses a majority of the energy of the original primary beam. High-energy, high-emittance beams are poorly suited for low-energy experiments, but good for Coulomb excitation and reaction studies.

1.2.2 Indirect mass measurements

Indirect mass measurements involve the determination of Q values of nuclear reactions or radioactive decays. Various types of reactions have been used to determine masses both near and far from stability. With respect to the latter, reaction Q-value measurements allow for the masses of unbound nuclei to be determined.

The Q-value of nuclear decays provide mass differences between parent and daughter nuclei. In order to arrive at a final mass value from a decay the unstable species must be linked to a known mass. For isotopes far from stability the final mass determination may involve long chains of decays which can lead to the accumulation of error in the final mass value.

1.2.3 Direct mass measurements

The first direct mass measurements of rare isotopes were performed with magnetic spectrographs and spectrometers [19, 20]. In 1996 the last facility with a rare-isotope

mass measurement program based on deflection-voltage measurements, Chalk River, was closed. Today, all direct mass measurements are made by employing some combination of time of flight, frequency determination, and magnetic rigidity. Several spectrographs and spectrometers exist around the world for making mass measurements of rare nuclides at various precisions. SPEG [21], at GANIL, uses time of flight and magnetic rigidity measurements to achieve a mass resolution of $\approx 10^{-4}$. The time of flight is on the order of 1 μs, and although the resolving power is relatively low, SPEG's high sensitivity have allowed it to perform measurements far from the valley of stability. TOFI [22] at LANL was designed to measure the masses of light, neutron-rich nuclei. The S800 spectrograph [23] at the NSCL also uses time of flight and magnetic rigidity for making mass measurements in a similar manner, and regime, as SPEG. First mass measurements with the S800 in the ^{66}Fe region have recently been performed [24].

For a given time resolution the overall mass resolution is limited by the total time of flight of the ions. In an effort to improve the mass resolving power two approaches have been made. The first is to use cyclotrons to prolong the time of flight. In the case of the CSS2 [25] cyclotron, at GANIL, projectile fragments are injected into the cyclotron and radiofrequency fields are applied to accelerate species with a certain mass-over-charge value. The arrival time of the ion at a detector inside of the cyclotron is measured as a function of the phase of the radiofrequency, allowing a mass determination to be made. A similar approach [26] was used with SARA at Grenoble. The second approach is to use a storage ring, such as the Experimental Storage Ring (ESR) at GSI. By operating in isochronous mode [27] the revolution times of ions are recorded as they travel around the ESR, using a thin-foil detection technique for the time-of-flight detection. Ions of different mass create different time-of-flight spectra which can be compared to reference mass spectra to determine a mass value. Mass resolving powers on the order of 10^5 can be achieved and the method

has been employed to measure the masses of many short-lived, neutron-rich nuclides [27].

Even greater mass resolving powers can be obtained through frequency determination. Using the ESR it is possible to use cold electrons to cool the rare isotopes as they travel around the ESR and employ the Schottky method to detect the revolution frequency of the ions [28]. This method increases the resolving power to $\approx 10^6$ and requires a few thousand ions, yet the lengthy cooling times limit the half lives to $T_{1/2} > 5$ s.

The RF spectrometer MISTRAL, at ISOLDE, accepts the 60 keV ISOLDE beam, imposing a two-turn helicoidal trajectory through a homogenous magnetic field. Using MISTRAL one determines the cyclotron frequency, $\nu_c = qB/(2\pi m)$, of the nuclide of interest by the application of a radiofrequency signal applied to electrodes located at the one-half and three-half turn position within the magnetic field. If the phase difference in the applied RF signals is correct then ions experience an equal but opposite deflection when passing through the second electrode structure. An incorrect phase difference will result in a net deflection and the ions will not pass through an exit slit, which allows resolving powers of greater than 10^5 to be reached.

Today, Penning trap mass spectrometry is the most precise method available for measuring stable and unstable nuclides. Relative mass precisions of $\delta m/m < 10^{-10}$ [4] for stable species and $\delta m/m < 10^{-8}$ [29] for unstable species have been observed. Penning trap mass spectrometry of unstable nuclides with half lives down to 10 ms are considered to be possible, and the shortest-lived isotope studied so far is ^{74}Rb [30] which has a half life of $T_{1/2} = 65$ ms.

Penning trap mass spectrometers have been installed at radioactive beam facilities around the world. The first Penning trap mass spectrometer for rare isotopes, ISOLTRAP [31], was installed at the ISOLDE facility at CERN. The low-energy, low-emittance ISOL beams are ideal for precision experiments, such as Penning trap

mass spectrometry. Following ISOLTRAP's success, several Penning trap spectrometers were installed at other facilities: JYFLTRAP [32] at Jyväskylä, CPT [33] at Argonne National Lab, and SHIPTRAP [34] at GSI. Although CPT and SHIPTRAP are installed at facilities which produce low-to-mid energy rare isotope beams, an additional step is required to thermalize the beam before it can be used for Penning trap mass spectrometry. Thermalization of the rare isotope beam is accomplished by stopping the beam in a gas cell and extracting it at low energies.

1.2.4 LEBIT - the first Penning trap mass measurements on rare isotopes produced by projectile fragmentation

LEBIT is the first facility designed to thermalize high-energy, rare-nuclide beams produced by relativistic in-flight separation for precision experiments. Utilizing gas stopping of the high-energy secondary beam, it has been shown that fragmentation beams can be made amenable to precision low-energy experiments, such as Penning trap mass spectrometry. This demonstration also opens the door to future ISOL-type experiments, such as laser spectroscopy, in-trap decay studies, and experiments with post acceleration of nuclei unavailable at lower-energy facilities. The first experiment on a thermalized secondary beam was the Penning trap mass measurement of ^{38}Ca, discussed in this work, and of ^{37}Ca [11]. In order to take full advantage of the short-lived isotopes produced by produced by projectile fragmentation, new techniques must be developed to reduce the measurement time necessary to achieve a given relative mass uncertainty. In this work two such techniques are introduced. A new device, called a Lorentz steerer, is used for a fast preparation of the ion motion necessary for a cyclotron frequency determination. A new RF excitation scheme at twice the ion's cyclotron frequency, leading to an increase in resolving power, is studied in detail.

1.3 Outline of the dissertation

Due to the scale of the LEBIT project, many people were involved in bringing LEBIT from conception all the way to the first successful radioactive mass measurement of ^{38}Ca. In this document I will first provide an overview of the NSCL and LEBIT followed by more in depth discussion of the aspects that I was primarily responsible for. These topics include the design, construction and commissioning of the 9.4 T Penning trap system, stable Kr isotope measurements and the exploration of a new excitation scheme. Finally, I will present the results of the ^{38}Ca mass measurement, introducing ^{38}Ca as a test candidate of the CVC hypothesis.

CHAPTER 2

LEBIT Overview

2.1 The Coupled Cyclotron Facility

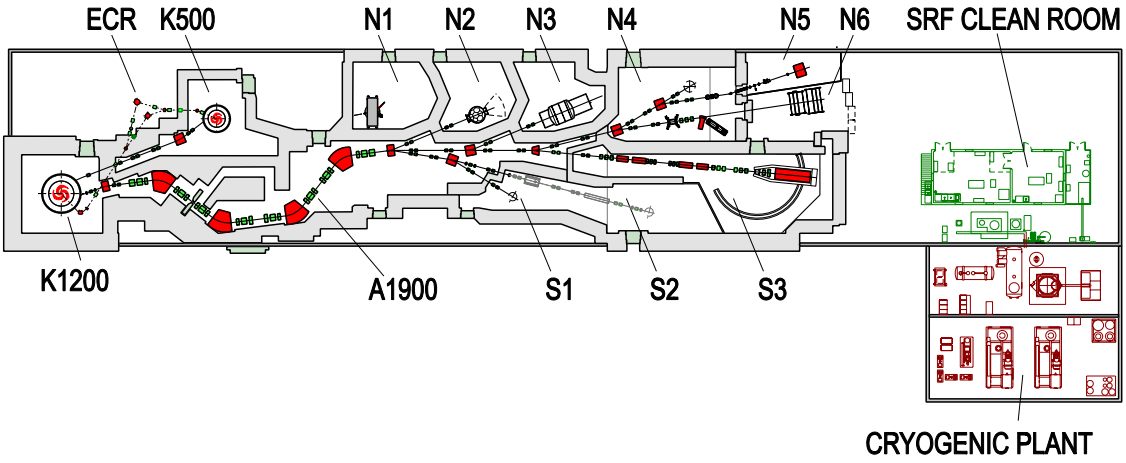

Figure 2.1. Layout of the Coupled Cyclotron Facility (CCF) at the NSCL.

The Coupled Cyclotron Facility (CCF) at the NSCL on the campus of Michigan State University is the premier rare isotope beam facility in the US. Fig. 2.1 presents an overview of the CCF. One of two Electron Cyclotron Resonance (ECR) ion sources is used to produce a primary ion beam of highly charged stable isotopes which is injected into the smaller K500 cyclotron. The K500 accelerates the beam to about 14

MeV/u. The extracted beam is injected into the larger K1200 cyclotron, where their remaining electrons are removed by a stripper foil. The K1200 then accelerates the beam to energies on the order of 140 MeV/u. The fast primary beam is extracted from the K1200 and focused on the production target, to produce rare isotopes by fragmentation reactions. The secondary beam is then injected into the A1900 fragment separator [35], where the beam is purified and a small range of fragments is selected by a two-stage separation. This secondary beam of rare isotopes can be delivered to the different experimental vaults (N2-N6, S1-S3). LEBIT is located in the N4 and N5 vaults. The gas stopping station is located in the shielded N4 vault as due to the high-energy beam. The rest of the LEBIT facility is located in the N5 vault as the beam has been thermalized, with an energy of only a few keV.

The layout of the LEBIT facility is shown in Fig. 2.2. There are four main components that are connected via an electrostatic beam transport system [11]. Six beam observation boxes (BOBs) are located along the beam line and are equipped with various detector systems, such as Faraday cups, microchannel plate (MCP) detectors and silicon detectors. The first component is a gas stopping station consisting of a gas cell and mass filtering radiofrequency quadrupole (RFQ) ion guides [9]. Here the fast secondary beam of rare isotopes delivered by the A1900 is stopped and and a low energy beam is produced. After the wall in the N5 vault is another RFQ system [11] for cooling and bunching the DC beam delivered by the gas cell/ion guide system. There is also a plasma test beam ion source that provides stable beams for offline testing, system optimization, and for providing reference ions for magnetic field calibration. Finally, at the end of the LEBIT beam line is a 9.4 T Penning trap mass spectrometer designed to make high-precision mass measurements on short-lived radioactive species.

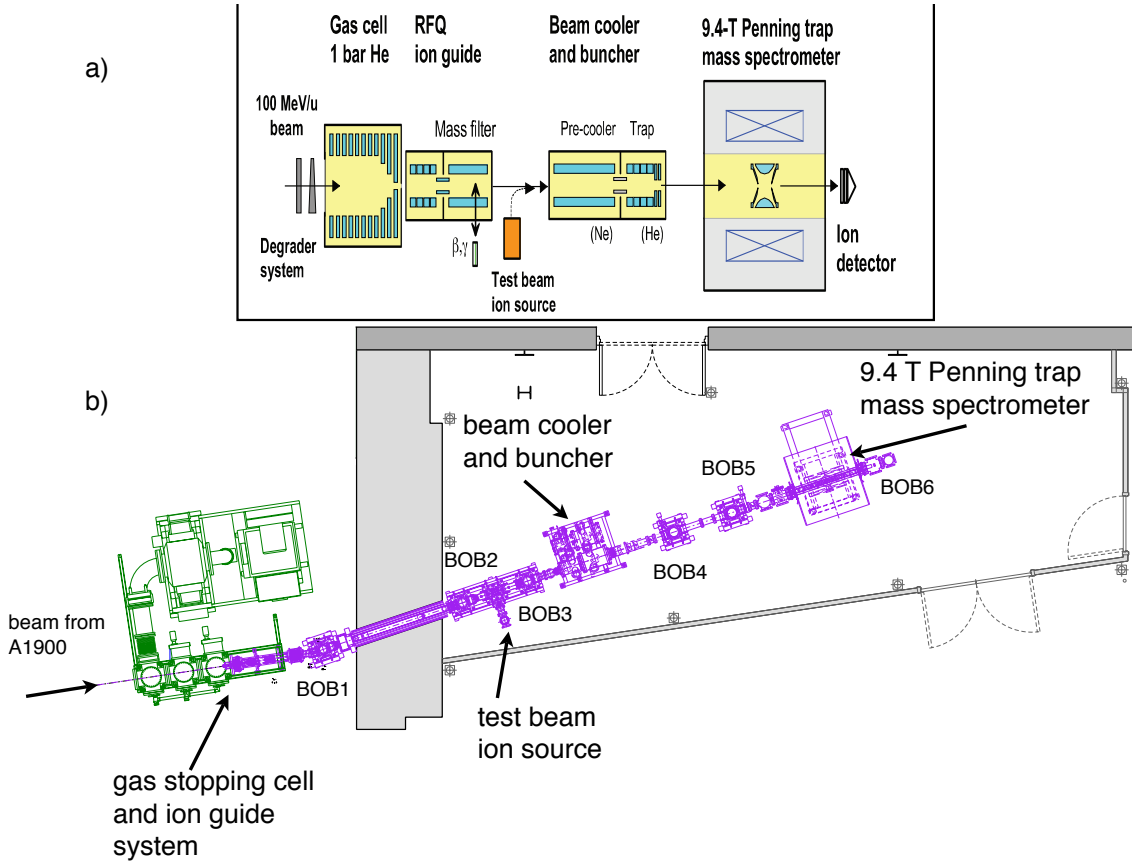

Figure 2.2. Layout of the LEBIT facility at the NSCL. BOB denotes beam observation boxes equipped with various detector systems. The two figures are (a) the schematic layout and (b) design drawing of the LEBIT system.

2.2 The gas stopping and ion guides station

Fig. 2.3 schematically shows the gas cell and ion guide system together with pictures of selected components. In order to stop the fast rare isotope beam from the A1900, it passes through a system of adjustable glass degraders where it loses most of its energy before passing through an aluminum wedge degrader which drastically reduces the momentum spread of the fragment beam. It then passes through a thin beryllium window into a 51 cm-long gas cell [36] filled with 1 bar of ultra-pure helium gas, where the ions ultimately come to rest. Helium is used because it has the highest

first ionization energy of any ion. As highly charged ions are delivered to the gas cell by the A1900 the ions are stopped by collisions with the gas. By charge exchange reactions with the helium gas they lower their charge state until they are, at least, in the Q = +1 state. Inside of the gas cell a system of ring electrodes (Fig. 2.3(b)) is used to create a DC gradient which pulls the ions through the gas towards an extraction nozzle. A series of electrodes (2.3(c)) near the nozzle focus them into a region where gas flow provides the dominant force and sweeps the ions through the nozzle, out of the gas cell, and into an RFQ ion guide system. This ion guide system is contained in three vacuum chambers and divided into sections by a small RFQ (μRFQ) (2.3(d)), which facilitates differential pumping and better beam transmission between the first and second chambers, and a diaphragm. The pressure in the first ion guide can reach as high as 0.2 mbar, while the pressure in the final chamber is on the order of 10^{-6} mbar. The mass-selective ion guides span the last two chambers. They allow filtering by mass-to-charge ratio, A/Q, and have been designed to achieve a resolving power of ≈ 50 with no loss in efficiency. A biased needle electrode can be inserted into the beam for collection and retracted to measure the collected activity on a nearby β detector. This method is used to measure the rate at which rare isotopes are extracted from the gas cell. When used in conjunction with the mass filter, the A/Q values of the radioactive atomic or molecular ions extracted out of the gas cell can be determined.

2.3 The test beam ion source

Beams from the test beam ion source are used extensively in system tuning and optimization, and also to provide reference masses during mass measurements of rare nuclides. Fig. 2.4 shows a photograph of the plasma ion source presently used. Gas is introduced through a needle valve into a gas inlet tube. Noble gases like Ar, Kr and Ne are typically used. To ionize these gasses, a tungsten filament is heated so that it

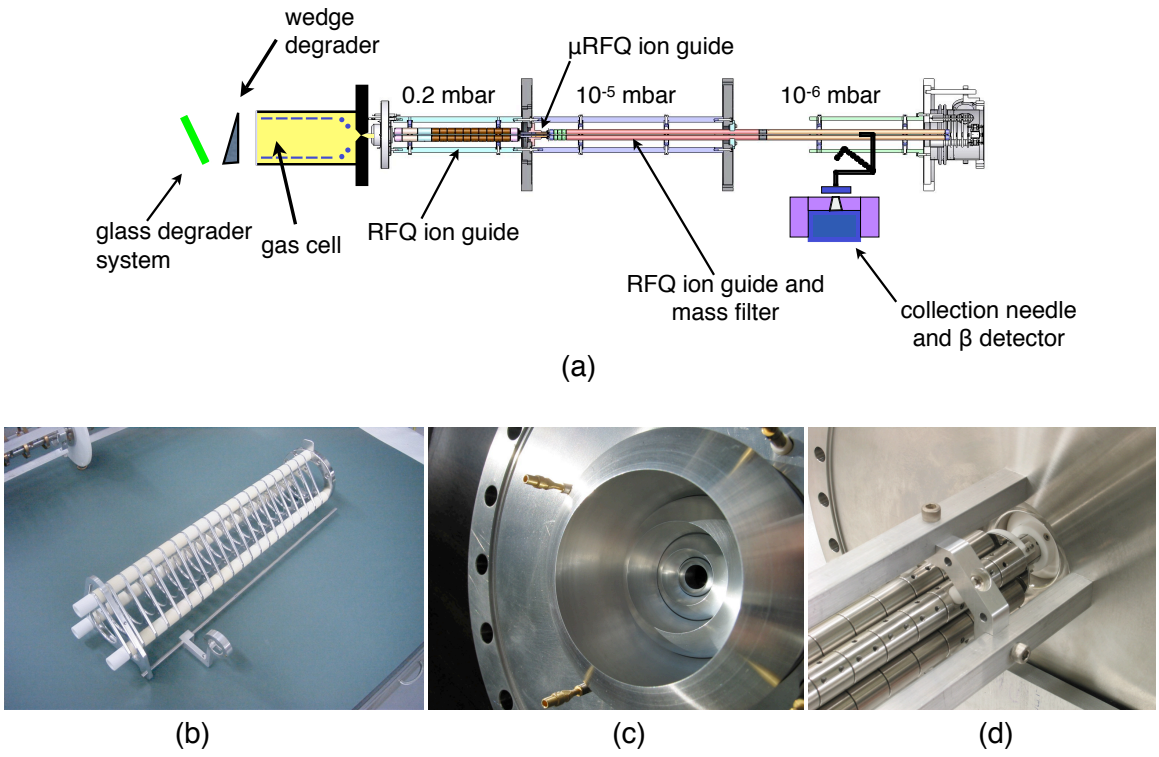

Figure 2.3. The gas stopping station. (a) schematic diagram of the gas cell and ion guides system. (b) gas cell ring structure for creating a DC gradient inside of the gas cell. (c) gas cell "flower" electrode for creating focusing potential. (d) partial section of the RFQ ion guides connected to the μRFQ.

produces electrons and is biased at around 100 V to produce a discharge. By changing the polarity of this bias alkali metals can also be produced via surface ionization present as impurities in the filament of the ion source. The test ion source is located perpendicular to the main LEBIT beam line. An electrostatic quadrupole deflector is employed to send the beam downstream to the cooler/buncher and Penning trap or upstream towards the gas cell.

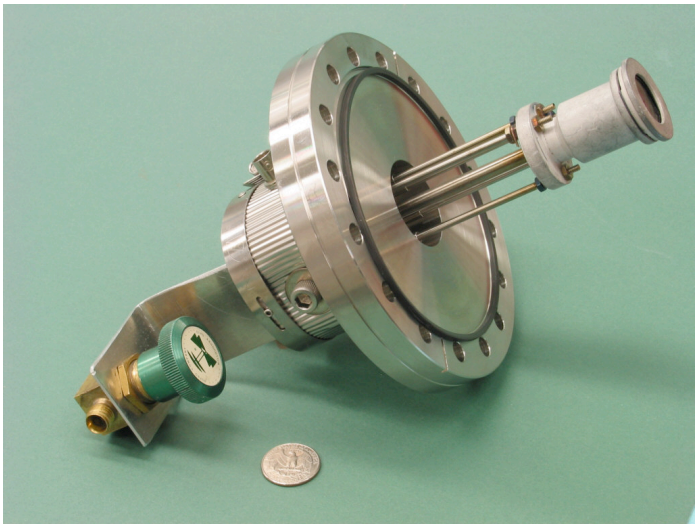

Figure 2.4. The test beam ion source.

2.4 The ion cooler/buncher system

The LEBIT ion accumulator and buncher accepts the 5 keV·Q continuous ion beam from the gas cell and converts it into a low-energy, low-emittance ion pulses. This device is a linear RFQ ion trap filled with a buffer gas at low pressure for ion cooling [11, 37, 38]. It features two separate vacuum sections (2.5(a)), one for beam pre-cooling and one for final cooling, trapping and beam bunching. The first section (2.5(b)) is typically operated with helium or neon at a pressure of $\approx 10^{-2}$ mbar. Neon can be used to increase the efficiency of Collision Induced Dissociation (CID) for the break up of molecular ions delivered from the gas cell. Before entering the system, the ions are electrostatically decelerated to a few tens of eV. Here the ions are transversely cooled and slowed down before they pass through a miniature RFQ ion guide (an efficient differential pumping barrier) into the trap section. The linear trap (2.5(c)) is operated with helium at a pressure 1-2 orders of magnitude lower than that in the first section to minimize beam heating during the pulsed-beam extraction. The ions are typically stored for 20-30 ms for their final cooling before they are extracted as a sub-μs ion pulse.

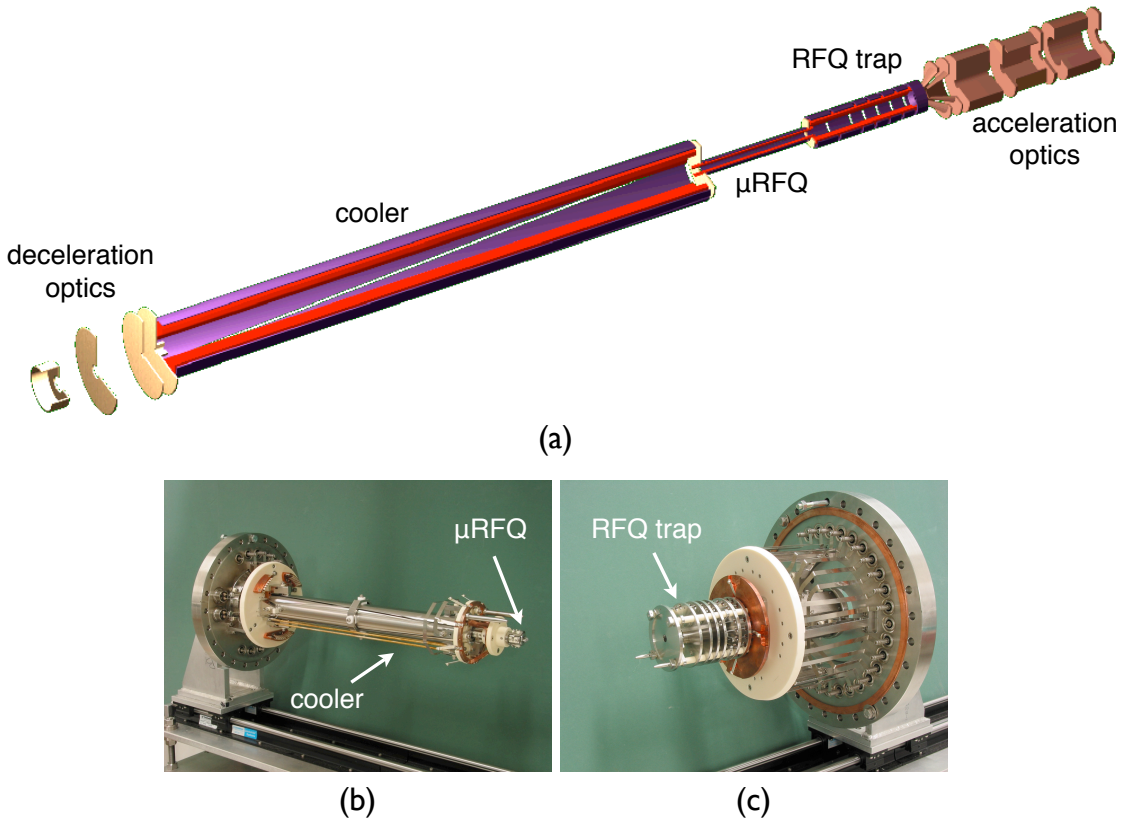

Figure 2.5. The LEBIT beam cooler and buncher. (a) design drawing of the LEBIT cooler and buncher. (b) Photograph of the ion guide cooler section together with the μRFQ. (c) Photograph of the RFQ ion trap for accumulation and bunching.

Both the pre-cooler and the trap sections have been built as cryogenic devices and can be cooled with LN_2 provided from a stationary cryogenic line, reducing the kinetic energy of the buffer gas. This increases the efficiency of the system by reducing the diameter of the beam in the cooler, making the transport between the two sections via the miniature RFQ more efficient. The low buffer gas temperature also decreases the cooling time and has the potential to reduce the emittance of the resulting pulse which would increase the efficiency of injection into the Penning trap. Cooling the system also results in the significant reduction of residual pressures of gases other than the noble gases used for beam cooling.

In contrast to standard RFQ ion coolers [39] used elsewhere the LEBIT system uses a wedged-electrode design which allows the electric drag potential in the cooling section to be created without the need for segmented rods. The LEBIT beam cooler and buncher has been extensively tested and its properties were found to be in very good agreement with beam simulations [40] involving realistic ion-atom interactions. In pulsed-mode operation the overall efficiency was found to exceed 50%, while in continuous mode operation values of up to 80% were observed.

In its normal mode of operation, continuous or pulsed ion beams from the gas cell or the test ion source are cooled and accumulated in the cooler/buncher and released as short ion bunches for capture in the precision trap of the LEBIT Penning trap mass spectrometer. For diagnostic purposes and buncher optimization time-of-flight distributions are routinely measured with a MCP detector downstream of the buncher. More details of the design of the buncher system can be found in the Ph.D. thesis of Tao Sun [11].

2.5 The 9.4 T Penning trap mass spectrometer

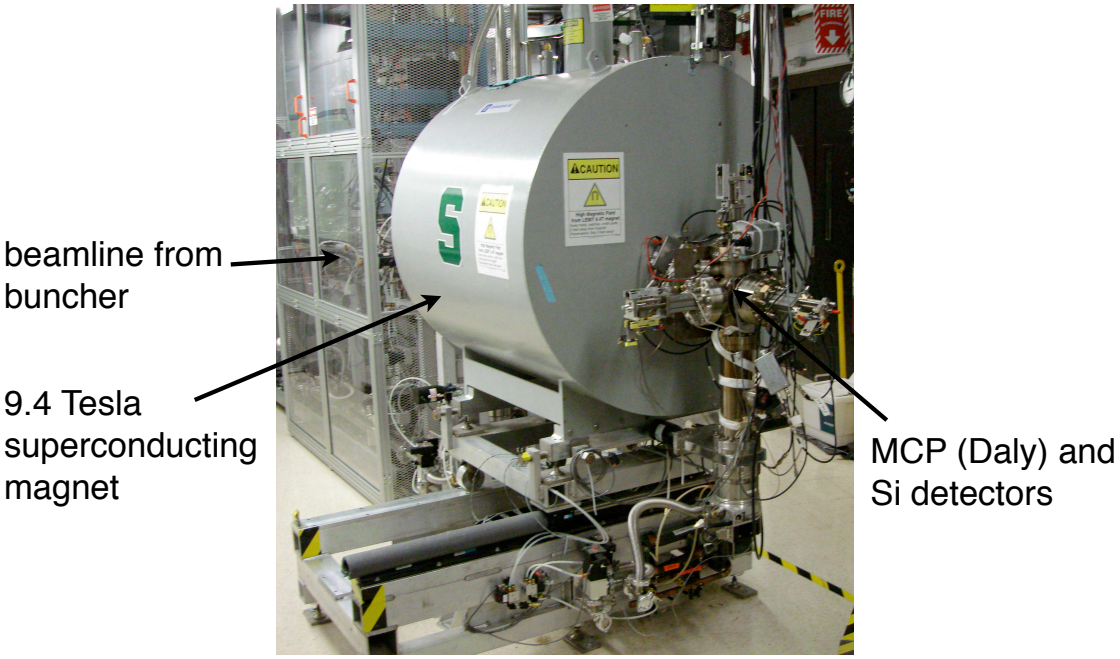

Figure 2.6. Photograph of the LEBIT Penning trap mass spectrometer.

The LEBIT Penning trap mass spectrometer, shown in Fig. 2.6, features a 9.4 T superconducting magnet. Housed within the bore of the magnet is the Penning trap system which was designed to make high-precision mass measurements of rare isotopes. Ion bunches are delivered from the buncher and trapped in the Penning trap. While trapped, the ion's motion can be driven with applied RF fields. The ion's response to the driving RF fields can be measured and used to determine its mass via a cyclotron resonance time-of-flight detection technique. Detailed information of the LEBIT Penning trap mass spectrometer will be presented in Chapter 3.

2.6 Overview of the performance of the LEBIT system

The efficiency of extracting rare nuclides which were stopped in the gas cell was measured to be about 5% for an implantation rate of ≈ 40 pps for a mixed ^{38}Ca/^{37}K beam [36]. The total efficiency of the transport of rare isotopes from the gas cell to final detector in BOB6 is estimated to be about 15 %.

After careful tuning of the potentials of the Penning trap and optimization of parameters for beam transport, ion capture and ejection, excellent line shapes and high resolving powers have been obtained with the LEBIT Penning trap mass spectrometer. The highest resolving power observed thus far is about 3 million for an excitation time $T_{rf} = 1$ s of $^{40}Ar^{+}$ ions.

In order to study the achievable precision and accuracy a large number of test measurements have been performed with stable ions, in particular $^{23}Na^{+}$, $^{39}K^{+}$, $^{40}Ar^{+}$, $^{40}Ar^{2+}$, and $^{A}Kr^{+}$. From these tests we conclude that LEBIT has the potential to achieve a very high accuracy. For example, the measured frequency ratio of stable $^{40}Ar^{2+}$ and $^{23}Na^{+}$, both known with sub-ppb precision, is in full agreement with the expected ratio obtained from literature mass values [2], showing an insignificant deviation of only $3(5) \times 10^{-9}$. This example corresponds to a close-doublet situation. The results obtained for a $^{A}Kr^{+}$ -$^{39}K^{+}$ mass comparison, discussed in Chapter 6, shows excellent agreement even for large mass differences, indicating that mass-dependent systematic uncertainties are small.

In the period from May of 2005 through November of 2006 LEBIT has made high-precision mass measurements of 26 rare nuclides: ^{37,38}Ca, ^{64,65,66}Ge, ^{40,41,42,43,44}S, ^{66,67,68,80}As, ^{29,34}P, ^{63,64}Ga, ^{68,69,70,81m,81g}Se, ^{33}Si, ^{70m,71}Br. The mass measurement of the super-allowed $0^{+} \rightarrow 0^{+}$ emitter ^{38}Ca, presented in this work, with a relative mass precision δm/m = 8×10^{-9} illustrates the precision to which the mass of

rare nuclides can be measured with the LEBIT system. LEBIT's sensitivity is demonstrated by the mass measurement of ^{37}Ca [37] where cyclotron resonance curves were obtained with a total of $\approx$ 50 detected ions. The mass measurement of ^{66}As, with $T_{1/2} = 96$ ms, indicates the short time scales necessary for the performance of high-precision mass measurements.

CHAPTER 3

The LEBIT High-Precision Penning Trap

Over the years a large amount of effort has been expended to optimize both the precision and accuracy of Penning trap systems [3, 41, 42]. Today they are the most precise instruments for making mass measurements on both stable and unstable species. In this chapter I will explore some basic Penning trap concepts dealing with ideal traps and RF excitations, and then move on to properties of realistic traps and discuss the design of the LEBIT Penning trap system.

3.1 Basic Penning trap concepts

Three-dimensional ion confinement in a Penning trap is achieved by superimposing an axial, electric quadrupole field in a homogenous, axial magnetic field, as illustrated in Fig. 3.1. The electric quadrupole field is generated by two hyperbolic endcap electrodes and one hyperbolic ring electrode. Hyperbolic electrodes are used to minimize higher-order electric field contributions. Other configurations also exist [43], but are not relevant to this discussion.

This electric field confines the ions in the axial direction. By placing this electrode

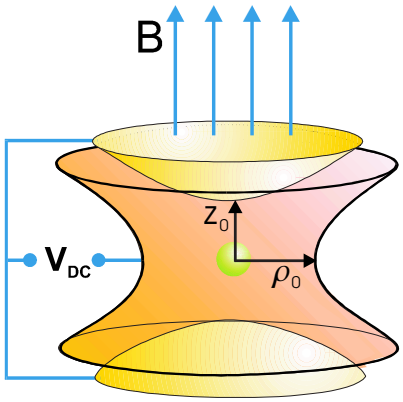

Figure 3.1. Cartoon illustrating the basic Penning trap concept. An axial electric quadrupole field is generated by a hyperbolic electrode configuration and embedded in a homogenous magnetic field oriented in the axial direction.

system in an axial magnetic field full three-dimensional confinement is achieved. The electric quadrupole potential created by the electrode configuration can be described in cylindrical coordinates (r,θ,ϕ) by

$$\phi_2 = \frac{a_2}{2}(2z^2 - r^2) \tag{3.1}$$

This potential can be realized by two hyperboloids of revolution given by

$$z^2 - \frac{r^2}{2} = \pm z_o^2 \tag{3.2}$$

where z_o is half the distance between the two endcap electrodes, as seen in Fig. 3.1. If we specify the quantity U_o as the potential difference between the endcap and ring electrodes, then the coefficient of the quadrupole expansion can be written as

$$a_2 = \frac{U_o}{2d^2} \tag{3.3}$$

where d is a characteristic trap parameter given by $d = \sqrt{\rho_o^2/4 + z_o^2/2}$. This yields the trapping potential

$$\phi_2 = \frac{U_o}{4d^2}(2z^2 - r^2) \tag{3.4}$$

and leads to the quadrupole trapping field

$$\begin{aligned} E_r &= \frac{U_o r}{2d^2} \\ E_z &= -\frac{U_o z}{d^2} \end{aligned} \tag{3.5}$$

3.1.1 Ion motion in a Penning trap

Charged particles in a magnetic field execute a circular cyclotron motion around the field lines with frequency

$$\omega_c = \frac{q}{m}B, \tag{3.6}$$

where q is the charge of the particle, B is the strength of the magnetic field and m is mass of the particle. Superimposing an azimuthal, electric quadrupole field within a uniform magnetic field and using them to trap a charged particle causes the particle to execute three independent eigenmotions. The electric quadrupole field is responsible for an axial oscillation with a frequency ω_z. The remaining two eigenmotions are in the radial plane: a slow magnetron motion with frequency ω_- due to the $\mathbf{E}\times\mathbf{B}$ drift motion of the particle, and a cyclotron motion with a modified frequency ω_+. Fig. 3.2 illustrates the three eigenmotions. In a pure electric quadrupole field the frequencies of the two radial eigenmotions are given by

$$\omega_\pm = \frac{\omega_c}{2} \pm \sqrt{\frac{\omega_c^2}{4} - \frac{\omega_z^2}{2}}, \tag{3.7}$$

where the axial oscillation frequency is given by

$$\omega_z = \sqrt{\frac{qU_o}{md^2}}. \tag{3.8}$$

In the general case of a strong magnetic field and a comparatively weak electric field $\omega_+ \gg \omega_z \gg \omega_-$. Two other important relationships between the three eigenmotions are

$$\omega_+ + \omega_- = \omega_c \tag{3.9}$$

and

$$\omega_+ \omega_- = \frac{\omega_z^2}{2} \tag{3.10}$$

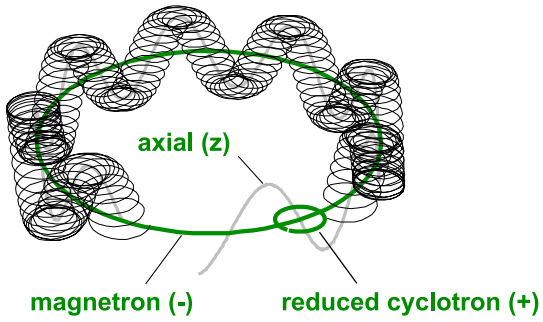

Figure 3.2. Cartoon illustrating the three independent eigenmotions executed by an ion in a Penning trap. The two radial eigenmotions are the cyclotron and magnetron motion, while the third motion is the axial oscillation.

The mass of an ion can be determined from Eq. 3.6, if we know the charge state of the trapped ion and the strength of the magnetic field. This can be determined by a calibration measurement of a well-known stable species.

3.1.2 Ion capture in a Penning trap

There are two methods used to capture ions in a Penning trap: a dynamic and a static method. In the static method the Penning trap electrodes are used to create a static potential well within a buffer gas. Ions are injected into the Penning trap, losing enough energy via collisions with the buffer gas such that they cannot escape

the trapping potential. The static method is not compatible with high-precision mass measurements due to subsequent interaction of the ion of interest with the buffer gas during the measurement. The dynamic method involves fast switching of voltages applied to the Penning trap electrodes. An ion is ejected from the cooler/buncher and drifts into the Penning trap system. When the trap is open the injection endcap voltage is low while the ejection endcap voltage is kept high. When the ions have drifted into the trap the voltage on the entrance endcap is raised and the ions are trapped. The process is illustrated in Fig. 3.3. In a perfect capture the ion comes to rest at the trap center when the voltage on the entrance endcap is raised which results in an ion with no axial energy. This is achieved by adjusting the slope of the injection potential such that the ion comes to rest at the trap center and immediately switching to the trapping potential. When multiple ions are captured a perfect capture results in the mean axial position of the ion bunch remaining at the trap center with the individual ions oscillating about the axis with some amount of axial energy. To remove ions from the trap the voltage on the ejection endcap is lowered, allowing ions to drift out.

3.1.3 Excitation of ion motion

Once the ion is trapped its motion can be excited through the application of multipolar RF fields. For the mass measurement technique used in LEBIT, RF excitation with multipolar, azimuthal RF fields is important. The most common method of introducing such a field is by segmenting the ring electrode and applying RF voltages to the ring segments for different multipolarities. An RF dipole field can be created by applying two RF signals with the same amplitude which are 180° out of phase to two diametrically opposite ring segments. The RF dipole field can drive one eigenmotion. By applying an azimuthal RF dipole field at frequency ν_+ or ν_- it is possible to drive either the cyclotron or magnetron motion of a trapped ion, increasing the amplitude,

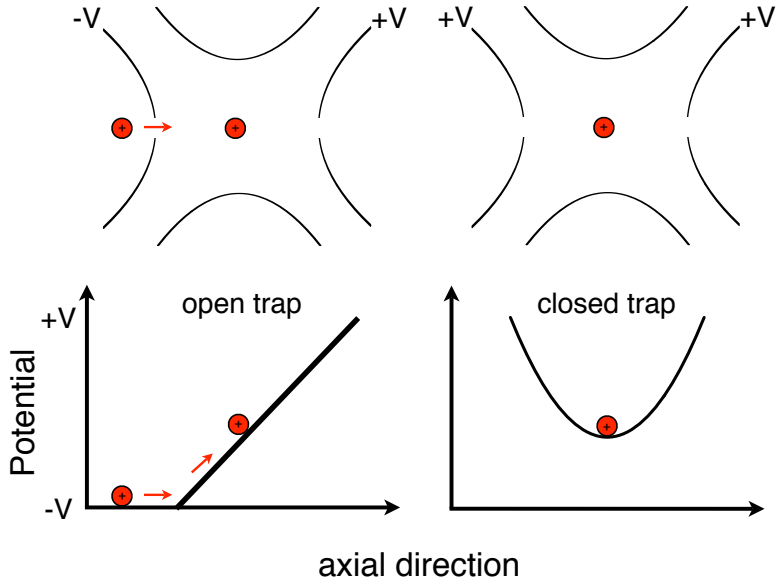

Figure 3.3. Cartoon illustrating the process of capturing an ion in a Penning trap. Shown is the potential along the axis of trap between the endcaps.

ρ_+ or ρ_-, of the eigenmotion. An azimuthal RF quadrupole field couples both radial eigenmotions. An azimuthal RF quadrupole field is created by applying two RF signals with the same amplitude which are 180° out of phase to a pair of diametrically opposite ring segments. With LEBIT the most important frequency driven with an azimuthal quadrupole field is $\nu_+ + \nu_- = \nu_c$. The application of a quadrupole RF field at frequency ν_c causes a periodic beating between the magnetron and cyclotron motions of an ion in a Penning trap, illustrated in Fig. 3.4, and is used to pump energy into the system which is detected and used to make a mass determination. The ion must initially be executing some radial motion to make this conversion. Traditionally this is achieved by first applying an azimuthal RF dipole field to drive the ion off axis. The figure on the left represents an ion beginning in a state of pure magnetron motion, $\rho_o = \rho_-$, as illustrated by the circle. When the quadrupole RF field is turned on, the cyclotron amplitude begins to grow and the magnetron amplitude begins to shrink. The figure on the right skips forward in time until the magnetron amplitude

has decreased to $\rho_- = 0$ and $\rho_+ = \rho_o$. Since $\nu_+ \gg \nu_-$ the conversion of ρ_- to ρ_+ is accompanied by a drastic increase in radial energy of the stored ion. A π-pulse at frequency $\nu_{rf} = \nu_c$ is defined as the product of the length of time for which the RF excitation is applied, T_{rf}, and RF amplitude, U_{rf}, such that the initial magnetron motion is completely converted into cyclotron motion.

In addition to the excitation of ion motion via the application of azimuthal dipole and quadrupole RF fields an octupole RF field can be used drive the radial eigenmotions at a frequency $\nu_{rf} = 2\nu_+ + 2\nu_- = 2\nu_c$. This excitation requires eight ring segments and offers an increase in resolving power over the standard quadrupolar excitation. The octupolar excitation will be discussed in detail in Chapter 4

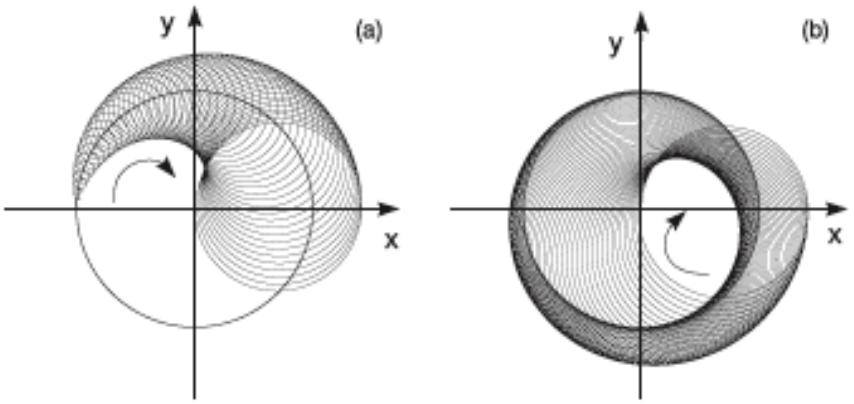

Figure 3.4. (a) Ion begins in a state of pure magnetron motion, until quadrupolar RF field is turned on and the reduced cyclotron radius begins to grow. (b) full conversion of magnetron to reduced cyclotron motion.

3.1.4 Time-of-flight cyclotron resonance detection scheme

After the application of a quadrupolar excitation at frequency ν_{rf}, the trapped ion may have gained some amount of radial energy if $\nu_{rf} \approx \nu_c$. In LEBIT, and in other Penning trap experiments, this energy is detected with a time-of-flight resonance detection technique [3, 44, 45]. In order to detect a change in the radial energy of an

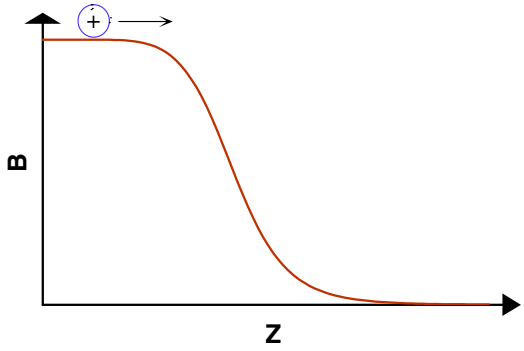

$$F = -\mu \frac{\partial B}{\partial z} = -\frac{E_r}{B_o} \cdot \frac{\partial B}{\partial z}$$

Figure 3.5. Cartoon illustrating the time-of-flight detection principle. The ion experiences a force in the axial direction due to the magnetic field gradient and gains axial energy. E_r is the radial energy of the ion and B_o is the initial magnetic field strength.

ion the voltage on the ejection endcap is lowered, as described in Sec. 3.1.2, and the ion drifts along the magnetic field to a detector where the time of flight is measured. As the ion travels through the ejection optics the strength of the magnetic field begins fall off. Since the ion is executing cyclotron motion it has a magnetic moment, and the ion experiences a force in the axial direction due to the gradient in the magnetic field. This process is illustrated in Fig. 3.5. Here E_r is the radial energy of the ion and B_o is the initial magnetic field strength. When the ion has left the magnetic field all of the energy gained during the excitation has been converted into axial energy and a reduced time of flight is measured at the end of the system with an MCP detector.

The total time of flight of the ion can be calculated by

$$T(\omega_{rf}) = \int_{z_o}^{z_1} \left(\frac{m}{2[E_o - q \cdot V(z) - \mu(\omega_{rf}) \cdot B(z)]} \right)^{\frac{1}{2}} dz, \tag{3.11}$$

where E_o is the total initial energy of the ion, q is the charge of the ion, $V(z)$ is the electric potential along the ion's path, and $B(z)$ is the magnetic field strength along the ion's path. A theoretical description of the ion motion during a quadrupolar

excitation [3] can be used in conjunction with Eq. 3.11 to determine the initial radial eigenmotion amplitudes, $\rho_{+,o}$ and $\rho_{-,o}$, if $V(z)$ and $B(z)$ are known. This has been used extensively in the study of the octupolar excitation (Chapter 4) and in characterizing the Lorentz steerer (Chapter 5).

3.1.5 Mass measurement procedure using the LEBIT Penning trap mass spectrometer

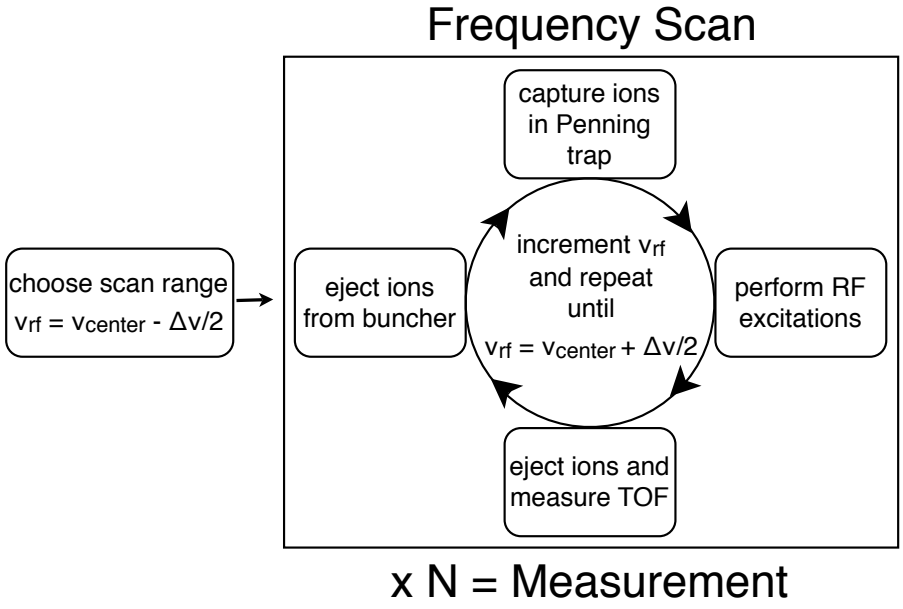

Figure 3.6. Chart illustrating the mass measurement cycle used with the LEBIT Penning trap mass spectrometer.

A cyclotron resonance curve measured with the time-of-flight technique outlined in the previous section is obtained in the following manner. First, a frequency scan range, $\Delta\nu$ is chosen depending on the mass uncertainty of the ion being measured. Next, an ion bunch is delivered from the buncher and trapped in the Penning trap. After purification of the ion bunch by the application of a mass-selective dipolar excitation, a quadrupolar excitation at frequency $\nu_{rf} = \nu_{center} - \Delta\nu/2$ is applied. The ions are ejected from the trap and their time of flight to the MCP is recorded. This process,

called a frequency scan, is repeated, incrementing ν_{rf} until $\nu_{rf} = \nu_{center} + \Delta\nu/2$. A measurement consists of one or more frequency scans and is outlined in Fig. 3.6. A sample cyclotron resonance curve for $^{82}Kr^{+}$ ions is shown in Fig. 3.7. For an excitation time of T_{rf} = 200 ms a line width of $\Delta\nu$ = 5 Hz is obtained for N $\approx$ 1000 detected ions, resulting in a resolving power of $R = \nu/\Delta\nu \approx$ 450,000. Perfect agreement is observed between the data points and the theoretical fit to the data [3].

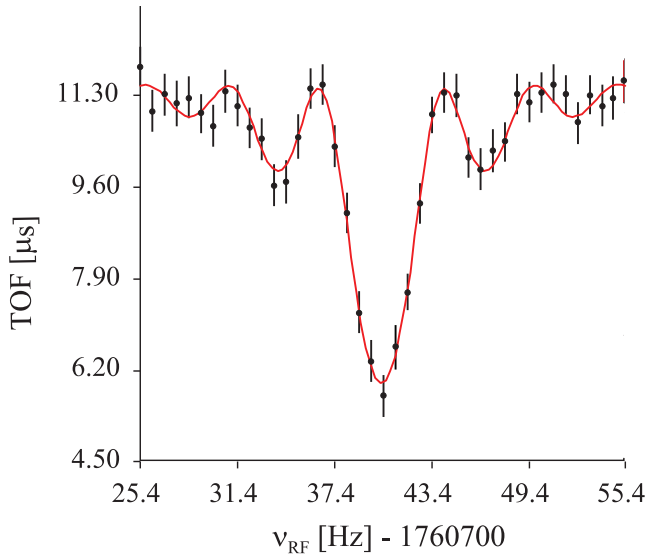

Figure 3.7. Cyclotron resonance curve of $^{82}Kr^{+}$ ions with an excitation time of T_{rf} = 200 ms with N $\approx$ 1000 detected ions. Solid line is a theoretical fit [3] to the data.

In order to make a Penning trap mass measurement the magnetic field must be known very precisely in order to determine the mass via a determination of the cyclotron frequency, $\nu_c = qB/(2\pi m)$. This is accomplished by making a measurement of a nuclide, usually stable, with a very well-known mass. The mass of the ion of interest can then be determined by $M = (\nu_{c,ref}/\nu_c)\cdot M_{ref}$ where M is the mass of the ion of interest, M_{ref} is the mass of the reference ion, ν_c is the cyclotron frequency of the ion of interest, and $\nu_{c,ref}$ is the cyclotron frequency of the reference ion. In order to determine the atomic mass of the ion of interest the electron mass and

electron binding energy are required. Isotopic shifts in the electron binding energies are negligible, and the electron binding energies of stable isotopes can be used.

With any real persistent superconducting magnet the field decays over time, and multiple reference measurements are required to determine the magnetic field as a function of time. In order to determine the strength of the magnetic field during a real mass measurement a reference measurement is taken before and after the measurement of the ion of interest. The cyclotron frequency of the reference ion is then linearly interpolated to the time at which the ion of interest was measured, as is illustrated in Fig. 3.8.

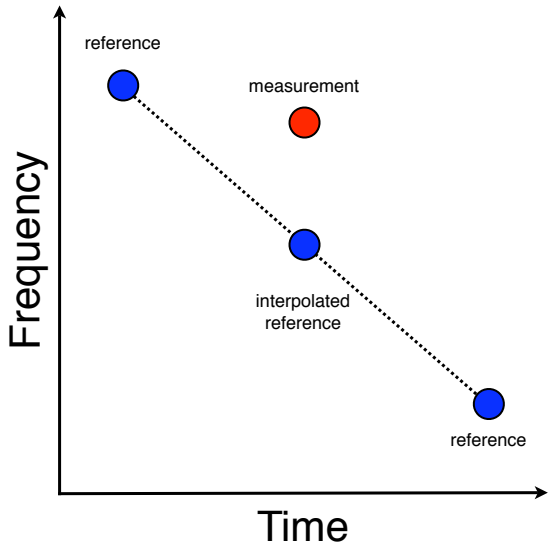

.

3.2 The LEBIT Penning trap mass spectrometer

Fig. 3.9 shows the schematic layout of the experimental setup of the LEBIT Penning trap mass spectrometer. The magnetic field is provided by an actively shielded, persistent, solenoidal, superconducting 9.4 Tesla magnet system built by Cryomagnetics, Inc. with a room-temperature, horizontal bore. The magnet system has been up-

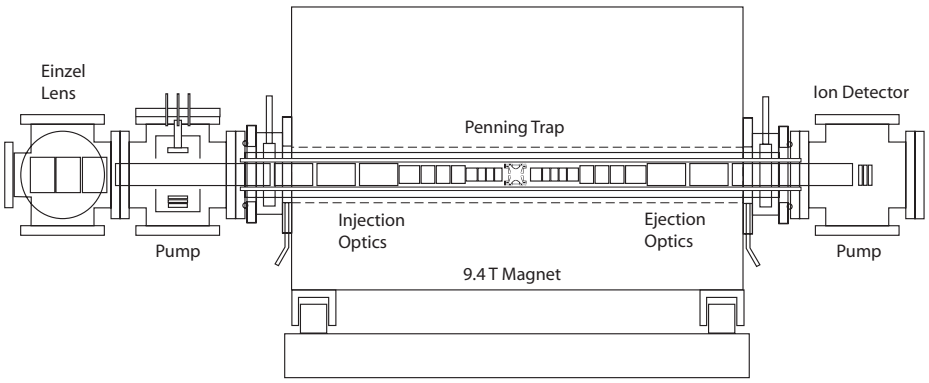

Figure 3.9. Schematic drawing of the LEBIT Penning trap mass spectrometer.

graded by the addition of external-field compensation coils [46] to reduce the effect of external field changes that may occur in an accelerator environment. The employment of a 9.4 T field, as compared to $\approx$ 6 T which is typical of current systems, has the advantage that a given precision can be achieved in about half the measurement time. The primary magnet specifications are listed in Table 3.2.

A precisely machined vacuum tube, mounted inside of the room-temperature bore of the magnet, serves as an ion optical bench for the trap electrode system. Since bore of the magnet may not be exactly parallel with the magnetic field axis the ends of the bore tube are secured to the magnet using translational mounts. To align the bore tube with the magnetic field an electron gun was used. The electron gun was placed in the center of the bore tube with two detection electrodes separated into quadrants on either side. The electron current on each quadrant can be read while the the position of the bore tube is adjusted with the translational mounts. When the currents on each quadrant are roughly identical the bore tube was declared to be aligned to the magnetic field axis.

The magnet rests on a translational mount which allows it to be moved so that the injection and ejection optics systems can be easily removed from the bore tube. On either side of the cryostat are two 300 L/s turbo pumps. After several months of pumping the pressure in the two chambers is on the order of 10^{-9} mbar. An MCP

Table 3.1. Specifications of the LEBIT 9.4 T magnet

Parameter	Value
central field homogeneity	± 10 ppm over a cylindrical volume 5.1 cm diameter × 10.2 cm length
persistent mode field decay	(dB/B)/dt ≈ -1×10^{-8}
bore diameter	12.8 cm
cryostat diameter	116.8 cm
cryostat length	101.6 cm
LHe capacity	325 L
LHe refill rate	≈ 3 months (250 L)
LN2 capacity	150 L
LN2 refill rate	≈ 2 weeks (140 L)

detector in a Daly [47] configuration is placed in BOB6.

Several improvements to the magnet system have also been added. The pressure of the helium bath is stabilized by an electric valve operated on a PID loop to eliminate non-linear magnetic field effects, on top of the natural magnetic field decay, due to variations in the helium boil-off rate. The Penning trap and nearby ion optical elements can be cryogenically cooled, reducing residual gas pressure which can cause frequency shifts while performing a measurement. A pair of insulated copper wires wound around the tube allow for either baking or compensation of the natural decay of the main magnetic field during measurements.

The Penning trap and associated injection and ejection optics have been optimized to avoid introducing large uncertainties in the measurements or losses in efficiencies. The electrode structure of the LEBIT Penning trap has been designed such that higher-order contributions to the electric trapping field have been minimized. The materials used to construct the trap have also been distributed such that the magnetic field in the center region of the trap remains homogenous. The injection optics have

been designed to minimize transverse energy pickup as the ions are injected into the magnetic field. The ejection optics must transport the ions out of the magnetic field and efficiently focus them onto the MCP detector at the end of the system. Details on the design of these systems will be covered in the following sections.

3.2.1 High-precision electrode system

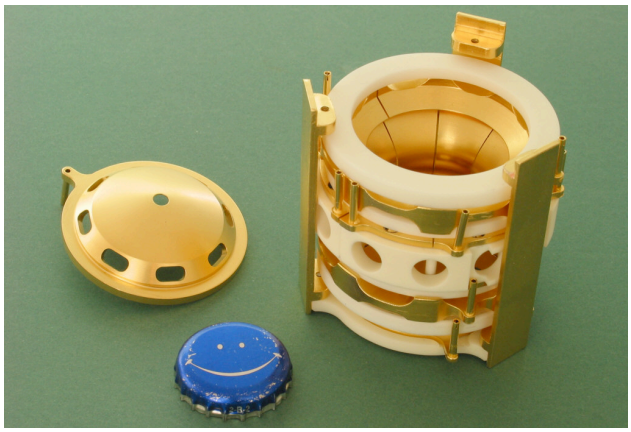

Figure 3.10. The LEBIT high-precision Penning trap with one endcap electrode removed. Note the hole in the endcap for ion injection/ejection.

The final design drawing of the LEBIT high-precision Penning trap is shown in Fig. 3.11. In addition to the ring and endcap electrodes there are two sets of correction electrodes. In order to generate a perfect electric quadrupole field the hyperbolic electrodes would need to extend to infinity. In a real Penning trap the electrodes are truncated, which introduces higher-order field contributions. These higher-order terms can be minimized by adding correction ring electrodes to compensate for the finite nature of the ring and endcap electrodes. The holes in the endcap electrodes also introduce higher-order field contributions and are partially compensated by the addition of correction tube electrodes.

The LEBIT Penning trap's electrodes are constructed of high-conductivity copper and plated with gold to reduce possible patch effects for the creation of a homoge-

nous electric field. The shape and dimensions of the electrodes have been optimized to achieve close-to-ideal electric and magnetic fields within the trap, and will be discussed in detail in the following sections. The insulators are made of Alumina. The ring electrode has an eight-fold segmentation. This allows not only for the creation of a quadrupole RF field, as required for the excitation of the ion motion at the ion's cyclotron frequency ν_c [42], but also the application of an octupole RF field, which makes ion motion excitation at $2\,\nu_c$ possible, which is discussed in Chapter 4. Fig. 3.10 shows a photograph of the LEBIT high-precision Penning trap with on endcap removed. The electrodes are gold and the Alumina insulators are white.

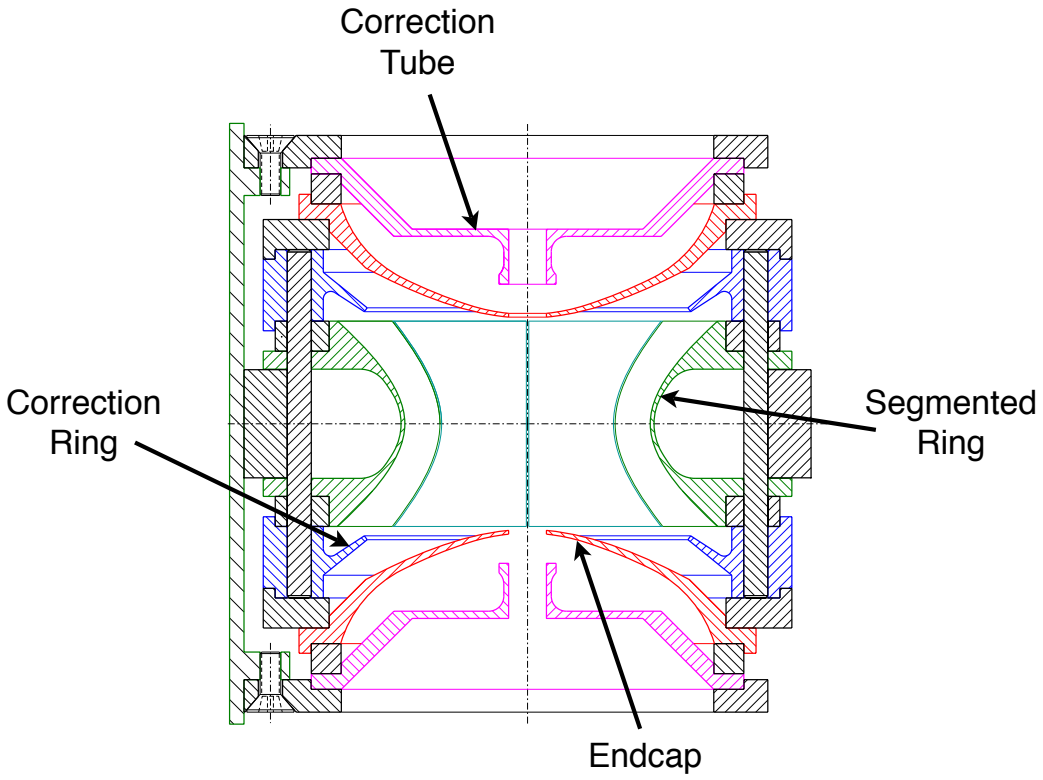

Figure 3.11. Design drawing of the LEBIT high-precision Penning trap. Color version: black-hashed elements are insulator and color-hashed elements are electrodes.

Minimizing the effects of electric field imperfections

As part of the design of the electrode system detailed simulations have been carried out. The trap geometry is symmetric azimuthally and about the z = 0 plane so the electric potential generated by the electrodes can be written as the expansion

$$\phi = \sum_l r^l P_l(\cos\theta), \tag{3.12}$$

where P_l are the normal Legendre polynomials and l = 2n for n = {0,1,2,...}. As in [42] we can write the coefficients of the higher order terms as

$$a_l = \frac{U_o}{2d^l} C_l, \tag{3.13}$$

where, again, U_o is the voltage applied to the endcap electrodes relative to the ring electrode potential. The dimensionless coefficients, C_l, then represent a degree of deviation from the pure quadrupole field where $C_2 = 1$ and all others are zero.

The potential along the z-axis can be written in cylindrical coordinates as the polynomial expansion

$$V(z) = \frac{V_o}{2}\left(C_o + \frac{C_2}{d^2}z^2 + \frac{C_4}{d^4}z^4 + \frac{C_6}{d^6}.z^6 + \cdots\right) \tag{3.14}$$

The ion-optics simulation package SIMION was used to analyze the trap configuration in an attempt to reduce the higher-order terms. SIMION uses the finite difference method to calculate potentials of systems of user-defined electrodes. Several configurations were investigated and the final geometry is shown in Fig. 3.12. The characteristic trap parameters which apply both to the physical trap and the SIMION geometry are given in Table 3.2.1.

The geometry is grouped into 4 pairs of electrode systems: the pair of endcap electrodes, the ring electrode, the pair of correction rings, and the pair of correction tubes. The potentials for each pair of electrode systems can be extracted from the SIMION data files and used to determine the optimal voltages which need to be

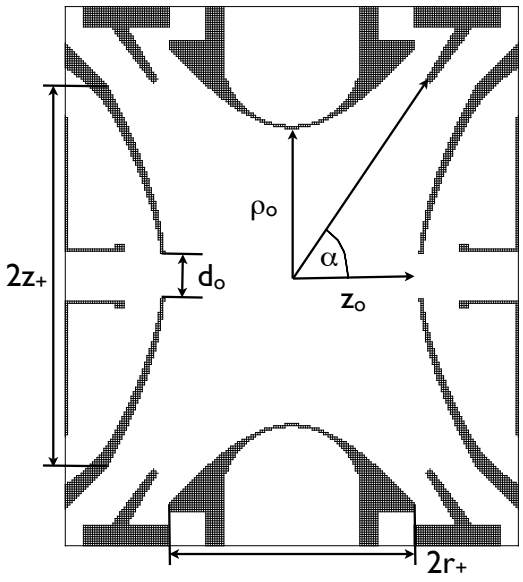

Figure 3.12. LEBIT Penning trap geometry used for electric potential calculations with SIMION. The geometry corresponds to the final design of the LEBIT Penning trap.

applied to the electrodes by a fitting routine described in Appendix D. Using the fit method described in Appendix D, I choose a conservative range of ±9 mm along the trap axis to fit the data. The physical extent of the ion cloud is expected to be considerably smaller. The optimum electrode voltages along with the resulting C_l values from Eq. 3.14 are presented in Table 3.3.

In order to use the C_l's to calculate expected frequency shifts due to higher-order electric field contributions it is easiest to use the method which is presented in [41]. First order perturbation theory can be used to evaluate the effects of the trap imperfections [42]. Applying the results found in [42], the frequency shifts due to the two lowest-order imperfection terms are

$$\Delta\omega_c = \frac{3}{4}\frac{C_4}{z_o^2}\frac{\omega_z^2}{(\omega_+ - \omega_-)}(\rho_+^2 - \rho_-^2),\ for\ C_4 \tag{3.15}$$

and

$$\Delta\omega_c = \frac{15}{8}\frac{C_6}{z_o^4}\frac{\omega_z^2}{(\omega_+ - \omega_-)}[3z^2(\rho_-^2 - \rho_+^2) + (\rho_+^4 - \rho_-^4)],\ for\ C_6 \tag{3.16}$$

Table 3.2. Parameters of LEBIT Penning trap.

Parameter	Value
ρ_o	13 mm
z_o	11.18 mm
α	54.74°
$2r_+$	21.6 mm
$2z_+$	33.6 mm
d_o	4 mm
d	10.23 mm

Table 3.3. Optimum electrode voltages (relative to the ring voltage) and the associated C_l's calculated using the LEBIT Penning trap SIMION geometry described above.

Parameter	Value
Endcaps	1.67235 V
Ring	0 V
Correction Rings	0.61227 V
Correction Tubes	2.87919 V
C_0	0.80590
C_2	1.00187
C_4	0.00207
C_6	-0.00442
C_8	0.00294

Table 3.4. Frequency shifts, $\Delta\nu_c$, associated with the octupole and dodecapole components of the electric field using the optimum electrode voltages.

l	$\Delta\nu_c$ [Hz]
4	-0.05
6	-0.06

where z is the amplitude of the axial oscillation of the ions in the trap.

We can now calculate values for the frequency shifts due to two lowest order terms due to trap imperfections. The values obtained will represent a worst-case scenario as during the quadrupolar excitation process an ion initially executing pure magnetron motion will spend the same amount of time with a magnetron amplitude greater than the cyclotron amplitude as with the reverse [42] and the effect will cancel.

We will assume that $\rho_+ = 0$ mm and $\rho_- = 1$ mm. This assumption is justified by theoretical fits to experimental resonance curves obtained with LEBIT. There is a small amount of radial energy pickup during the injection process, but the initial ρ_+ is typically two orders of magnitude less than the initial ρ_-, and is therefore negligible. Injection simulations have estimated the average axial oscillation amplitude to be ρ_z $\approx$ 3 mm. The trap is typically operated with $U_o = 25$ V and the magnetic field is about 9.4 T. The frequency shift terms are mass dependent, but very weakly. In any case, we will choose a mass with A = 40. Table 3.2.1 shows the maximum frequency shifts, $\Delta\nu_c$, associated with the octupole and dodecapole electric field components.

Now we can consider to what extent these frequency shifts will affect mass measurements. As mentioned in Sec. 3.1.3, the experimental quantity which one measures in a Penning trap mass measurement is the ratio, R = $\nu_c/(\nu_c)_{ref}$ of cyclotron fre-

quencies. Assuming that $\Delta\nu_c = (\Delta\nu_c)_{ref} = \Delta\nu$ the relative ratio shift will be

$$\frac{\Delta R}{R} \approx 1 - \frac{\nu_{c,ref}}{\nu_c}\frac{\nu_c + \Delta\nu}{\nu_{c,ref} + \Delta\nu} \tag{3.17}$$

$$\approx \frac{\Delta\nu}{\nu_c}\left(\frac{A_{ref} - A}{A}\right) \tag{3.18}$$

where $\Delta\nu = (\Delta\nu)_{C_4} + (\Delta\nu)_{C_6}$, A_{ref} is the mass number of the reference ion, and A is the mass number of the ion of interest. Using the parameters outlined above the relative deviation from R for an ion with a mass number A = 51 as a function of the difference between the masses of the ion of interest and the reference ion is linear, passing through zero at $\Delta A = 0$, with a slope of $\approx 8{\times}10^{-10}$ $\Delta\mathrm{A}^{-1}$.

3.3 Minimizing effects due to magnetic field imperfections

Frequency shifts associated with the magnetic field occur when the magnetic field is not homogenous. There are two primary causes of inhomogeneity in the magnetic field: external field contributions, and the introduction of foreign material into the magnetic field. As mentioned in Sec. 3.2 the LEBIT 9.4 T magnet is equipped with active-shielding coils which minimize the effect of variable, external magnetic fields. In the interest of keeping the magnetic field within the trapping region of the Penning trap as homogenous as possible two factors are important: the material which constitutes the trap must be minimized, and the effect of each type of material must be minimized by appropriate design. The LEBIT Penning trap is constructed from two materials, oxygen-free copper for the electrodes and Alumina for the insulators. It is important to make the induced magnetic field from each type of material constant in the trapping region. It is not a good idea to try to compensate for deviations caused by the electrodes by adjusting the insulators, or vice versa. This is because the magnetic susceptibilities are not precisely known and are temperature dependent.

Constant offsets in the magnetic field induced by the two materials are not a primary concern as they do not introduce amplitude-dependent frequency shifts.

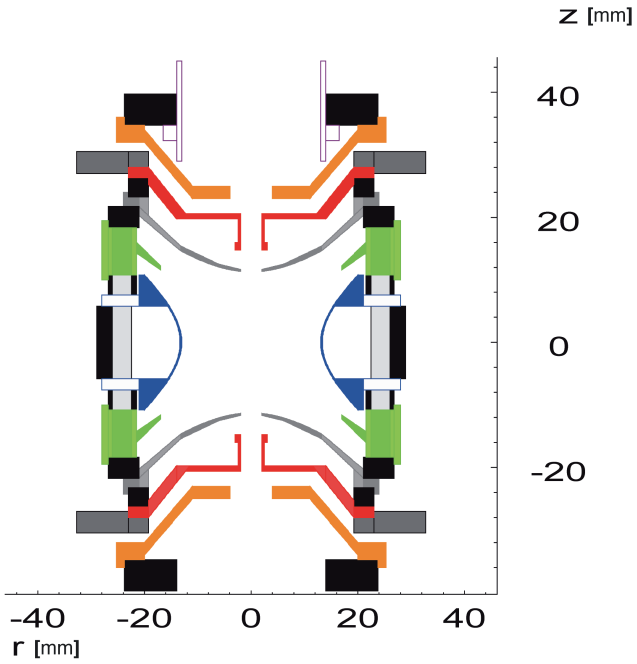

Figure 3.13. SUSZI geometry of the LEBIT Penning trap. (color version) Different colors represent the different electrodes and insulator components. Lighter shades are materials with a density less than 1 to simulate pumping holes or support legs.

To determine the induced magnetic fields I used SUSZI [48], a code developed by Stefan Schwarz. SUSZI allows you to define a trap geometry, see Fig. 3.13, by specifying equations which describe individual trap components in 2D. The program calculates the induced magnetic field on the axis of the trap by creating a grid over the model and calculating the contribution to the total induced magnetic field due to each grid unit. In my simulations I used a grid size of 0.01 mm^2. Reducing the grid size further did not change the results. The individual components can be assigned a magnetic susceptibility. I used -6.0×10^{-6} for the Alumina pieces and -3.8×10^{-7} for the copper pieces.

Fig. 3.14 displays the results of the SUSZI calculation, plotting the induced magnetic field contribution, $\Delta B/B$, as a function of axial displacement for the copper

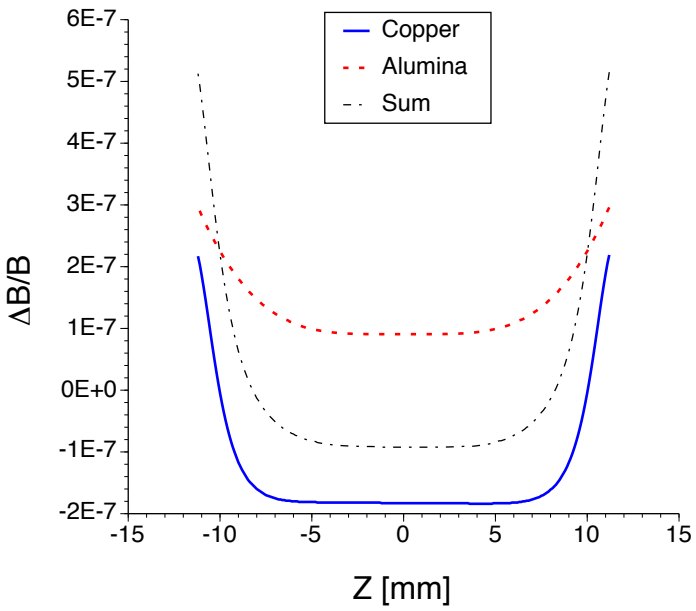

Figure 3.14. Induced magnetic field contribution, ΔB/B as a function of axial position, z. The individual contribution from the electrodes (copper) and the insulators (Alumina) are plotted together with their sum.

electrodes, the insulators, and their sum. Note that the copper and Alumina curves are constant in the middle of the trap.

Since the magnetic field imperfections are symmetric about the z = 0 plane the lowest order component of the magnetic field deviation will be the quadrupole term, which is expressed as

$$B_z = B_o \left[1 + \beta_2 \left(z^2 - \frac{r^2}{2} \right) \right] \tag{3.19}$$

where B_o is the base magnetic field strength. Then, according to [42] the cyclotron frequency shift is given by

$$\Delta\omega_c = \beta_2 \omega_c \left[z^2 - \frac{\rho_+^2}{2} \left(1 - \frac{\omega_c}{\omega_+ - \omega_-} \right) - \frac{\rho_-^2}{2} \left(1 + \frac{\omega_c}{\omega_+ - \omega_-} \right) \right]. \tag{3.20}$$

If we use the approximation $\omega_+ - \omega_- \approx \omega_c$, then

$$\Delta\omega_c = \beta_2 \omega_c (z^2 - \rho_-^2). \tag{3.21}$$

By taking the sum data shown in Fig. 3.14 and performing a least-squares fit to a second order polynomial it is possible to extract the β_2 term. Fig. 3.15 shows the

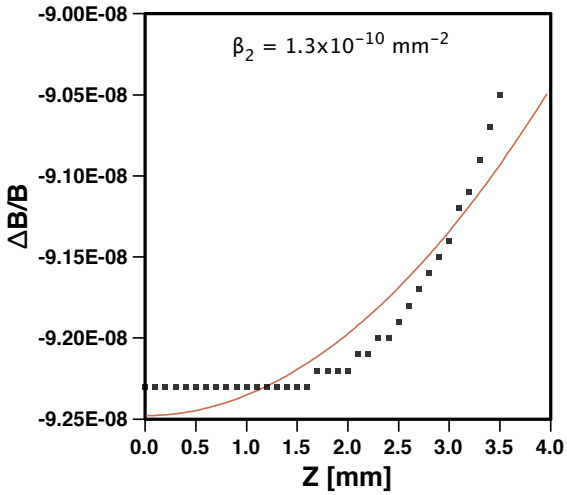

Figure 3.15. Fit to sum data from Fig. 3.14 from z = 0 mm to z = 3.5 mm. The fit yields a $\beta_2 = 1.3\times10^{-10}$ mm^{-2}.

sum data from z = 0 mm to z = 3.5 mm and least-squares fit, which yields $\beta_2 = 1.3\times10^{-10}$ mm^{-2}. An overall relative shift of the magnetic field of $\approx 9\times10^{-8}$ is observed. Fig. 3.16 plots $\Delta\nu_c/\nu_c$ as a function of the axial oscillation amplitude for four different values of ρ_-. The maximum ρ_- allowed by the entrance and exit holes of the LEBIT Penning trap is 2 mm. If we assume a ρ_- of 2 mm then the maximum relative frequency shift is $\Delta\nu_c/\nu_c \approx \pm\ 1\times10^{-9}$.

The relative deviation of the measured frequency ratio due to magnetic field imperfections is found to be

$$\frac{\Delta R}{R} \approx \beta_2(\Delta z - \Delta\rho_-), \tag{3.22}$$

where $\Delta z = z^2_{ref}$ - z^2 and $\Delta\rho_- = \rho^2_{-,ref}$ - ρ^2_-. The relative deviation of R is zero in the case that amplitudes of the axial and magnetron motions are the same for both ion species.

Experimentally it is not difficult to ensure that the difference between $\rho_{-,ref}$ and ρ_- is small, and a 10% difference is a conservative estimate. Similarly, the difference in the axial oscillation amplitude should not be very great as it depends on a well-controlled timing sequence. For 10% differences in amplitudes not exceeding 2 mm

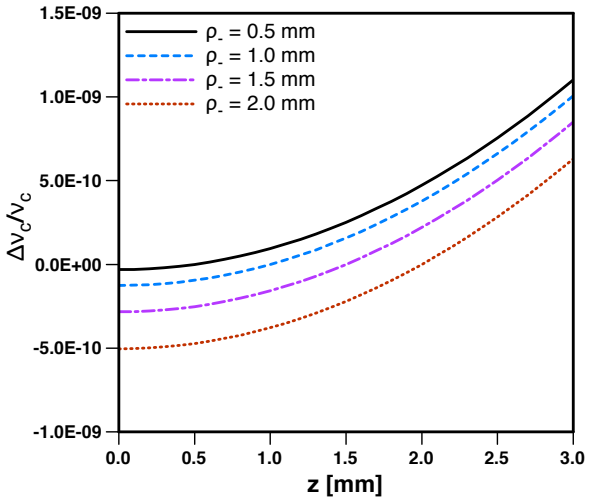

Figure 3.16. $\Delta\nu_c/\nu_c$ as a function of the axial oscillation amplitude, z, for four different values of ρ_- for $\beta_2 = 1.3\times10^{-10}$ mm^{-2}.

the relative shifts will be below 10^{-10}.

3.4 Penning trap injection/ejection optics

Fig. 3.17 shows a photograph of the complete Penning trap injection/ejection optics system, including the Penning trap (see also Fig. 3.10). These ion optical systems are inserted into the bore of the magnet. The injection optics is composed of eight drift tube sections and a field termination plate located just before the trap. They are used to decelerate the ion bunch delivered from the cooler/buncher with a kinetic energy of K $\approx$ 2 keV·Q to K $\approx$ a few eV when entering the Penning trap. One element of the injection optics is the "Lorentz" steerer, which is a new technique used to prepare the ion bunch for a quadrupolar excitation during the injection process and is described in Chapter 5. Detailed SIMION simulations have been performed to optimize the voltages applied to the individual ion optical elements such that a space focus is created at the trap center.

The ejection optics consists of five drift tubes and their purpose is to guide the

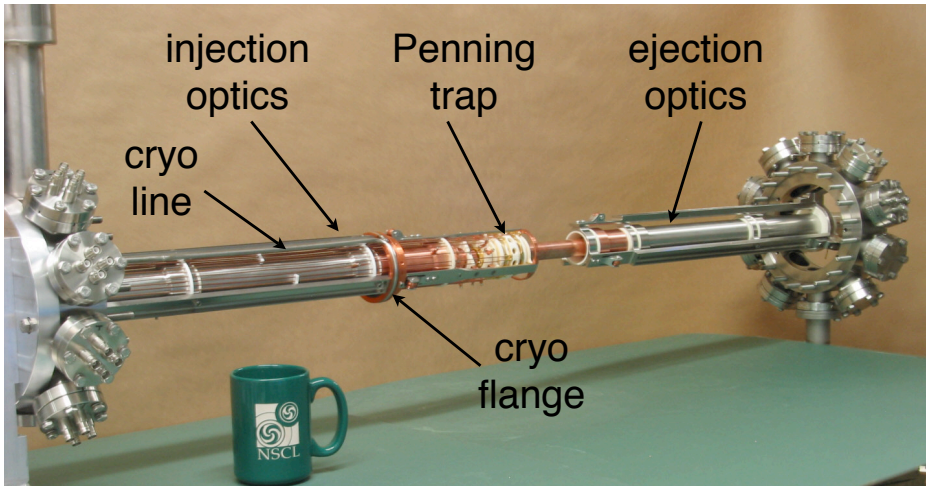

Figure 3.17. Photograph of the complete injection/ejection optics system with Penning trap.

ion bunch out of the Penning trap, through the magnetic field to the MCP detector located at the end of the system. The ions typically travel through the first drift tube with an axial kinetic energy of K $\approx$ 30 eV·Q. By the time the ions have reached the end of the ejection optics they have an axial kinetic energy of K $\approx$ 1.8 keV·Q, plus whatever energy they gained as a result of an RF excitation in the Penning trap. SIMION simulations have been performed to optimize the location of the beam spot on the MCP, and to increase the the time-of-flight separation between ions that have gained radial energy during the quadrupolar excitation and the baseline. Fig. 3.18 shows a schematic drawing of the injection and ejection ion optics with typical voltages listed.

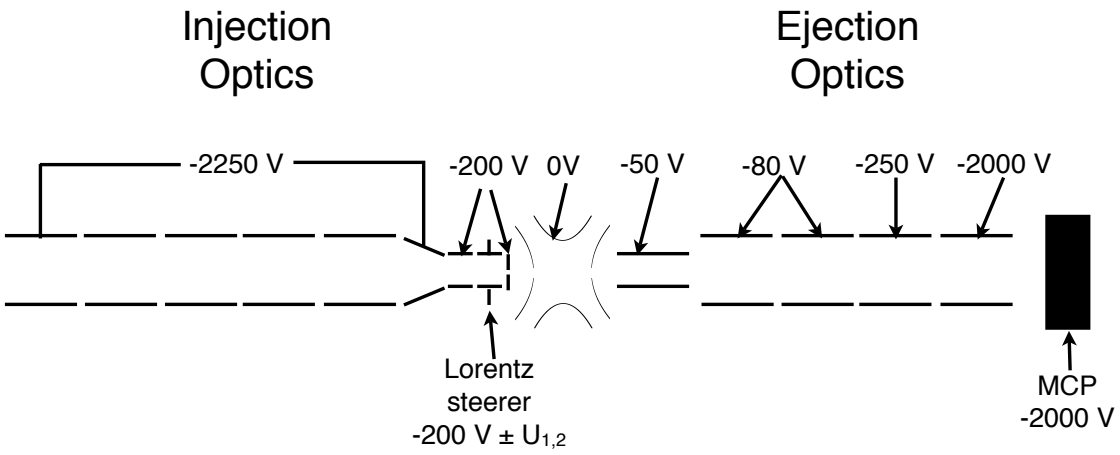

Figure 3.18. Schematic drawing of the injection/ejection ion optical elements with typical voltages.

CHAPTER 4

Study of the classical quadrupolar and new octupolar excitation schemes

4.1 Introduction

Within this work detailed aspects of the quadrupolar excitation as presently used for mass determination were investigated. In particular, the phase dependence of the quadrupolar excitation was studied, which has never been studied in detail. In addition, ion motion excitation using an octupole RF field was investigated and demonstrated for the first time. An octupolar excitation in a Penning trap is achieved by applying a octupole RF field at frequency $2\nu_c$, instead of a quadrupole field at ν_c, and requires an eight-fold segmentation of the electrode to which the RF is applied. Using this new excitation scheme it may be possible to increase the resolving power of Penning trap mass measurements.

4.2 The quadrupolar excitation revisited

In order to provide some background for the discussion of both quadrupolar and octupolar excitations the major steps leading to the equations of motion for a quadrupolar excitation, as derived in [3], will be briefly reviewed.

4.2.1 Equations of motion

Begin by introducing the vectors $\overrightarrow{V}^+$ and $\overrightarrow{V}^-$ [41] such that

$$\overrightarrow{V}^{\pm} = \dot{\overrightarrow{\rho}} - \omega_{\mp} \cdot \overrightarrow{\rho} \times \hat{e}_z, \tag{4.1}$$

where $\overrightarrow{\rho}$ is the ion's position vector. Additionally,

$$\begin{aligned} x &= -\frac{V_y^+ - V_y^-}{\omega_+ - \omega_-} \\ y &= \frac{V_x^+ - V_x^-}{\omega_+ - \omega_-}, \end{aligned} \tag{4.2}$$

where x and y are the ion's position in Cartesian coordinates. Eq. 4.1 successfully decouples the equations of motion of an ion confined in a Penning trap. Using this coordinate transformation and applying the rotating wave approximation the equations of motion can be solved [3] for an ion subjected to an applied quadrupolar RF field. The solution is

$$\begin{aligned} \rho_{\pm}(t) = \; & [\rho_{\pm,o}\cos(\omega_B t) \mp \tfrac{1}{2}\frac{\rho_{\pm,o}[i(\omega_{rf}-\omega_c)]+\rho_{\mp,o}k_o^{\pm}}{\omega_B} \\ & \times \sin(\omega_B t)]e^{\frac{i}{2}(\omega_{rf}-\omega_c)t}, \end{aligned} \tag{4.3}$$

where $\rho_{\pm}$(t) are the magnitudes of the cyclotron and magnetron radii as a function of time and $\rho_{\pm,o}$ are the initial cyclotron and magnetron radii. Additionally,

$$\omega_B = \frac{1}{2}\sqrt{(\omega_{rf}-\omega_c)^2 + k_o^2} \tag{4.4}$$

and $\mathrm{k}_o^{\pm} = \mathrm{k}_o \mathrm{e}^{\pm i\Delta\phi}$ where $\mathrm{k}_o = \frac{U_{rf}}{2a^2}\frac{q}{m}\frac{1}{\omega_+ - \omega_-}$. Here, q is the ionic charge, m is the ionic mass, U_{rf} is the applied RF amplitude, a is the radius at which the RF is

applied and

$$\Delta\phi = \phi_{rf} - (\phi_+ + \phi_-). \tag{4.5}$$

ϕ_{rf} is the phase of the applied RF and $\phi_\pm$ are the cyclotron and magnetron phases. As stated above, radial energy gained during the excitation process is detected via a reduced time of flight of ions ejected from the trap to the detector. Under normal conditions $\omega_+ \gg \omega_-$, so we can write the radial energy as $\mathrm{E}_r(\mathrm{t}) \approx \frac{1}{2}\mathrm{m}\omega_+^2\rho_+^2(\mathrm{t})$.

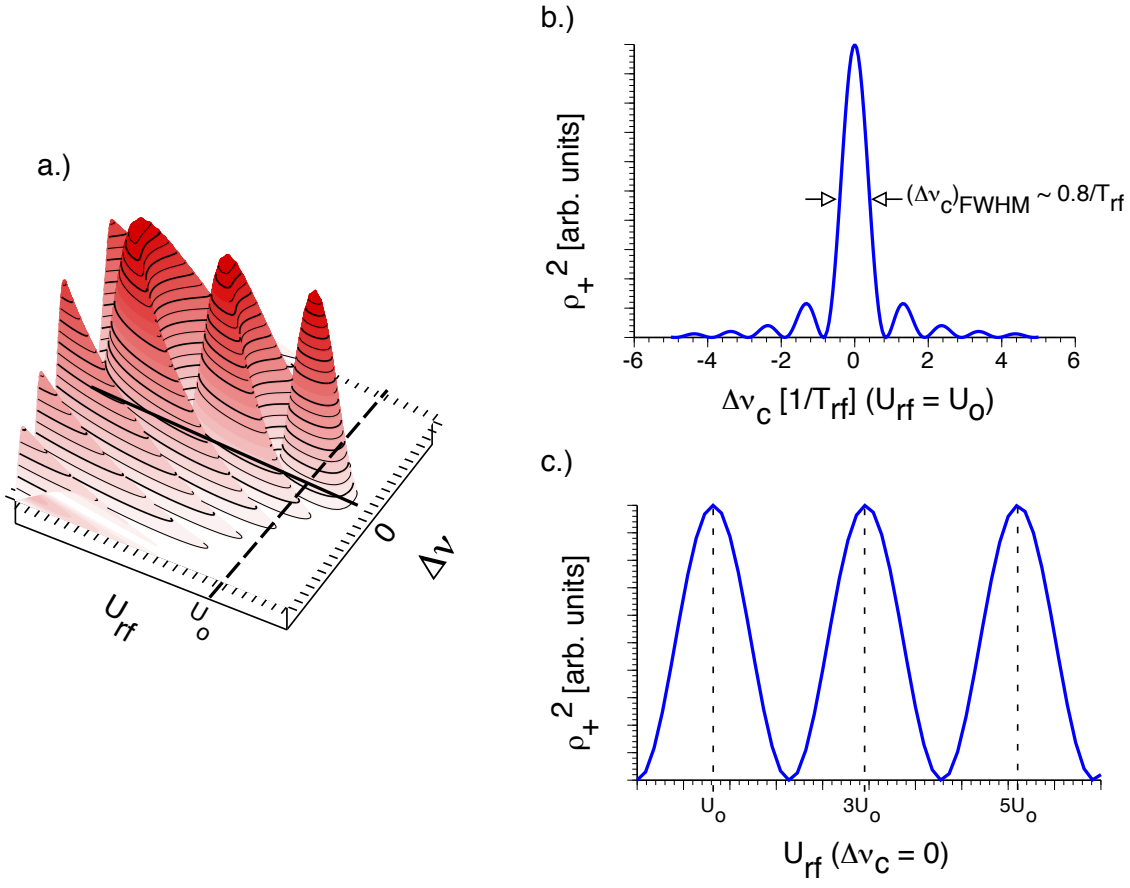

Figure 4.1. (a) surface plot of ρ_+^2 as a function of U_{rf} and ν_{rf} for a given excitation time T_{rf}. (b) cut from plot (a) at $\mathrm{U}_{rf} = \mathrm{U}_o$. Full conversion from magnetron to cyclotron motion is achieved at $\Delta\nu_c = \nu_{rf}$ - $\nu_c = 0$. (c) slice from plot (a) at $\Delta\nu = 0$ illustrating the beating of ρ_+^2 as a function of U_{rf}.

Fig. 4.1(a) shows a 3D plot of the calculated values of ρ_+^2, which is proportional

to the gained energy, as a function of U_{rf} and frequency detuning for a given T_{rf} for a single ion initially executing pure magnetron motion, $\rho_{+,o} = 0$. Fig. 4.1(b) shows a cut at $U_{rf} = U_o$, which is the excitation amplitude at which a full conversion of magnetron to cyclotron motion has occurred for $\nu_{rf} = \nu_c$. The width of the resonance curve is given by theory as $\Delta\nu_{FWHM} \approx 0.8/T_{rf}$. Such a response is reflected in the experimental resonance curve shown in Fig. 4.2. Fig. 4.1(c) is a cut along $\Delta\nu = \nu_{rf}$ - $\nu_c = 0$ illustrating the change of ρ_+^2 as a function of U_{rf} for a constant excitation time.

Calculating the energy gain from the excitation and accounting for the ejection optics and magnetic field it is possible to calculate the theoretical line shape [3] expected for the time-of-flight measurement. This shape has been used to fit the experimental data shown in Fig. 4.2. Due to a nonlinear conversion between radial energy and time of flight, the full width of the time-of-flight curve is $0.9/T_{rf}$ for LEBIT.

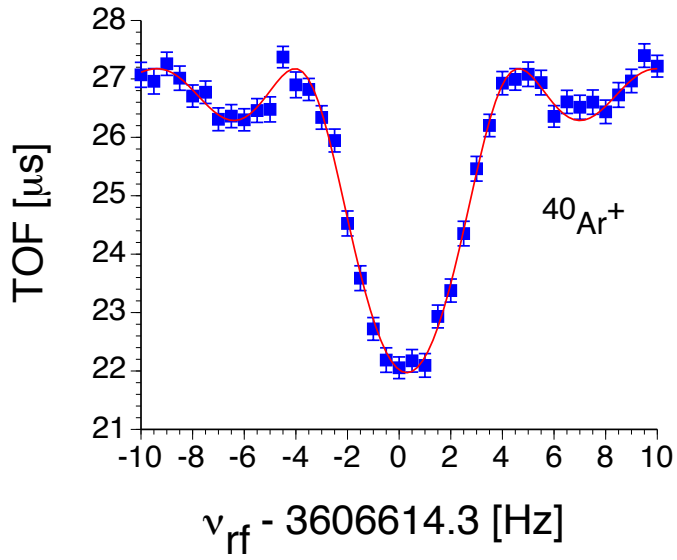

Figure 4.2. TOF line shape obtained from a quadrupolar excitation of $^{40}Ar^{+}$ with excitation time $T_{rf} = 200$ ms. The solid line is a fit [3] of the theoretical line shape to the data.

4.2.2 Phase dependence of the quadrupolar excitation

The solution to the equations of motion as derived in [3] contains a phase dependence, the consequence of which has not been previously investigated. The phase dependence appears in Eq. 4.3 through the $k_o^{\pm}$ term. We algebraically expand

$$\begin{aligned}\rho_+(t)\rho_+(t)^* = \quad & \frac{4\rho_{+,o}^2\omega_B^2\cos^2(\omega_B t)}{4\omega_B^2} + \frac{k_o^2\rho_{-,o}^2+\rho_{+,o}^2(\omega_{rf}-\omega_c)^2}{4\omega_B^2}\sin^2(\omega_B t) \\ & -\frac{k_o\rho_{-,o}\rho_{+,o}(\omega_{rf}-\omega_c)\sin(\Delta\phi)}{4\omega_B^2}\sin^2(\omega_B t) \\ & -\frac{2k_o\rho_{-,o}\rho_{+,o}\omega_B\cos(\Delta\phi)}{4\omega_B^2}\sin(2\omega_B t).\end{aligned} \tag{4.6}$$

The phase dependence of the radial energy change is located in the third and fourth terms of Eq. 4.6. Both terms scale with the product of $\rho_{+,o}$ and $\rho_{-,o}$, which means if the ions begin in a state of pure cyclotron or magnetron motion at the beginning of the excitation the effect will not be present.

Fig. 4.3 presents the results of simulations of quadrupolar resonances for single $^{39}K^+$ ions with $T_{rf} = 1$ s. Both simulations were performed with $\rho_{-,o} = 1$ mm and $\phi_{+,o} = \phi_{-,o} = 0°$. An initial cyclotron radius of $\rho_{+,o} = 0.1$ mm was used on the left and $\rho_{+,o} = 0.4$ mm was used on the right. In each case the value of U_{rf} was adjusted such that in resonance and for $\phi_{rf} = 0°$ the radial energy was maximized. Looking closely at the contour plot on the left one can see a distortion of the central peak and a shift in the position of the side bands as $\Delta\phi$ changes. Resonance profiles for which $\Delta\phi = 90°$ and $270°$ become asymmetric and the position of the minimum time of flight has shifted slightly. Increasing the value of $\rho_{+,o}$ to 0.4 mm only exacerbates the situation. The most obvious implication of these phase-dependent effects involve low-statistics measurements where $\Delta\phi$ is allowed to vary. If the measurement samples any particular phase range more frequently and the resonance is fit with a line shape with a symmetric center then the analysis will include an additional error.

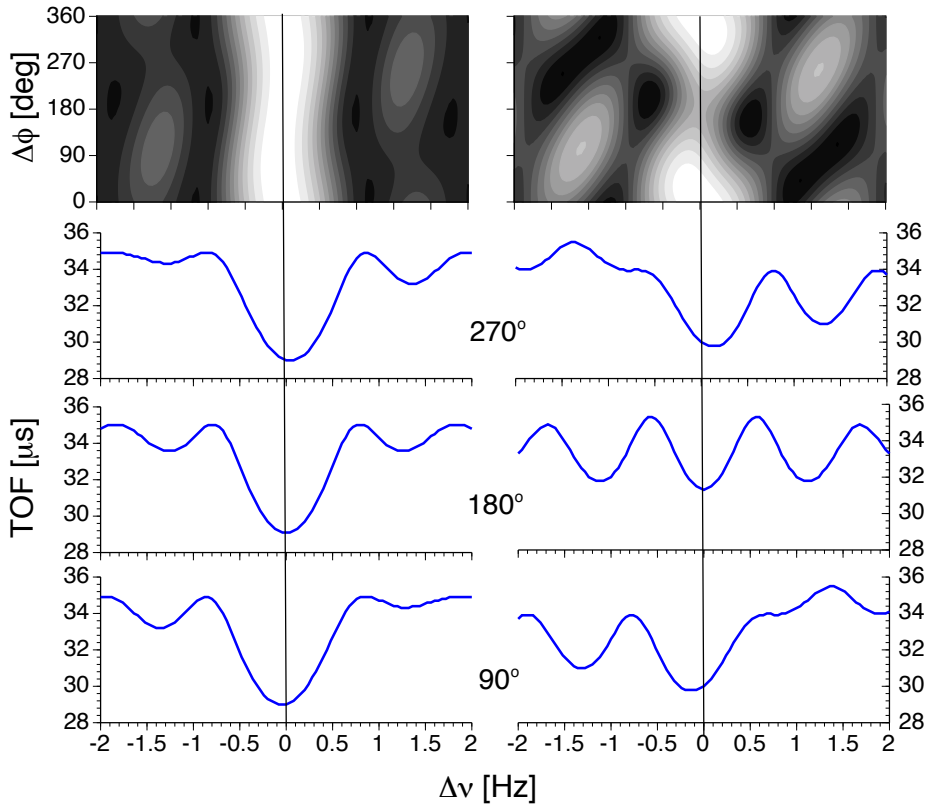

Figure 4.3. Simulations of quadrupolar resonances for single $^{39}K^{+}$ ions with T_{rf} = 1 s. The two plots in the top row are contour plots of the resonances as a function of $\Delta\phi$ and $\Delta\nu$. Below are cuts at given values of $\Delta\phi$. Both simulations were performed with $\rho_{-,o} = 1$ mm and $\phi_{+,o} = \phi_{-,o} = 0°$. An initial cyclotron radius of $\rho_{+,o} = 0.1$ mm was used on the left and $\rho_{+,o} = 0.4$ mm was used on the right.

In order to see the phase dependence in the radial energy change of the quadrupolar excitation, two conditions must be met. The first is that the RF voltage must have a defined phase relation to initial ion motion. $\Delta\phi$ must not be random which means, according to Eq. 4.5, that all individual phases must be well defined. If this is not the case then the final line shape will be an average over the line shapes of random $\Delta\phi$'s. The second condition is that the ion ensemble cannot begin in a pure state of cyclotron or magnetron motion.

For the test of this phase dependence $^{39}K^{+}$ ions were injected into the Penning trap, and an initial magnetron motion was introduced with the Lorentz steerer. The

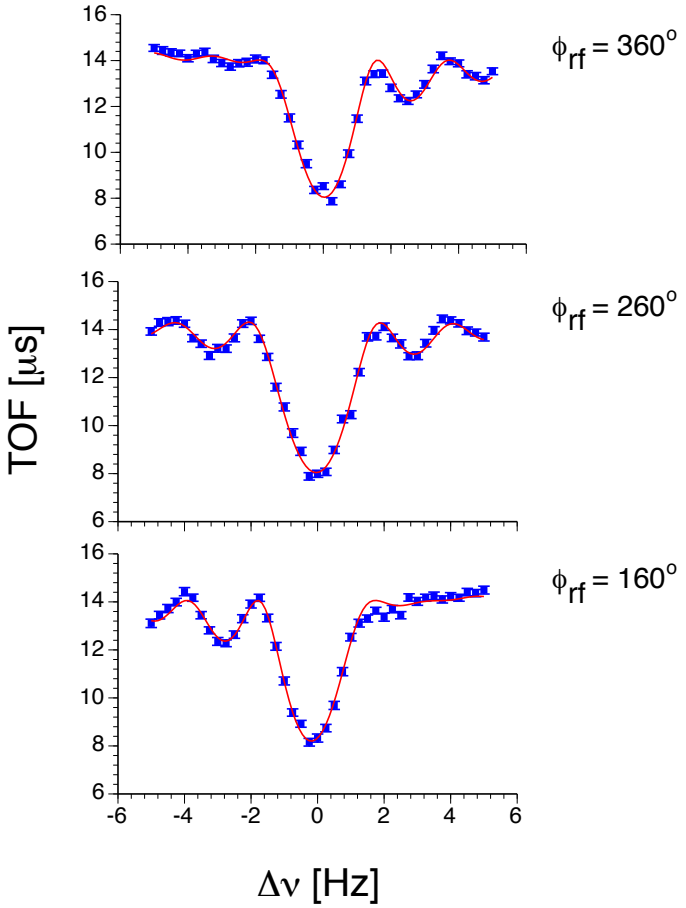

Figure 4.4. Three $^{39}K^{+}$ quadrupolar resonances for T_{rf} = 500 ms measured for different values of ϕ_{rf}. The solid line is the fit of the theoretical line shape.

excitation RF was phase locked to the time of ion capture in the trap, which defines the initial phase of the ion motion. Several resonances with T_{rf} = 500 ms were taken with varied values of ϕ_{rf}. Fig. 4.4 illustrates the effect of varying ϕ_{rf} on the resonance shape. Here we see experimentally how the sidebands change shape as the value of $\Delta\phi$ is changed. When $\Delta\phi$ is allowed to be a free parameter a good agreement is obtained between the experimental data and the fit. All three fits yield consistent values for $\rho_{-,o}$ = 0.91(2) mm and $\rho_{+,o}$ = 0.11(1) mm. For each resonance ϕ_{rf} was incremented by 100°. Within 20% this phase dependence was reproduced in the fit parameter $\Delta\phi$.

As discussed earlier, only the third and fourth terms of Eq. 4.6 contain a $\Delta\phi$ term and contain the product of $\rho_{+,o}$ and $\rho_{-,o}$. While $\rho_{-,o}$ is introduced deliberately, a finite $\rho_{+,o}$ must be the result of an asymmetric injection of ions into the magnetic field of the Penning trap which leads to a pickup of cyclotron motion. If the amount of radial energy gained during the injection process can be reduced, then $\rho_{+,o}$ will be reduced, thus reducing the phase-dependent effect. This could be useful in fine-tuning the injection of ions into a Penning trap.

4.3 Octupolar excitation

Excitation of ion motion in a Penning trap by application of an octupolar RF field at frequencies near $2\nu_c$ have been studied experimentally and in simulations. Single-ion simulations were used to explore the resonant response of ρ_+^2 for a variety of initial conditions. Simulations utilizing realistic distributions of multiple ions were used to predict resonance profiles under realistic conditions. Two independent codes were developed and used in these studies: a fourth-order Runge-Kutta routine written in Fortran and compiled on a Microsoft Windows operating system, and a fourth-order Runge-Kutta routine with adaptive step size control written in C++ and compiled on an OSX operating system.

Experimental results together with those from simulation are used to make estimates of the distribution for initial conditions. In many cases 2D simulation results have been presented to illustrate the scope of the simulations performed. In practice, though, the agreement between experimental and simulation data is more clearly observed by presenting projections of the data.

4.3.1 The octupolar field

Since much of what we learn from the octupole excitation will be based on simulation it is important to adequately outline the methods employed should anyone care to reproduce the results given here. Bearing this in mind I will present the formulation of the octupole field orientation which I used and the associated equations of motion which can be solved numerically (using a Runge-Kutta routine [49] in the present work). The expansion for the charge distribution, $\phi_\circ$, is

$$\phi_o = ax^4 + bx^3y + cx^2y^2 + dxy^3 + ey^4. \tag{4.7}$$

Since the space is charge free it must satisfy the Laplace Equation, $\bigtriangledown^2\phi = 0$. Applying this condition to Eq. 4.7 yields the following conditions:

$$\begin{array}{rcrcl} 6a & + & c & = & 0 \\ b & + & d & = & 0 \\ c & + & 6e & = & 0 \end{array} \tag{4.8}$$

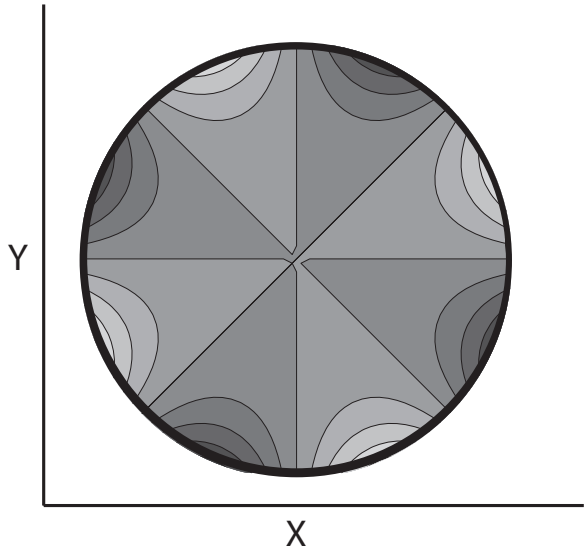

Figure 4.5. Octuoplar RF field configuration used in simulations shown at t = (2n+1)$\pi/(2\omega_{rf})$. Nodes are located at (2n+1)$\pi/8$. Generated with b = -d = 1 and a = c = e = 0 in Eq. 4.8.

Choosing a nontrivial set of parameters which satisfy Eq. 4.8 yields an equation describing a valid octupole field. Different parameters correspond to a rotation of the

field's orientation in space. For illustration we will choose a=c=e=0 and b=-d=1. This is the orientation used in all of the calculations, and is shown in Fig. 4.5.

Calculating the electric field produced by a time-varying octupolar field produced by a set of electrodes at a radius a from the trap center yields the following field components:

$$\begin{aligned} E_x &= \frac{U_{rf}}{a^4}\sin(\omega_{rf}t+\phi_{rf})(y^3-3x^2y) \\ E_y &= -\frac{U_{rf}}{a^4}\sin(\omega_{rf}t+\phi_{rf})(x^3-3xy^2). \end{aligned} \tag{4.9}$$

Writing out the full equations of motion of an ion in a Penning trap subjected to an octupolar RF field using the transformation given in Eq. 4.2 yields

$$\begin{aligned} \dot{V}_x^{\pm} &= -\omega_{\pm}V_y^{\pm} - k\frac{(V_x^+-V_x^-)^2[(V_x^+-V_x^-)^2-3(V_y^+-V_y^-)^2]}{(\omega_+-\omega_-)^3} \\ \dot{V}_y^{\pm} &= \omega_{\pm}V_x^{\pm} + k\frac{(V_y^+-V_y^-)^2[(V_y^+-V_y^-)^2-3(V_x^+-V_x^-)^2]}{(\omega_+-\omega_-)^3} \end{aligned} \tag{4.10}$$

where

$$k = \frac{U_{rf}}{a^4}\frac{q}{m}\sin(\omega_{rf}t+\phi_{rf}). \tag{4.11}$$

Unfortunately, the transformation does not decouple the equations of motion. The ansatz presented in [3], $\overrightarrow{V}^{\pm} = \overrightarrow{A}^{\pm}(\mathrm{t})\mathrm{e}^{\pm i(\omega_{\pm}+\phi_{\pm})}$, where $A^{\pm}$ is an amplitude, does not simplify the problem. In the case of the quadrupolar excitation after the ansatz is inserted the high-frequency components can be neglected and the solution remains a physical description of the system. Following the same procedure in the case of the octupolar excitation yields a non-physical description of the system. Unless a suitable coordinate transformation is found an analytical solution may not be possible. At present, numerical solutions to the equations of motion have to be used. By calculating the vectors $\overrightarrow{V}^{\pm}$ and using Eq. 4.1 it is possible to extract ρ_+ and ρ_- as a function of time. Since $\mathrm{E}_r \propto \rho_+^2$, the radial energy pickup due to the application of an octupolar RF field is directly accessible.

4.3.2 Single-ion octupolar simulations

Octupolar excitation of the motion of a single ion will be used to illustrate the similarities and differences between the octupolar and quadrupolar excitation schemes.

Motional beating of single ions with $\nu_{RF} = 2\nu_c$

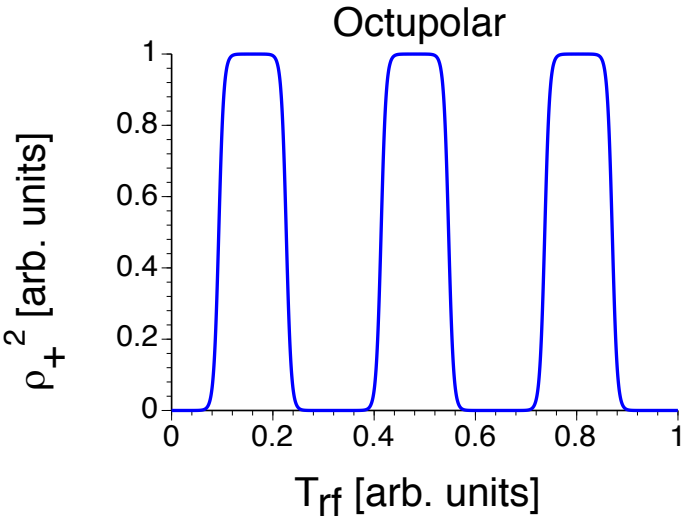

Figure 4.6. ρ_+^2 of an ion confined in a Penning trap and subjected to an azimuthal octupolar RF field at frequency $2\nu_c$.

Fig. 4.6 shows the variations of ρ_+^2 of an ion as a function of time subjected to an azimuthal octupolar RF field. The ion is initially in a state of pure magnetron motion. A periodic beat pattern is observed. Compared to the quadrupolar case (Fig. 4.1c) the beating is no longer harmonic but begins to approach a square wave in shape.

According to Eq. 4.4, the beat frequency of an ion induced by a quadrupolar RF field with $\nu_{rf} = \nu_c$ is proportional to U_{rf}, and independent of the initial ion motion. This is not the case with the octupolar excitation. Fig. 4.7 displays the ρ_+^2 of a single ion, subjected to an octupolar field with $\nu_{rf} = 2\nu_c$, for different initial magnetron radii, $\rho_{-,o}$, and applied RF amplitudes, U_{rf}. The panels on the left side display the

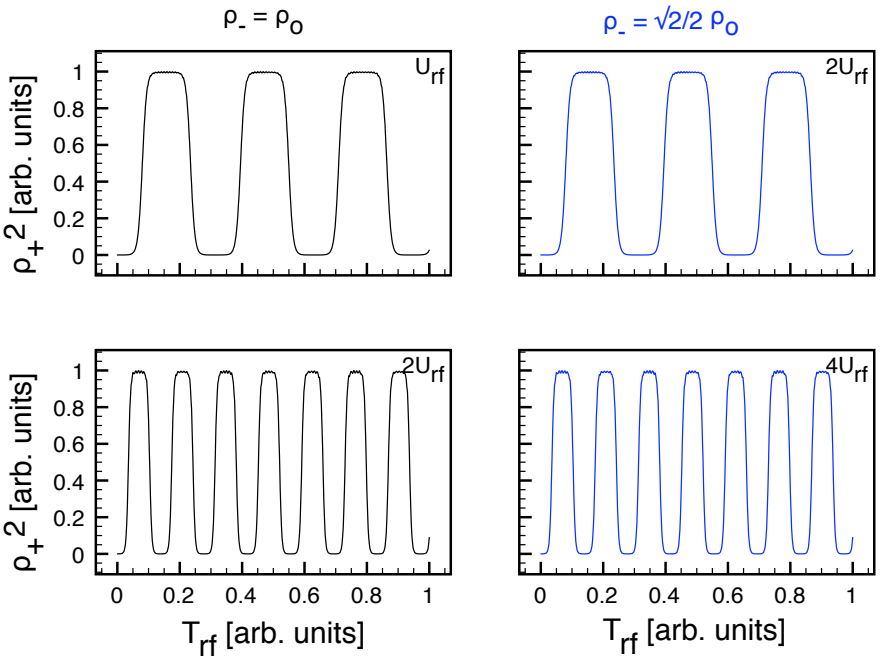

Figure 4.7. The left hand panels show ρ_+^2 as a function of T_{rf} for an ion with an initial $\rho_{-,o} = \rho_o$ and $\rho_{+,o} = 0$ with applied RF amplitudes of U_{rf} and $2U_{rf}$, respectively. The right hand panels ρ_+^2 for an ion with an initial $\rho_{-,o} = \frac{\sqrt{2}}{2}\rho_o$ and applied RF amplitudes of $2U_{rf}$ and $4U_{rf}$, respectively.

beat patterns for an ion with an initial magnetron radius of ρ_o. Doubling U_{rf} results in an increase in the beat frequency. The panels on the right side illustrate that doubling U_{rf} and scaling the initial magnetron radius by $\sqrt{2}/2$ preserves the original beat frequency. In the case of octupolar excitation the beat frequency depends not only on the excitation amplitude, but also on the initial motion of the ion in the trap.

Fig. 4.8 shows the beat frequency as a function of the initial $\rho_{-,o}$ for three different initial magnetron phases, $\phi_{-,o}$. The figure reveals that the beat frequency depends not only on $\rho_{-,o}$, but also on $\phi_{-,o}$. The dip in the $\phi_{-,o} = 0^\circ$ curve is not a numerical artifact, but has been verified by two independent simulations. By changing the phase one can change the position of this dip, but it quickly moves to a larger value of $\rho_{-,o}$ as one moves away from $\phi_{-,o} = 0^\circ$. With $\phi_{rf} = 0^\circ$ the dip occurs at $\rho_- \approx 2.1$

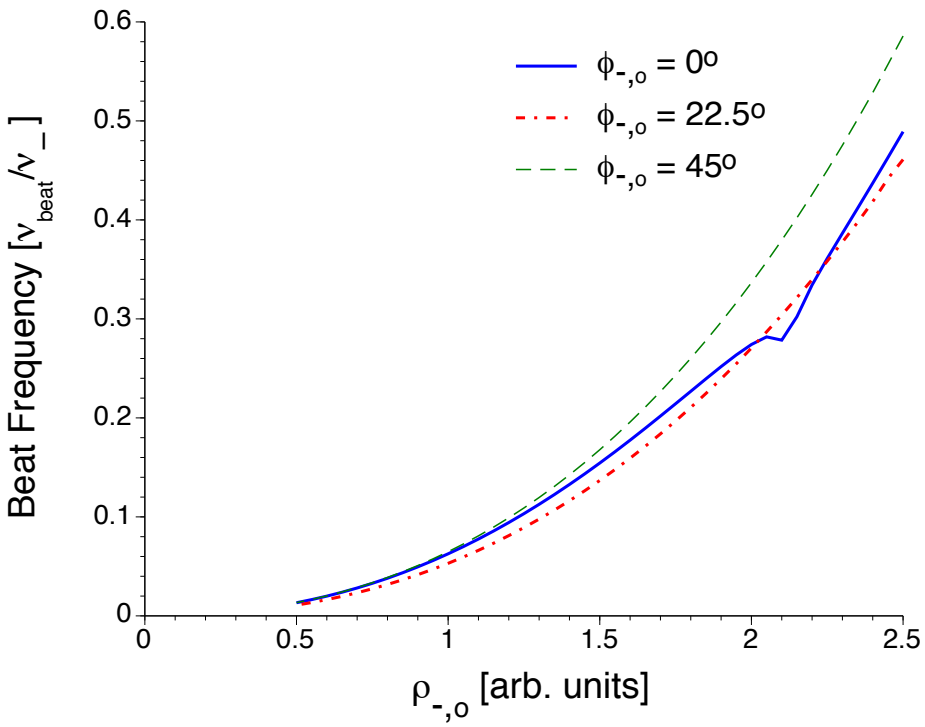

Figure 4.8. Beat frequency between magnetron and cyclotron motions as a function of $\rho_{-,o}$ for constant U_{rf} and for three initial magnetron phases, $\phi_{-,o} = 0°, 22.5°$ and $45°$.

and $\nu_{beat}/\nu_- \approx 0.26$. Fig. 4.7 might lead one to believe that $\nu_{beat} \propto \rho^2_{-,o} \cdot U_{rf}$, yet taking Fig. 4.8 into account the relation would need to be amended to $\nu_{beat} \propto f(\phi_-) \cdot \rho^2_{-,o} \cdot U_{rf}$. The effect of holding U_{rf} and $\phi_{-,o}$ constant and plotting the beat frequency as a function of $\phi_{-,o}$ can be seen in Fig. 4.9. The beat frequency seems to sample the octupolar RF field's spatial orientation, and is at a minimum at the anti-nodes, and maximum at the nodes, of the field.

According to Eq. 4.4 the beat frequency in the case of $\nu_{rf} = \nu_c$ due to a quadrupolar excitaton is linear with respect to U_{rf} and is phase independent. Again, this is different in the case of octupolar excitation. The beat frequency is not linear with respect to U_{rf}, and is dependent upon the $\phi_{-,o}$, as is illustrated in Fig. 4.10 which shows the beat frequency as a function of U_{rf}. As the beat frequency nears ν_- the beat pattern begins to lose its periodic nature. Zooming in to low frequencies and

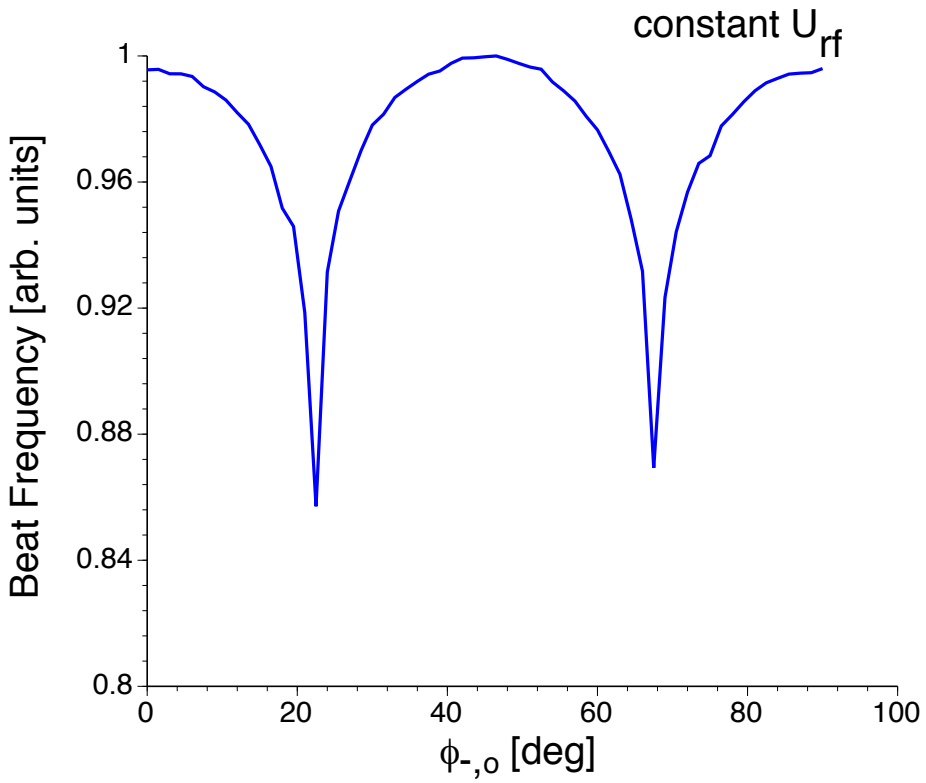

Figure 4.9. Beat frequency as a function of $\phi_{-,o}$ for a constant U_{rf}.

excitation amplitudes the $\phi_{-,o} = 0°$ and $\phi_{-,o} = 45°$ curves become indistinguishable, while the $\phi_{-,o} = 22.5°$ curve remains distinct. Again, similar to Fig. 4.8, a dip is observed in the $\phi_{-,o} = 0°$ case, again located at $\nu_{beat}/\nu_{-} \approx 0.26$.

We are now in a position to investigate a possible invariant of the motion. Fig. 4.11 shows the beat frequency when changing $\rho_{-,o}$, while at the same time keeping the product $U_{rf} \cdot \rho^2_{-,o}$ constant. It can be seen that the beat frequency is constant for a given initial phase, $\phi_{-,o}$. This was found to be true for ions in a state of pure magnetron motion, and for mixed initial motions, $\rho_o = \sqrt{\rho^2_{+,o} + \rho^2_{-,o}}$, as well. Therefore, we arrive at a general relationship $\nu_{beat} \propto \alpha(\rho_{\pm,o}, \phi_{\pm,o}, \phi_{rf}) \cdot \rho^2_o \cdot U_{rf}$, where α is a scaling factor which depends on all four of the initial ρ's and ϕ's.

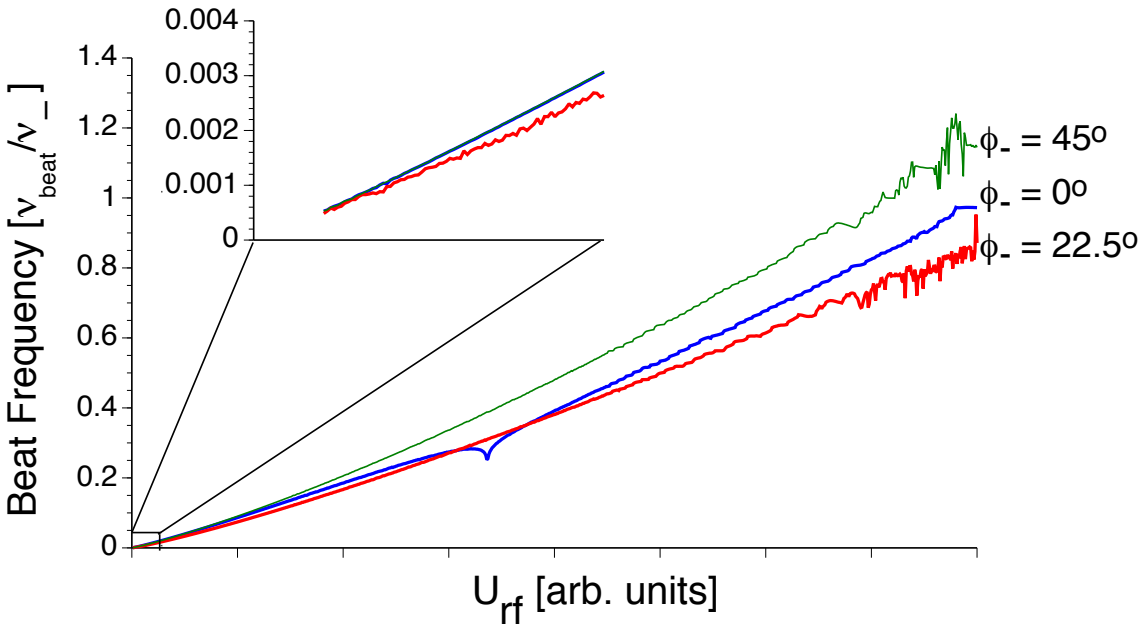

Figure 4.10. Beat frequency as a function of U_{rf} for three initial $\phi_{-,o}$'s. The insert zooms in to low beating frequencies and amplitudes.

Invariant phase relation of the octupolar excitation

According to Eq. 4.5, $\Delta\phi = \phi_{rf} - (\phi_+ + \phi_-)$ is a constant of the motion for a quadrupolar excitation. We investigate if a similar phase relation holds for the octupolar excitation.

Fig. 4.12 shows scans of ρ_+^2 as a function of $\phi_{+,o}$ and time for a given $\phi_{-,o}$ with $\phi_{rf} = 0^\circ$ in all cases. By comparing the patterns it is easy to conclude that the time dependence of ρ_+^2 is the same if $\phi_{+,o} + \phi_{-,o} = \text{const}$. It was verified that this also holds true if ϕ_{rf} is changed.

Fig. 4.13 is similar to Fig. 4.12, except $\phi_{+,o}$ is held constant at 0° and the individual panels show ρ_+^2 as a function of $\phi_{-,o}$ and time. Here we verified that for $\phi_{+,o} = 0^\circ$, $\frac{1}{2}\phi_{rf}$ - $\phi_{-,o} = \text{const}$. the same time dependence of ρ_+^2 is observed. Testing this condition for many values of $\phi_{+,o}$ yields the same results and leads us to conclude that the invariant phase in the case of octupolar excitation is $\Delta\phi = \frac{1}{2}\phi_{rf}$ - $(\phi_+ +$

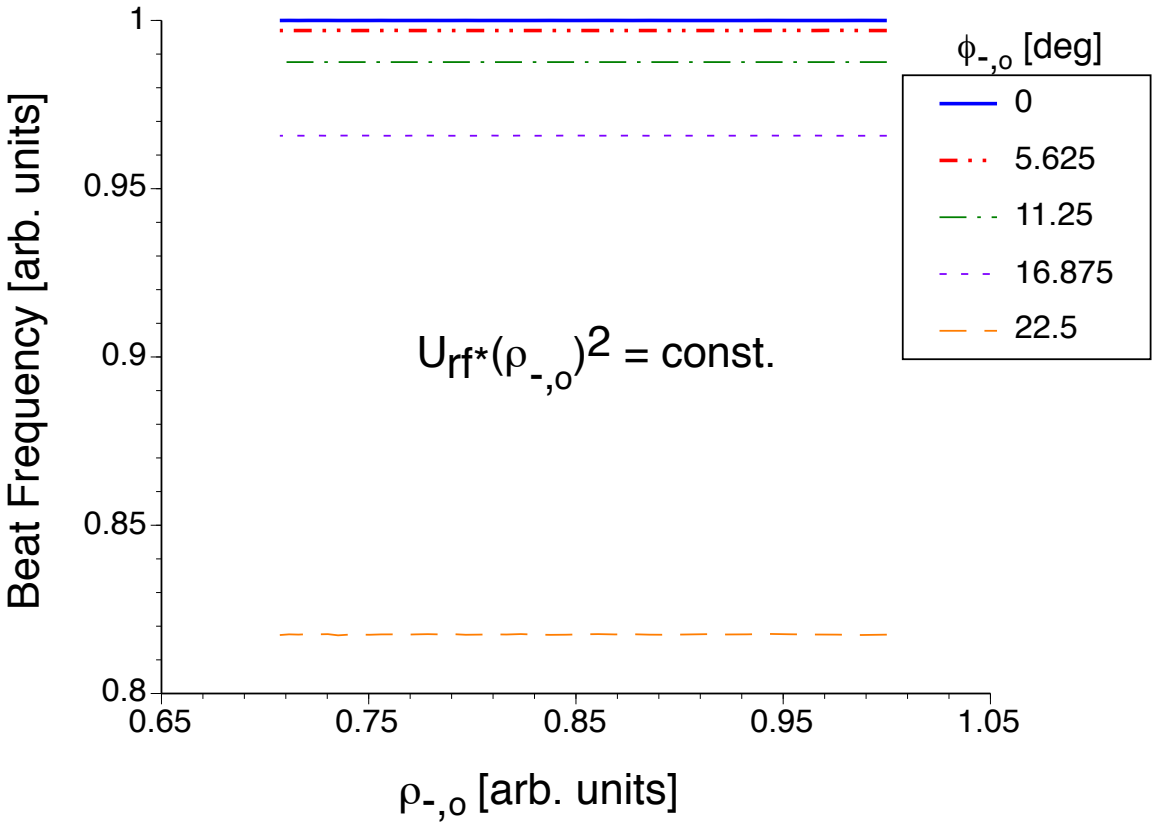

Figure 4.11. Beat frequency due to an octupolar excitation as a function of $\rho_{-,o}$ holding $\rho_{-,o}^2 \cdot U_{rf}$ constant for several values of $\phi_{-,o}$.

ϕ_-). This differs from the quadrupolar phase relation, Eq. 4.5, only in the factor of 1/2 multiplying the ϕ_{rf} term. This appears plausible as the octupolar field has twice the number of nodes and anti-nodes as the quadrupolar field. The factor of 1/2 reflects that the ions do begin their motion at the same position with respect to the field orientation.

Single-ion resonance curves

At first, we will examine octupolar resonances of single ions initially in a state where $\rho_o = \rho_{-,o}$. The general observation is a periodic change of ρ_+^2 as a function of U_{rf}. Along the line $\nu_{rf} = 2\nu_c$ a resonant effect is observed. Fig. 4.14 illustrates

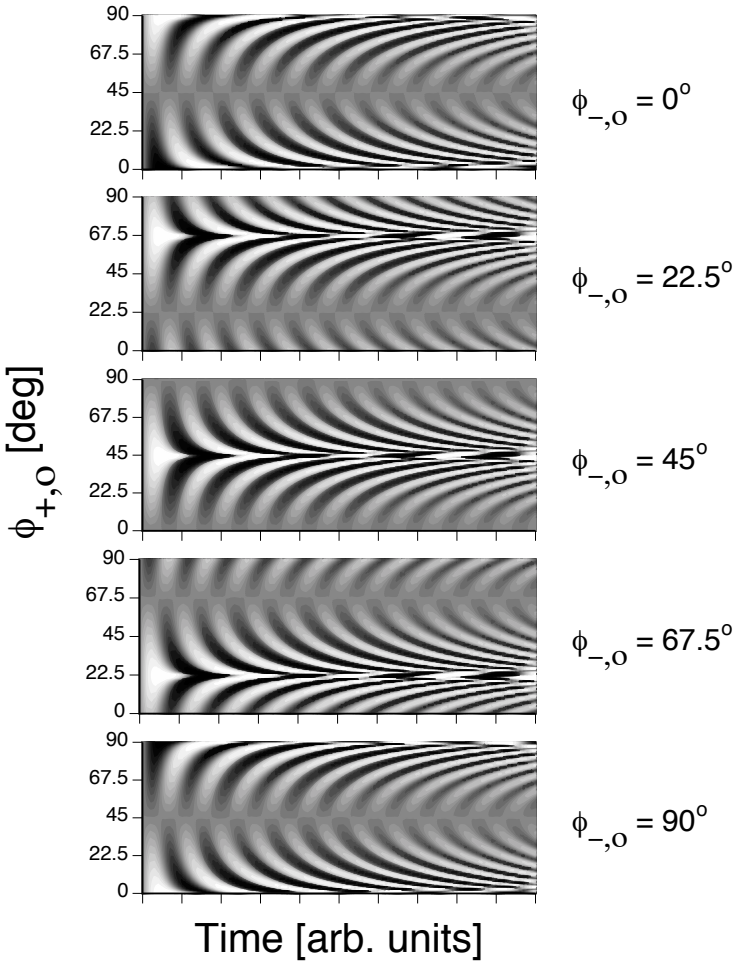

Figure 4.12. 2D simulations of ρ_+^2 as a function of time and $\phi_{+,o}$ for a given $\phi_{-,o}$ with $\phi_{rf} = 0°$. The grey scale is proportional to ρ_+^2.

the dependence of ρ_+^2 on frequency detuning, $\Delta\nu = \nu_{rf}$ - $2\nu_c$, and U_{rf} for various values of $\phi_{-,o}$. At $\phi_{-,o} = 13.5°$ a secondary resonant effect becomes visible which sweeps through the primary resonant structure as the value of $\phi_{-,o}$ is changed. This effect lies on a line with an origin at $U_{rf} = 0$ and $\Delta\nu = 0$ which rotates clockwise for increasing values of $\phi_{-,o}$. At $\phi_{-,o} = 18.0°$ the structure can be seen across all three sections of the primary resonant structure. At $\phi_{-,o} = 22.5°$ the secondary structure lies on the $\Delta\nu = 0$ line.

A close look at the resonances reveals a narrowing of the resonance profiles at $\Delta\nu$

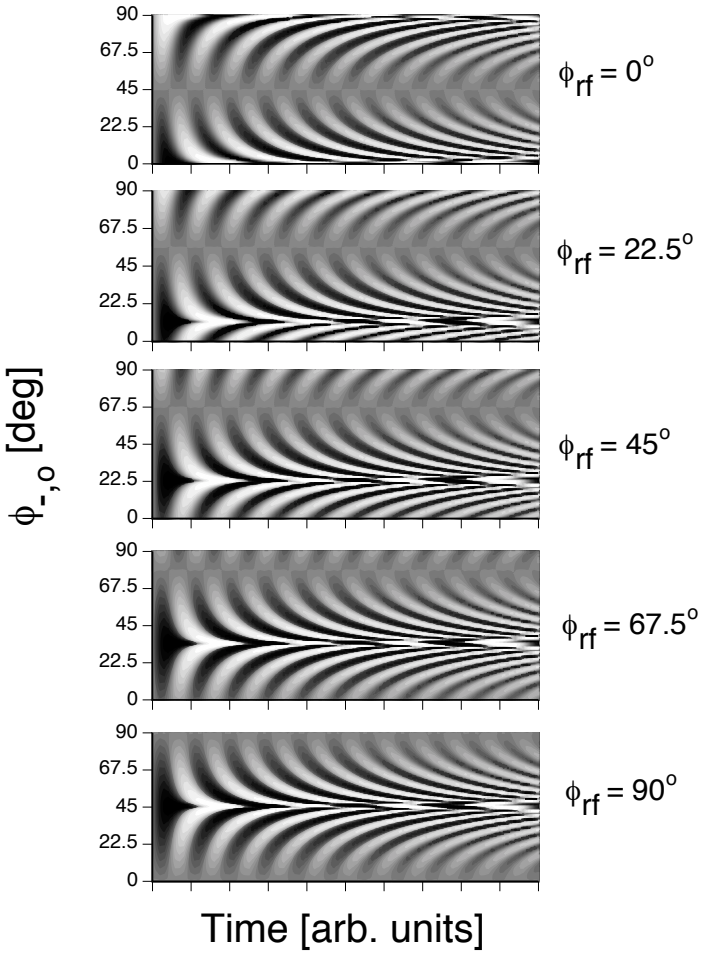

Figure 4.13. 2D simulations of ρ_+^2 as a function of time and $\phi_{-,o}$ for a given ϕ_{rf} with $\phi_{+,o} = 0^\circ$. The grey scale is proportional to ρ_+^2.

= 0 for certain values of U_{rf}. Fig. 4.15 plots 2D cuts from the $\phi_{-,o} = 0^\circ$ (left) and $\phi_{-,o} = 22.5^\circ$ (right) cases shown in Fig. 4.14. Moving from the top panels to the bottom steps through the first conversion of magnetron to cyclotron motion. The $\phi_{-,o} = 0^\circ$ case exhibits a larger width in the radial energy distribution at the lower values of $U_{rf} \cdot T_{rf}$ as in $\phi_{-,o} = 22.5^\circ$ case. The central peak narrows for larger values of $U_{rf} \cdot T_{rf}$ and at $U_{rf} \cdot T_{rf} = 2.90$ V·s the radial energy gained during the excitation begins to drop. The top three panels of the $\phi_{-,o} = 22.5^\circ$ case show a suppression of radial energy at $\Delta\nu \approx 2\nu_c$. The three bottom panels no longer exhibit

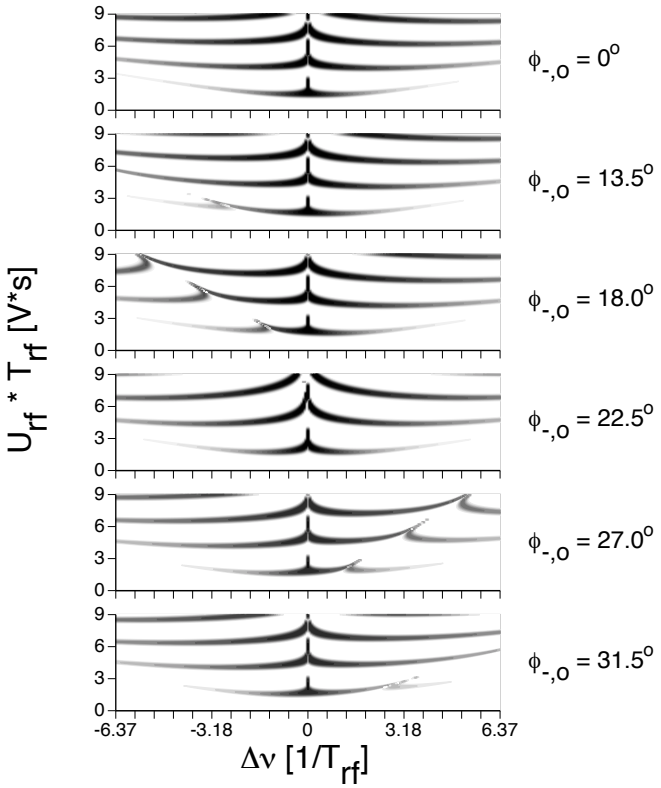

Figure 4.14. Simulation of ρ_+^2 for a single ion with $\rho_{-,o} = 1$ mm and $\rho_{+,o} = 0$ mm as a function of frequency detuning, $\Delta\nu = \nu_{rf}$ - $2\nu_c$, and U_{rf} for different values of $\phi_{-,o}$. The grey scale is proportional to ρ_+^2.

this behavior, but the central peak continues to narrow. In both cases $\Delta\nu_{FWHM}$ falls below $1/(100 \cdot T_{rf})$, which corresponds to a factor of ≈ 200 increase in resolving power over the quadrupolar excitation for the same excitation time! It remains to be seen how well the ions can be prepared to reproduce these results under realistic conditions.

4.3.3 Realistic multi-ion simulations

Simulations involving multiple ions representing a cloud are required to study the ion behavior in the case of an octupolar excitation under realistic conditions. First we will examine the radial energy gain as a function of U_{rf}, with $\nu_{rf} = 2\nu_c$. Gaussian

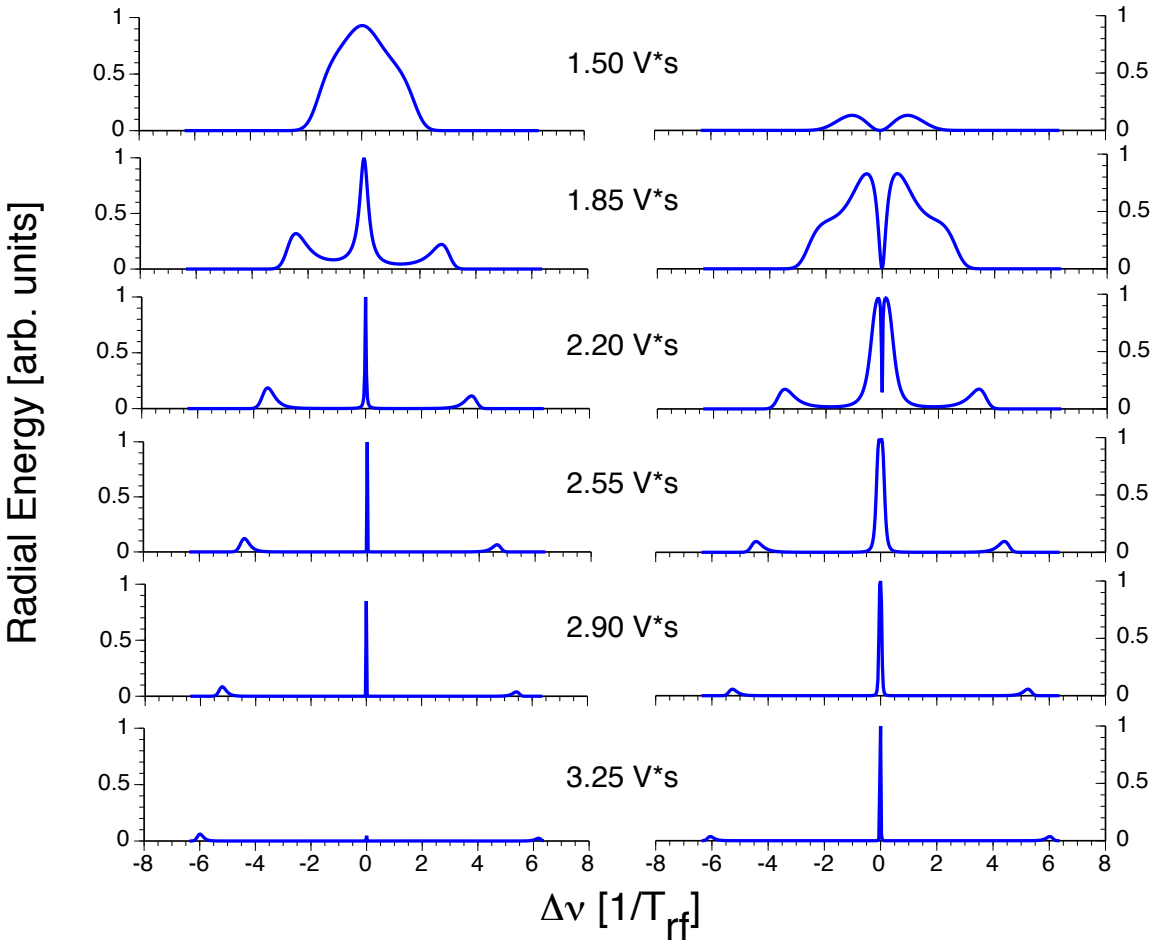

Figure 4.15. 2D cuts from the $\phi_{-,o}- = 0°$ and $\phi_{o,-}- = 22.5°$ 3D profiles in Fig. 4.14 for six different values of $U_{rf} \cdot T_{rf}$.

distributions were used in generating values for the initial ion cloud. Fig. 4.16 shows the results of three simulations for three different values of $\sigma_{\rho_{-,o}}$ with $\overline{\rho}_{-,o} = 0.55$ mm. $\rho_{+,o} = 0.050(5)$ mm was used, being a conservative estimate from simulated radial energy gain during injection into the Penning trap. This value also agrees with those obtained from fits to quadrupolar resonances obtained under similar conditions. Widths of the ϕ distributions seem to have a small effect on the multi-ion response curves, and $\phi_- = 0(5)°$ and $\phi_+ = 0(50)°$ were used. For the largest value of $\sigma_{\rho_{-,o}}$ shown in Fig. 4.16 the curve seems to mimic the behavior of a damped oscillator,

converging to some average asymptotical value of radial energy. This is the result of the beat frequency being dependent on ρ_o, as discussed in Sec. 4.3.2. The larger the spread in ρ_o, the larger the range of beat frequencies. The distribution of beat frequencies determines how quickly the average beat pattern is damped.

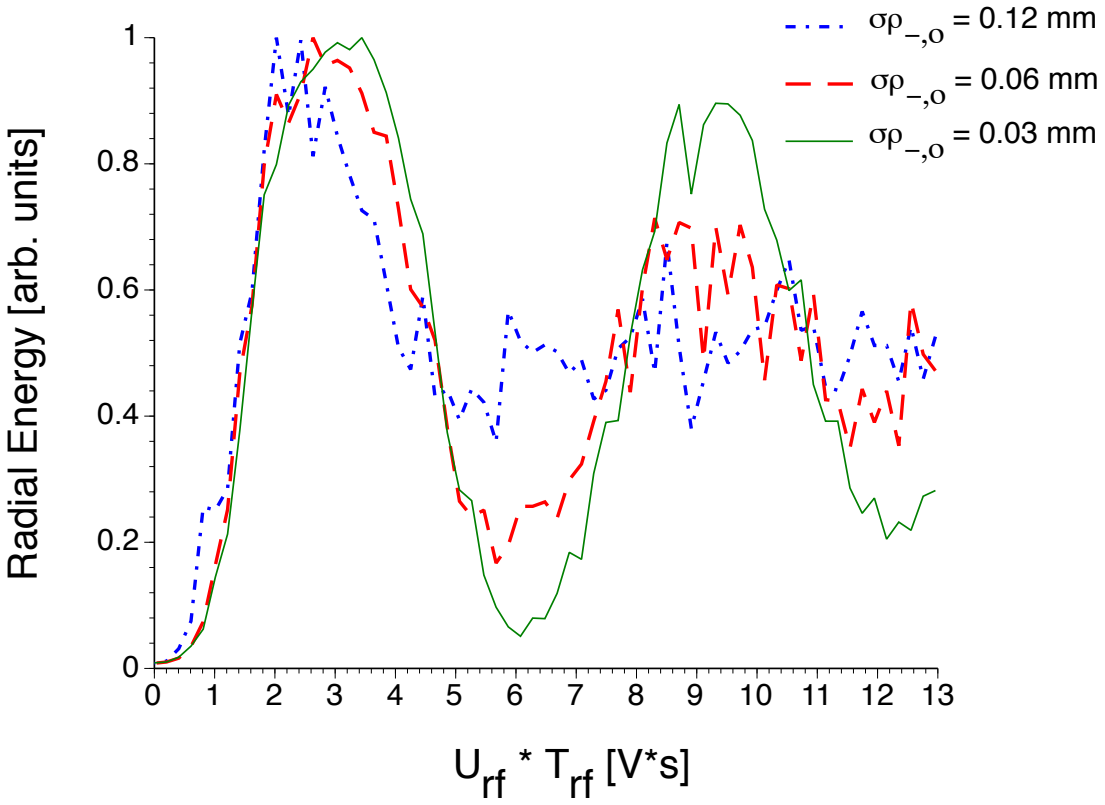

Figure 4.16. Simulated radial energy gain for three different values of $\sigma_{\rho_{-,o}}$ as a function of U_{rf} for $\nu_{rf} = 2\nu_c$ and $\overline{\rho}_- = 0.55$ mm.

Fig. 4.17 shows the results from two octupolar simulations of $^{23}Na^+$ with $T_{rf} =$ 50 ms. Both simulations were performed with identical phase and ρ_+ distributions as the simulations shown in Fig. 4.16. $\overline{\rho}_-$ was also held constant, but the widths of the distributions were changed. The simulation shown in the first column was performed with $\rho_{-,o} = 0.80(3)$ mm and in the second with $\rho_{-,o} = 0.80(13)$ mm. Instead of ρ_+^2 the calculated time of flight was plotted for easier comparison to experimental results

covered in the next chapter. The first row shows the dependence of the time of flight as a function of U_{rf} and $\Delta\nu$. The grey scale indicates smaller values of time of flight. The remaining rows are cuts through the data at different voltages.

Note the resemblance of the top left plot to the single-ion case shown in Fig. 4.14. For the larger $\sigma_{\rho_-,o}$, shown on the right, only one conversion is seen in the grey-scale plot before settling down to an average value. This is also reflected in Fig. 4.16. The 2D profiles also reveal that there is a greater separation in time of flight between the baseline and the minimum for the profiles on the left. In both cases as one proceeds from smaller to larger values of U_{rf} the resonance narrows. On the right-hand side the narrow peak begins to develop on top of a broader resonant structure, while on the left the time of flight baseline doesn't change. At $U_{rf} = 44.5$ V the resonance curve on the left has achieved a maximum change in time of flight and a minimal width of $\approx 0.14/T_{rf}$, corresponding to a gain of a factor of 13 in resolving power over the quadrupolar excitation.

4.3.4 Experimental procedure and results

Fig. 4.18 presents a schematic drawing of the electronic setup which was used to produce an azimuthal octupolar RF field in the LEBIT Penning trap. An arbitrary function generator (AFG) prodived a signal to a broadband RF amplifier with 65 dB gain. The signal from the amplifier was fed into a phase-splitting coil. The two output signals, $U_{rf,1}$ and $U_{rf,2}$, which are 180° out of phase, were then fed into the ring electrode segments. The amplitudes of the two phases agree to within $\approx$ 15-20 %. From now on, their average will be quoted as the excitation amplitude, U_{rf}.

In the experiments $^{23}Na^+$ ions were used. Ion bunches from the cooler/buncher were injected off-axis, via the Lorentz steerer, described in detail in Chapter 5, and trapped in the LEBIT high-precision Penning trap.

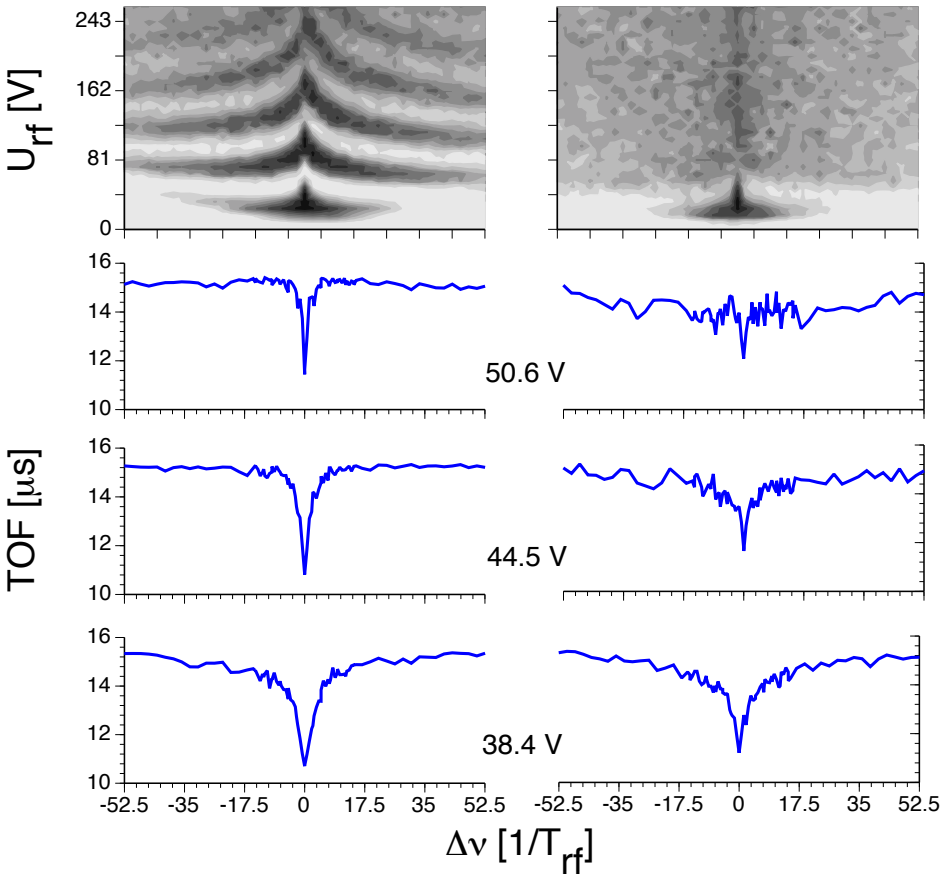

Figure 4.17. (Left): multi-ion simulation of TOF as a function of U_{rf} and $\Delta\nu$ with three cuts at different RF voltages. (Right): same as the left only the width of the $\rho_{-,o}$ distribution has been increased by a factor of 4.

Experimental octupolar studies in resonance

$^{23}Na^{+}$ ions were excited with an octupolar excitation with $\nu_{rf} = 2\nu_c$ for $T_{rf} = 50$ ms and their time of flight was measured as a function of U_{rf}. The result is shown in Fig. 4.19 together with a simulated curve. The simulated curve corresponds to the $\sigma_{\rho_{-,o}} = 0.13$ mm case from Fig. 4.16. In order to get a good agreement between experimental data and the simulation results it was necessary to divide RF voltage values measured at the output of the circuit by a factor of 0.7. Such a factor makes sense as it accounts for RF attenuation and partial shielding due to the geometry of the trap. Using experimental data like that shown in Fig. 4.19 and comparing

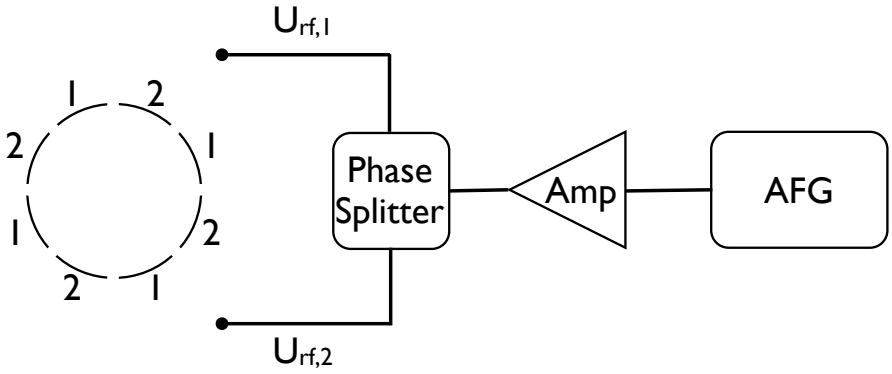

Figure 4.18. Schematic drawing of experimental setup used to produce a azimuthal octupolar RF field in the LEBIT Penning trap.

to the corresponding simulation results allows the values of $\overline{\rho}_{-,o}$ and $\sigma_{\rho_{-,o}}$ to be determined. The minimum time-of-flight value achieved is a function, primarily, of $\overline{\rho}_{-,o}$, and the damping of the curve is determined by the ratio of $\sigma_{\rho_{-,o}}$ and $\overline{\rho}_{-,o}$.

In the case of quadrupolar excitation, the beat frequency of ρ_+^2(t) is proportional to the product $\mathrm{U}_{rf}{\cdot}\mathrm{T}_{rf}$ (see Eq. 4.4). We will experimentally explore if this holds true for the octupolar excitation, as well. Fig. 4.20 shows the time of flight of ions as a function of U_{rf} for five different excitation times. As expected, the minimum time of flight is reached at a lower value of U_{rf} for longer excitation times. The value of U_{rf} where the TOF curve reaches its minimum will be labeled U_o. Fig. 4.21 displays the product $\mathrm{U}_o{\cdot}\mathrm{T}_{rf}$ for the fives cases shown in Fig. 4.20, along with simulated data using our best-fit parameters determined by the comparison shown in Fig. 4.19. Both the experimental and simulated data agree and are constant within 5%. This value will not be constant for all circumstances, and depends on initial conditions.

By adjusting the Lorentz steerer we can control $\overline{\rho}_{-,o}$. The displacement of the ions as a function of the applied voltage is linear. Fig. 4.22 shows six different octupolar scans of TOF as function of U_{rf} in the case of $\nu_{rf} = 2\nu_c$ for six different voltages, V_L, applied to the Lorentz steerer. The first minimum in the curves represent the

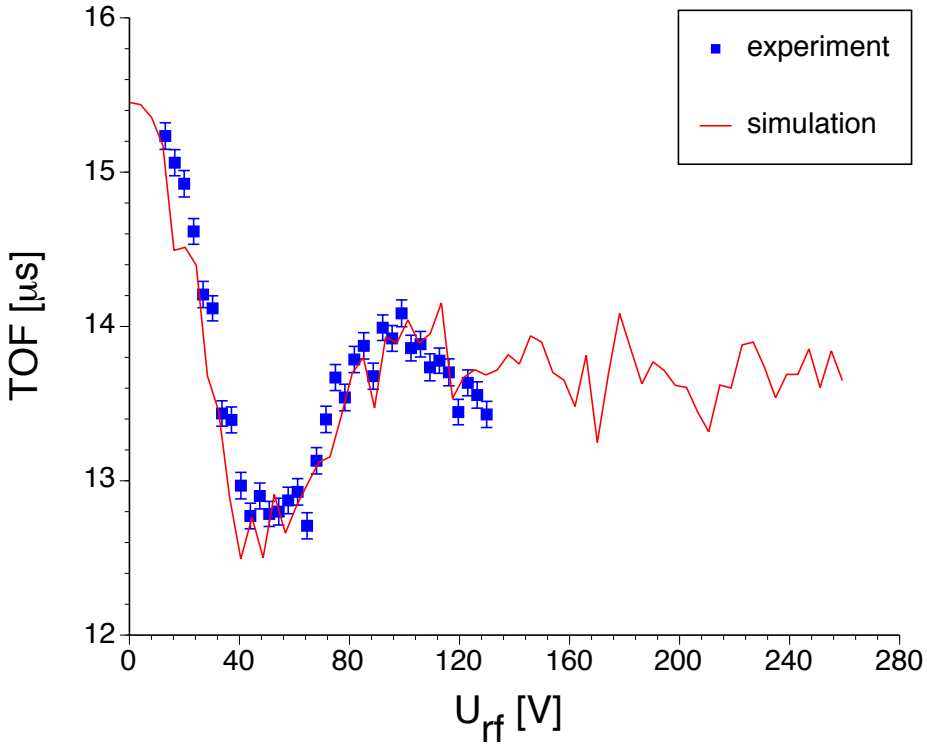

Figure 4.19. Time of flight as a function of U_{rf} for a octupolar excitation of $^{23}Na^{+}$ with $T_{rf} = 50$ ms at $\nu_{rf} = 2\nu_c$. The solid line shows the results of a simulation.

necessary U_{rf} to, on average, bring the ions to a state of maximum radial energy.

Fig. 4.23 contains the beat frequencies observed in Fig. 4.22 as a function of $\rho_{-,o}$. Two of the curves are simulation results and one is experimental data. The experimental observation does not seem to confirm the nonlinear response illustrated in Fig. 4.8. However, the $\sigma_{\rho_{-,o}} = 0.13$ mm curve represents our best-fit simulation scenario, and matches the data quite well. The third curve reduces the best-fit value of $\sigma_{\rho_{-,o}}$ by a factor of four to 0.0325 mm. Now the curve begins to recover the nonlinear shape shown in the single ion simulations. Again the variation of individual beating frequencies of ions in the cloud play a dominant role in determining the overall response of the system.

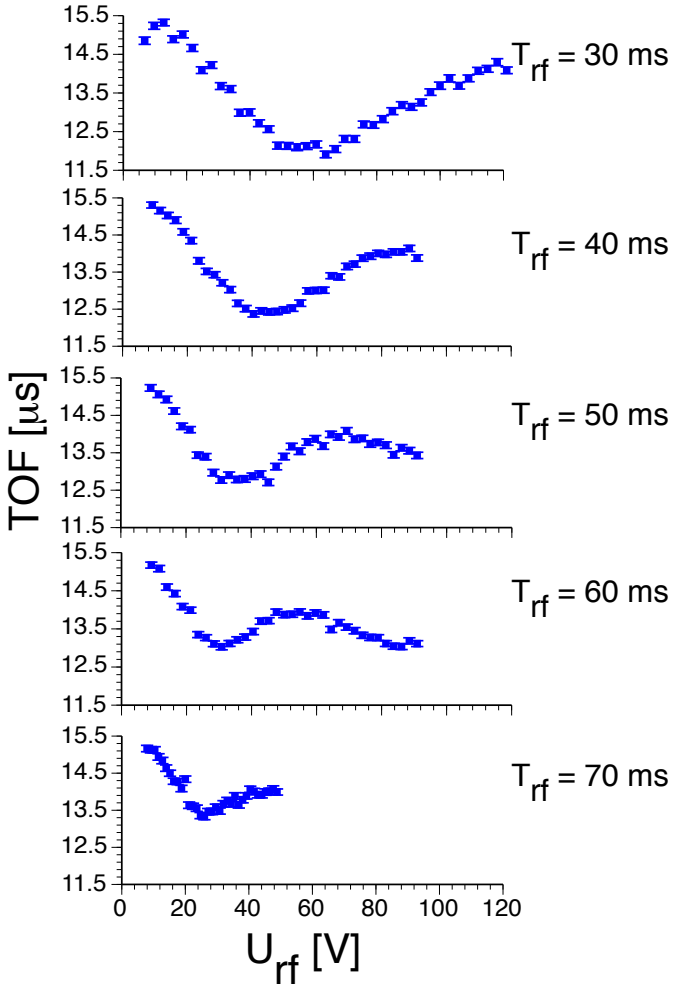

Figure 4.20. Octupolar TOF curves of $^{23}Na^{+}$ as a function of U_{rf} with $\nu_{rf} = 2\nu_c$ for several excitation times.

Experimental octupolar resonances

Fig. 4.24 displays several octupolar resonances of $^{23}Na^{+}$ produced with $T_{rf} = 50$ ms for various values of U_{rf}. Included in the figures are simulated resonances which were produced using the same initial conditions as the simulation in the right column of Fig. 4.17. For $U_{rf} \leq 40$ V the width of the resonances are between $1.3/T_{rf}$ and $0.9/T_{rf}$. Proceeding towards larger amplitudes reduces this width. At $U_{rf} = 72.9$ V a narrow resonant peak with a width of $\approx 0.2/T_{rf}$ forms atop a broader resonant structure.

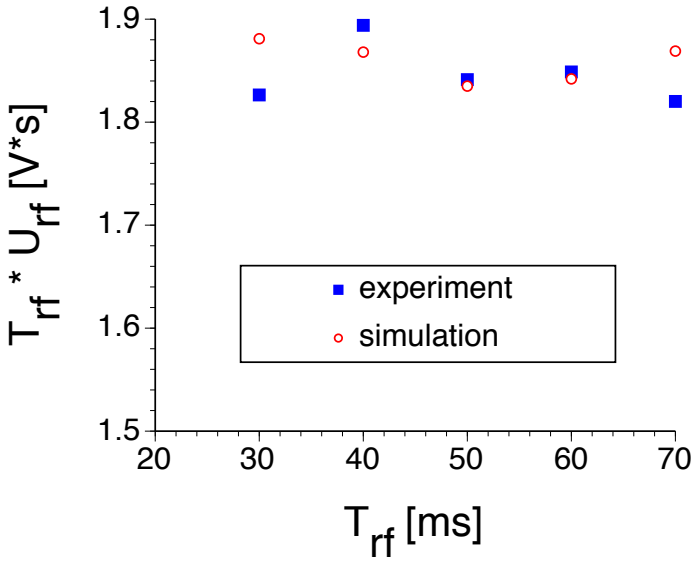

Figure 4.21. Product of U_o and T_{rf}, where T_{rf} is the duration of the octupolar excitation and U_o is the amplitude of applied octupolar RF field at which the TOF curve reaches its minimum.

Mass measurements with octupolar excitation

To verify that octupolar resonances can be used for precision mass measurements, a mass measurement of $^{41}K^+$, using $^{39}K^+$ as a reference, was performed. An excitation time of T_{rf} = 200 ms was used in each individual measurement. U_{rf} was chosen such that the resonances were Gaussian. Fig. 4.25 shows the results of this mass measurement. As there is no theoretical line shape all resonances were fit with a Gaussian profile. The difference of the mean mass value extracted from the octupolar measurements from the accepted literature values (Atomic Mass Evaluation [2]) is shown. The dashed lines represent the uncertainty in the mean of the experimental results. The solid lines represent the uncertainty in the AME values. As can be seen, there is excellent agreement within the uncertainty.

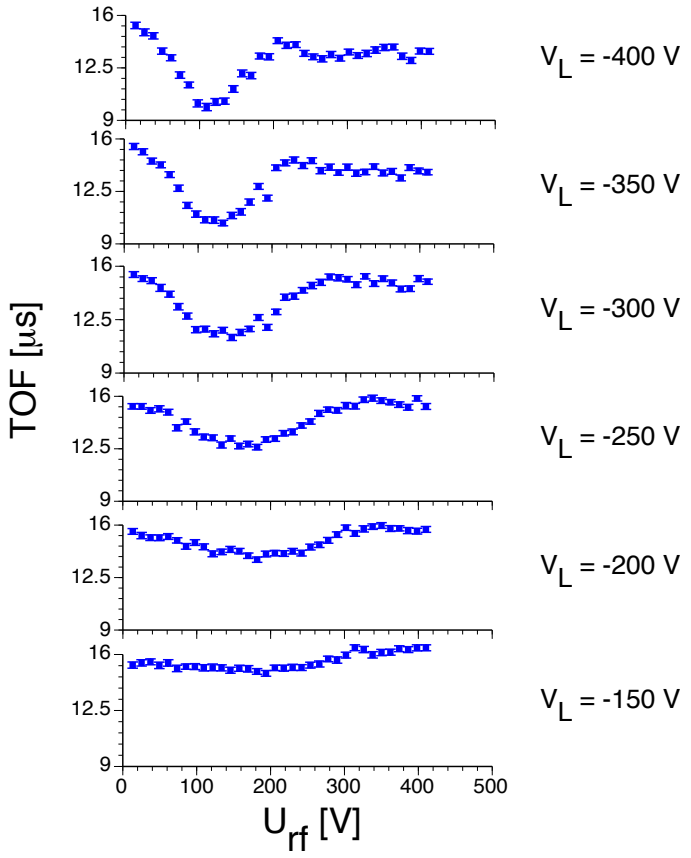

Figure 4.22. Time of flight as a function of U_{rf} with $\Delta\nu = 0$ using $^{23}Na^{+}$ with $T_{rf} = 50$ ms octupolar excitation for six different Lorentz steerer voltages, V_L. The greater the magnitude of applied voltage, the larger the initial average displacement of the ions from the center of the trap.

4.4 Summary and conclusions

Although an analytical solution to the octupolar excitation has yet to be found, numerical simulations combined with experimental results have offered significant insight into this complicated problem. The most important observations can be summarized as:

- *The beat frequency of an ion subjected to an octupolar RF excitation applied at $\nu_{RF} = 2\nu_{+} + 2\nu_{-} = 2\nu_c$ is dependent upon the initial conditions of the ion motion. This is in contrast to the quadrupolar excitation at ν_c where such a*

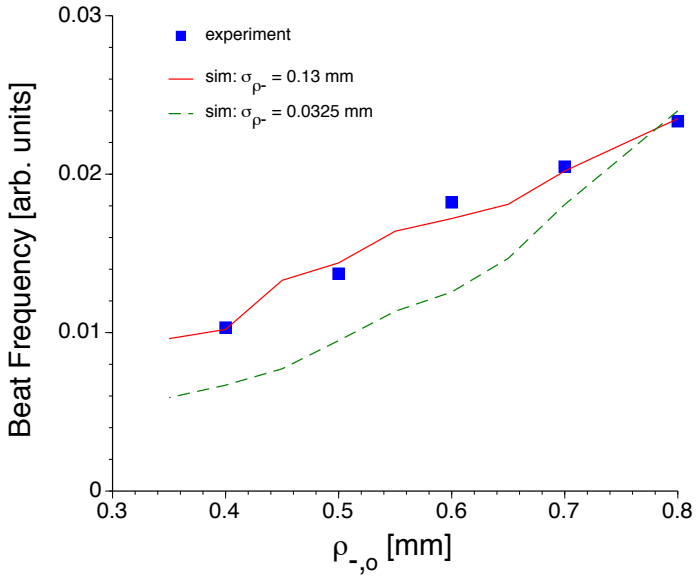

Figure 4.23. Beat frequency as a function of $\overline{\rho}_{-,o}$. The experimental curve is extracted from data shown in Fig. 4.22. The $\sigma_{\rho_{-,o}} = 0.13$ mm curve is a simulation based on the parameters extracted from the simulation shown in Fig. 4.19. The second simulated curve was generated using identical parameters, except $\sigma_{\rho_{-,o}} = 0.0325$ mm.

dependence does not exist as long as $\rho_{+,o} = 0$.

- *The octupolar resonance profiles have a radically different shape than their quadrupolar counterparts.*

- *For certain initial conditions it is possible to reduce the width of octupolar resonances by a factor of 10 or more beyond what is achievable with a comparable quadrupolar resonance performed with the same excitation time.*

We have verified a factor of 9 gain in resolving power over the standard quadrupolar excitation scheme. According to the simulation results presented in Fig. 4.17, a factor of four reduction in $\rho_{-,o}$ would yield a factor of 13 gain without the broad resonant structure observed in Fig. 4.24. We have also shown that the initial conditions of the ion cloud determines the ultimate resolving power that can be achieved. Simulations show even higher resolving powers are possible, provided that the ions can be prepared

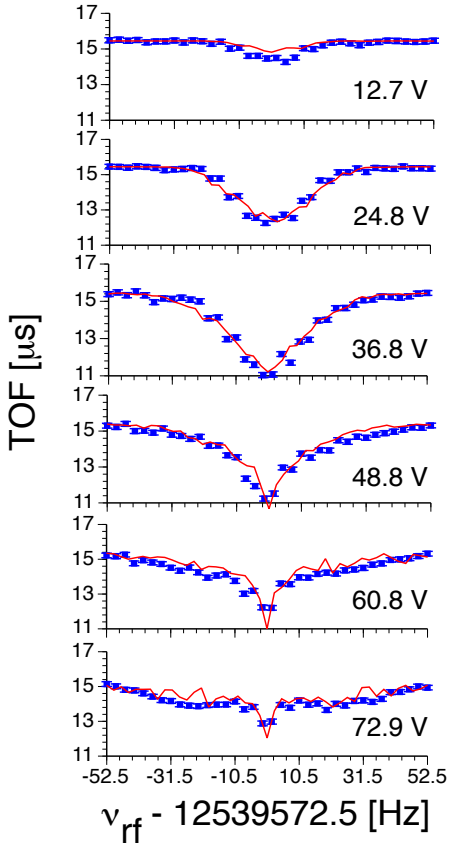

Figure 4.24. Several octupolar resonance profiles of $^{23}Na^{+}$ with T_{rf} = 50 ms for various values of U_{rf} (data points) compared with simulated results (solid lines).

appropriately. Although more work is required to assess the absolute accuracy of mass measurements performed with octupolar excitations, a promising first step has been taken towards the implementation of octupolar resonances in high-precision mass measurements. Motivated by the phase dependence exhibited by the octupolar excitation, we have also revisited the quadrupolar excitation and confirmed a phase dependence of resonance line shapes.

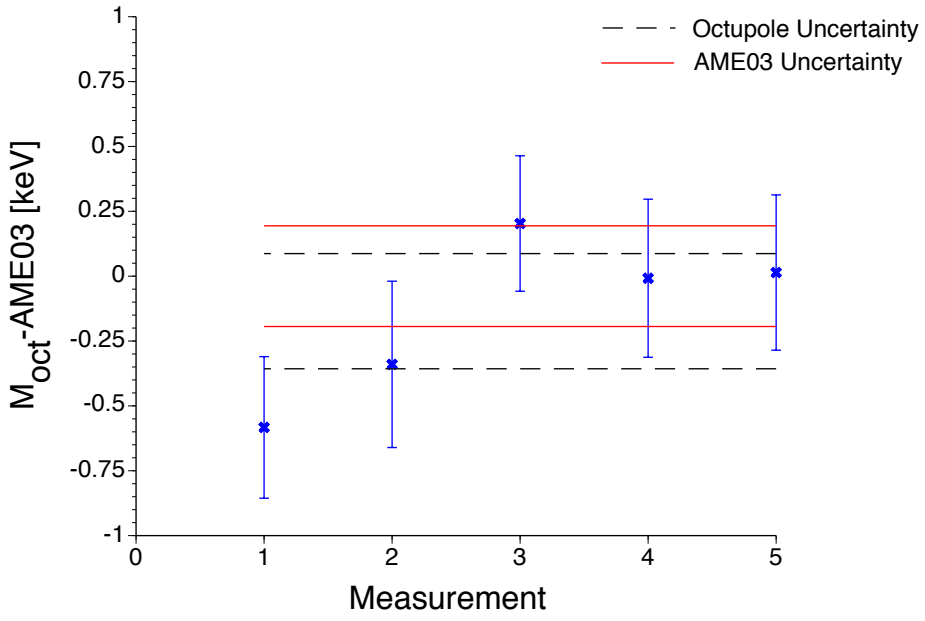

Figure 4.25. Mass comparison of $^{39,41}K^{+}$ using octupolar excitation. $^{39}K^{+}$ was used as the reference and all measurements were performed with 200 ms excitation times.

CHAPTER 5

Development and detailed study of the Lorentz steerer

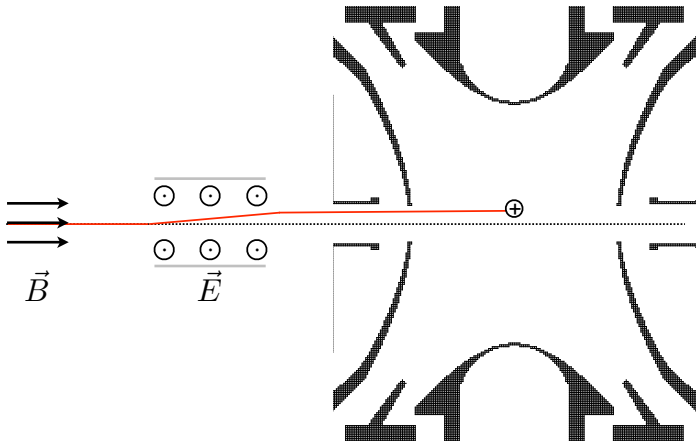

Figure 5.1. Cartoon illustrating a positively-charged ion passing through a region of perpendicular electric and magnetic fields, resulting in an off-axis capture in a Penning trap.

As mentioned in Sec. 3.1.3, before the application of a quadrupolar (or octupolar) field it is necessary for a trapped ion to be executing some initial motion. Normally this is achieved by first applying a dipole RF field at frequency ν_+ to drive the ion's magnetron motion. After the ion has been driven out to some radius the quadrupolar excitation will drive a beating between the magnetron and cyclotron motions. This

dipolar excitation requires some finite amount of time, on the order of 10 ms, to perform. Additionally, the RF excitation must be phase locked to the time of ion capture to ensure that for each individual measurement that the value of ρ_-, previous to the application of the quadrupolar RF field, is the same.

Since every millisecond is precious when making mass measurements on short-lived species, a method that could prepare the ions in-flight would be very desirable. The Lorentz steerer accomplishes this by creating an electric dipole field before the Penning trap, but well within the strong magnetic field region. The ions experience a net force in the $\mathbf{E}\times\mathbf{B}$ direction which results in an off-axis capture in the Penning trap, resulting in an initial magnetron motion and eliminating the need for an initial dipolar excitation. This process is illustrated schematically in Fig. 5.1

5.1 Charged particle motion in a region of perpendicular electric and magnetic fields

To begin we will consider the motion of a particle as it travels through a region of perpendicular electric and magnetic fields. Let $\vec{B} = \mathrm{B}\hat{z}$ and $\vec{E} = \mathrm{E}\hat{y}$. The equations of motion in the radial plane which must be solved are

$$\ddot{\vec{r}} = \frac{q}{m}(E\hat{y} + \dot{\vec{r}} \times B\hat{z}). \tag{5.1}$$

Consider a particle initially at the origin traveling in the $\vec{z}$ direction with no initial radial energy. The velocity in the radial plane and the radial displacement is then

$$\dot{r}(t) = \frac{\sqrt{2}E}{B}\sqrt{1-\cos(\omega_c t)} \tag{5.2}$$

$$r(t) = \frac{E}{B^2 q}\sqrt{2m^2[1-\cos(\omega_c t)] + [Bqt]^2 + 2mBqt\sin(\omega_c t)}, \tag{5.3}$$

where E is the strength of the electric field, q is the ionic charge, m is the mass, B is the strength of the magnetic field and ω_c = (q/m)B. For large values of t,

$$\lim_{t\to\infty} r(t) = \frac{E}{B} \cdot t = \bar{v}_{\text{drift}} \cdot t, \tag{5.4}$$

where $\bar{v}_{\text{drift}}$ is the average drift velocity of the ions. The displacement after traveling a distance L is proportional to $t = L/v_z \propto \sqrt{m}$.

For example, Fig. 5.2 shows the radial displacement as a function of time for an A = 40, singly-charged particle as it travels through a region of perpendicular, uniform electric, E = 28.6 V/m, and magnetic, B = 9.4 T, fields. This displacement is accompanied by a pickup of cyclotron motion which leads to the observed non-linearity. Fig. 5.3 shows the square of the radial velocity, which is proportional to

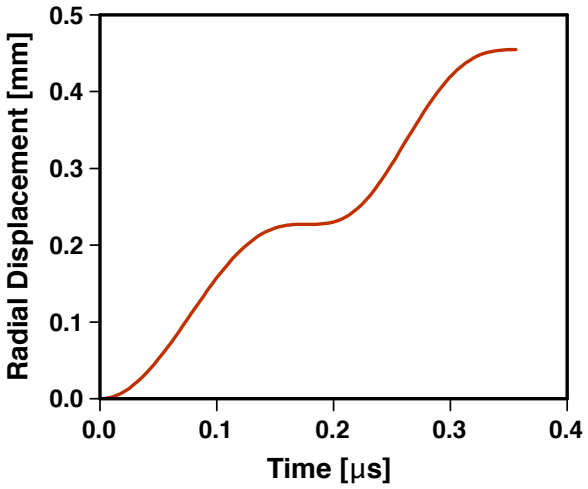

Figure 5.2. Radial displacement as a function of time for a charged particle passing through a region of uniform, perpendicular electric and magnetic fields.

the radial energy, of a particle as a function of ω_ct. From Eq. 5.2 it can be seen that the radial velocity as a function of time scales as 1-cos(ω_ct). If we consider the particle to enter and exit the electric field suddenly, then upon exit it would have a radial velocity between 0 and $\sqrt{2}E/B$, depending upon the time of exit. Having left the electric-field region the ion performs a cyclotron motion with a radius that

depends on the time of exit. For the example parameters used here the maximum radial velocity is $V_r = 4300$ m/s, which corresponds to a radial energy $K_r = 5$ eV and a radius of the cyclotron motion of $\rho_{+,o} = 0.17$ mm.

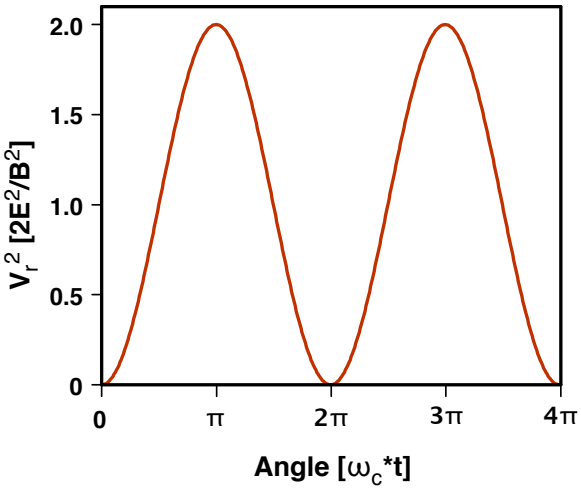

Figure 5.3. Square of the radial velocity as a function of ω_ct of a charged particle after it has travelled through a region of uniform, perpendicular electric and magnetic fields.

5.2 Lorentz steerer design

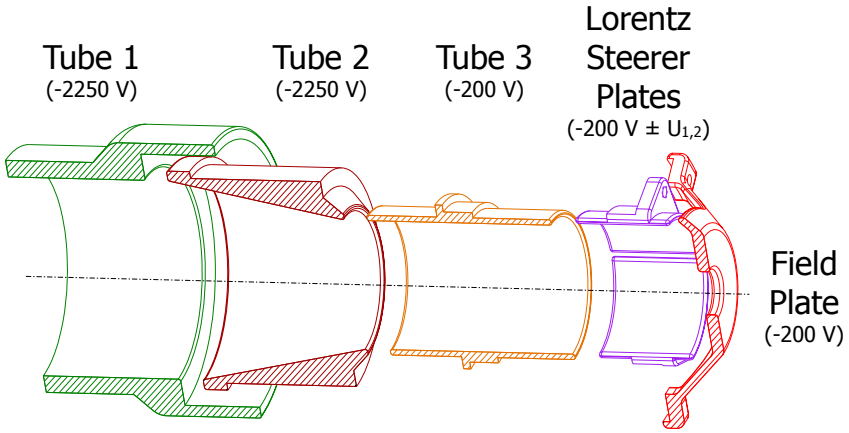

Figure 5.4. Isometric section of the Lorentz steerer and nearby optics elements. The dashed line is the axis. Typical operating voltages are listed.

The design of the Lorentz steerer is remarkably simple, being four segments of a cylinder quartered in the radial plane. Fig. 5.4 shows a design drawing of the injection optics of the LEBIT Penning trap mass spectrometer which contains the Lorentz steerer. The Lorentz steerer is located just upstream of a field termination plate, and after a series of drift tubes. The steerer electrode system is 16.5 mm in length and 28 mm in diameter with 3 mm gaps between the four segments. Typical operating voltages are listed. These voltages were also used in SIMION simulations discussed later.

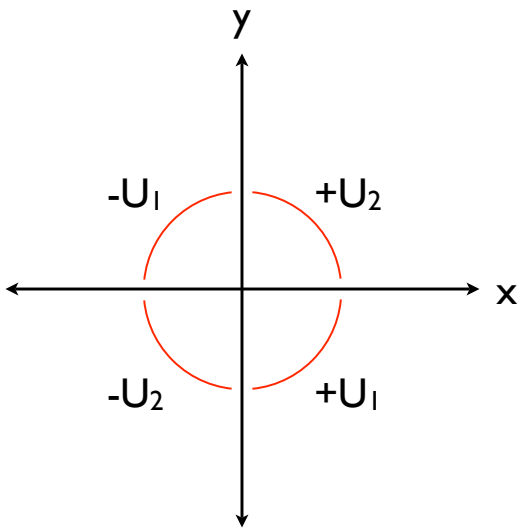

Figure 5.5. Schematic layout of the Lorentz steerer's electrode configuration. Each pair of diametrically opposing electrodes can be used to create an electric dipole field. Both pairs can be used simultaneously to orient the dipole field in space.

Fig. 5.5 shows a simple sketch of the electrode layout of the Lorentz steerer. Each pair of diametrically opposing electrodes can be used to generate an electric field with a dominant dipolar component. Changing the values of U_1 and U_2 such that $\sqrt{U_1^2 + U_2^2}$ remains constant results in a constant magnitude of the dipole field, but changes its orientation in space. This imparts a constant radial displacement with an

adjustable angle to ions passing through the steerer.

5.3 Lorentz steerer beam calculations

5.3.1 Ion cloud deflection simulations

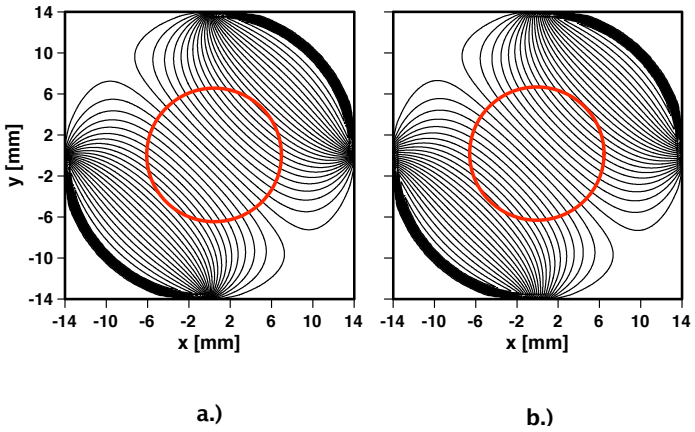

Figure 5.6. Contour plots of the potential at the mid-plane of the Lorentz steerer given by a.) the analytical solution and b.) the SIMION calculation for $U_1 = 0$ V and $U_2 = 1$ V (see Fig. 5.5). Within a circle of radius of 6 mm the relative difference of the potentials obtained by both methods is less than $4{\times}10^{-3}$.

The ion deflection in the Lorentz steerer has been calculated both analytically and numerically. While the magnetic field is assumed to be homogeneous, the electric field inside the steerer is required. One method is to use SIMION [50] to numerically solve the Laplace equation in a geometry based on the design drawing shown in Fig. 5.4 and to trace the ions through the electric and magnetic fields. Another method to obtain the electric field is to analytically solve the electric potential for an infinite quartered cylinder. This potential is given by

$$\begin{aligned} U(r,\phi) = \; & \frac{U_1}{\pi}\left[\arctan\left(\frac{2Rr\sin(\phi)}{R^2-r^2}\right) - \arctan\left(\frac{2Rr\cos(\phi)}{R^2-r^2}\right)\right] + \\ & \frac{U_2}{\pi}\left[\arctan\left(\frac{2Rr\sin(\phi)}{R^2-r^2}\right) + \arctan\left(\frac{2Rr\cos(\phi)}{R^2-r^2}\right)\right], \end{aligned} \tag{5.5}$$

where R is the radius of the cylinder and U_1 and U_2 are the applied voltages. In order to account for the finite length of the Lorentz steerer the analytic potential given by this equation can be multiplied by a function f(z). From a comparison with the potential obtained with SIMION a function f(z) = $e^{(-z/\alpha)^4}$ with $\alpha = 1{\times}10^{-2}$ m was found to fit the potential along the axis well. Fig 5.6 plots the mid-plane potentials obtained from the SIMION calculation and the analytical solution for U_2 = 1 V and U_1 = 0 V. Within a 6 mm radius from the center of the steerer the potentials agree within $<4{\times}10^{-3}$.

A series of simulations was performed, using both the analytical and the SIMION potentials, to study the properties of the actual Lorentz steerer. In the case of the SIMION simulations the geometry and potentials as shown in Fig. 5.4 were used. The initial ion distribution contained 500 ions and was centered on the axis of the Lorentz steerer. The width of the initial distribution in the radial direction was 0.1 mm. The ions started their flight in Tube 1, shown in Fig. 5.4, with an axial energy of 2 keV and no radial energy. After passing through the Lorentz steerer their radial positions were recorded at the location of the field plate.

Fig. 5.7 shows the mean radial displacement as a function of the potential applied to U_2 obtained from the SIMION simulations. As expected, the average radial displacement is proportional to U_2. The slopes of these lines represent a steering strength which depends on the mass and axial energy of the ion passing through the Lorentz steerer. Fig. 5.8 shows steering strength values obtained from the SIMION simulation (like those shown in Fig. 5.7). The solid line is the result of a calculation using the analytical solution for the potential of the quartered cylinder. There is good agreement between the SIMION simulations and the calculations.

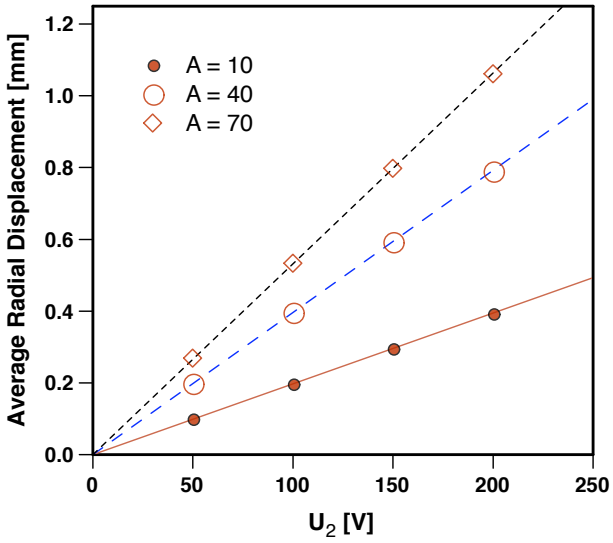

Figure 5.7. Results of SIMION simulation showing mean radial displacement (data points) as a function of Lorentz steerer voltage (U_2) for three different masses. Lines are the results of a linear regression analysis.

5.3.2 How to achieve minimum cyclotron motion?

When injecting ions into a Penning trap it is important to introduce as little radial energy in the process as possible, as non-zero values of the initial cyclotron radius, $\rho_{+,o}$, can introduce asymmetries in the resonance line shape [51] and reduce the magnitude of the resonance signal. Fig. 5.9 shows the radial displacement as a function of time of an A = 70, singly-charged ion for two different of axial energies. The steering voltage was adjusted to result in the same final radial displacement. The curves were calculated using the analytical potential. The solid line is the result for an ion with K = 200 eV of axial energy and a steerer voltage U_2 = 400 V. The dashed line is the result for an ion with K = 50 eV of axial energy and a steerer voltage U_2 = 200 V. The K = 200 eV ion exits the electric field region after $\approx$ 1.25 μs. The oscillations are due to the induced cyclotron motion (see Sec. 5.1), in this case leading to an amplitude $\rho_{+,o} \approx$ 0.1 mm. The slow ion exits the electric field region after $\approx$ 2.5 μs and achieves the same mean radial displacement as the fast ion, but with a cyclotron

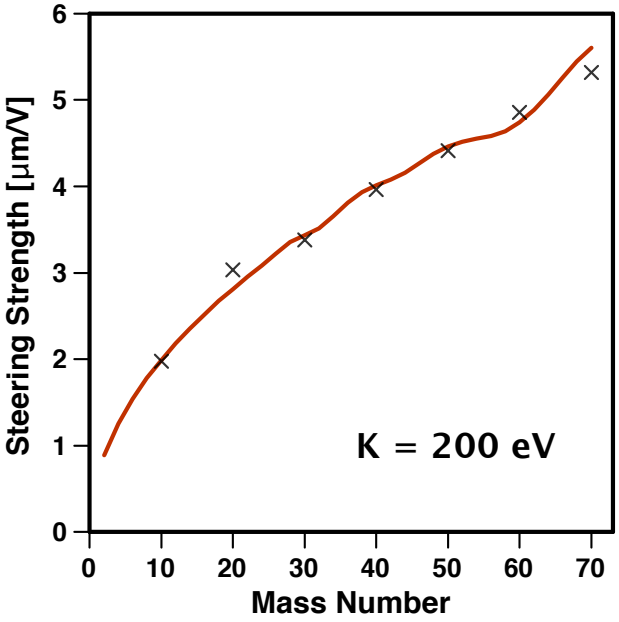

Figure 5.8. Steering strength as a function of mass number of a singly-charged ion with K = 200 eV axial energy determined from SIMION simulations. The solid line is obtained using the analytical solution for the potential.

amplitude of $\rho_{+,o} \approx 2$ μm. Qualitatively this can be understood upon closer inspection of Eq. 5.2. Slower ions require more time to pass through the Lorentz steerer and therefore require a smaller electric field strength E to drive them to the same final radial displacement as a faster ion. For the system employed in the LEBIT Penning trap mass spectrometer an axial energy of less than 75 eV reduces the radial energy gain to sub-eV levels for the maximum applied steering voltages of 400 V.

5.4 Lorentz steerer measurements

$^{39}K^{+}$ ions were created with a plasma ion source and delivered as short pulses using the LEBIT beam cooler and buncher [37]. After passing through the Lorentz steerer the ions were captured in the Penning trap. If the ions enter the trap off axis then upon being trapped they perform an initial magnetron motion. Application of a

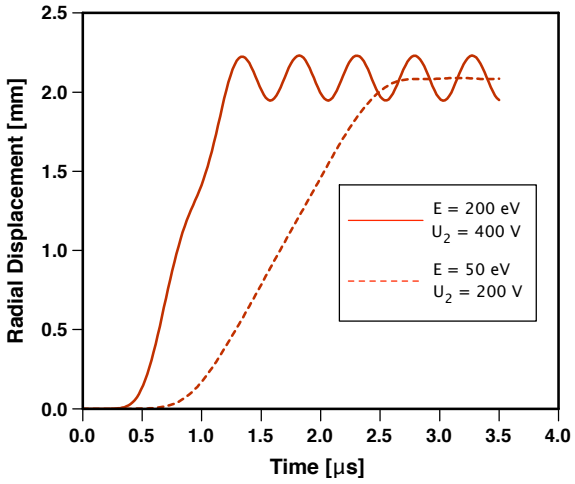

Figure 5.9. Calculated radial displacement as a function of time for an A = 70, singly-charged ion as it travels through, and out of, the Lorentz steerer. The solid line is for a beam with K = 200 eV axial energy. The dashed line is for a beam with K = 50 eV axial energy. The steering voltages have been adjusted to result in the same final radial displacement.

π-pulse with frequency $\nu_{rf} \approx \nu_c$ can be used to completely convert the magnetron motion into cyclotron motions as discussed above. The accompanied increase in radial energy which can be detected via measurement of the time-of-flight of the ions [44] from the trap to a detector located outside of the magnetic field. By taking the radial energy gain and the known electric and magnetic fields traversed by the ion on its path to the detector, the value for the initial magnetron amplitude can be determined.

Fig. 5.10 (top) shows the time of flight of ejected $^{39}K^{+}$ ions as a function of voltage applied to the Lorentz steerer electrodes after capture in the trap and subsequent quadrupolar excitation for a time T_{rf} = 50 ms. U_2 was held at a constant 84 V for the following reasons. Due to imperfections in the injection of the ions into the magnetic field of the Penning trap spectrometer steering voltages of $U_1 = U_2 = 0$ do not necessarily correspond to injection on the trap axis, and an initial steering by the Lorentz steerer may be required. The values $U_{1,2}$ = (-24 V, 84 V) correspond to

the maximum time of flight (and minimum initial magnetron amplitude). For ease of discussion we introduce offset-corrected steering voltages such that $U_{1,2}$' = (0 V, 0 V) corresponds to the maximum time of flight observed for $^{39}K^{+}$ ions.

Fig. 5.10 (bottom) shows the values of the initial magnetron amplitude calculated from the time-of-flight data in Fig. 5.10 (top) as a function of U_1'. The solid lines illustrate that the size of the magnetron radius $\rho_{-,o}$ of the captured ions is proportional to U_1', as expected from the simulation results shown in Fig. 5.7.

Fig. 5.11 shows the results for the initial magnetron radius $\rho_{-,o}$ as a function of the true voltage U_1 obtained from measurements with three different ion species. The solid lines are linear fits to the data. The numbers in parentheses are the slopes of the lines which correspond to steering strength values (in μm/V). According to Eq. 5.4, the displacement respectively steering strength is proportional to $\sqrt{m}$ for ions with the same axial velocity. This is reflected in the experimental data and the measured steering strength values for ^{23}Na and ^{39}K also agree with the calculated values shown in Fig. 5.8.

The Lorentz steerer should allow for precision control not only of the amplitude of the magnetron motion, but of the initial phase, as well. In order to investigate how well this control works, an experiment was performed according to the following procedure. $^{39}K^{+}$ ions were placed off axis into the trap using the Lorentz steerer, resulting in an initial magnetron radius. Next, a dipolar RF field, at frequency ν_{-} which is phase-locked to the time of ion capture, was applied. Depending on the phase of the RF field the excitation of the magnetron motion will result in a larger or smaller final magnetron radius. Using a π-pulse with $\nu_{rf} = \nu_c$ and the time-of-flight measurement allows the amplitude of the magnetron motion after the dipolar excitation to be determined. Fig. 5.12 presents the results of such a measurement. The magnetron amplitude ρ_{-} of $^{39}K^{+}$ ions is plotted as a function of the initial phase of the dipolar RF field for four different Lorentz steerer settings. Each setting

corresponds to a magnetron phase change of 90° from the previous setting and should provide the same steering strength. The data were fit with a sinusoidal function (solid line), $\rho_{-}(\phi) = \rho_{-,o} + \Delta\rho_{-}\cdot\sin(\phi_{rf} - \phi_{-,o})$, where $\rho_{-,o}$ is the initial magnetron amplitude introduced by the Lorentz steered, $\Delta\rho_{-}$ is the maximum amplitude change due to dipolar excitation, ϕ_{rf} is the initial phase of the RF, and $\phi_{-,o}$ is the initial magnetron phase. The results, given in Table 5.1, show that the initial magnetron amplitudes, $\rho_{-,o}$, due to the effect of the Lorentz steerer alone, agree to within a few percent. The phase change of 90° from one case to the next is confirmed to within ±2°. Both of these results together confirm that the ions were moved on a circle in the radial plane of the Penning trap and demonstrate the precision control of the initial ion placement in the trap available with the Lorentz steerer.

Table 5.1. Summary of the results of a fit of a sinusoidal function to the data presented in Fig. 5.12. $U_{1,2}$' are the offset-corrected voltages applied to the Lorentz steerer, $\rho_{-,o}$ is the initial magnetron amplitude given by the fit, $\phi_{-,o}$ is the initial magnetron phase given by the fit, and $\Delta\phi = |\phi^{i}_{-,o} - \phi^{i+1}_{-,o}|$ is the phase advance from one setting to the other.

	U_1' [V]	U_2' [V]	$\rho_{-,o}$ [mm]	$\phi_{-,o}$ [deg]	$\Delta\phi$ [deg]
1	-100	0	0.94(2)	102(1)	87(2.2)
2	0	+100	0.96(2)	189(2)	93(2.2)
3	+100	0	0.93(2)	282(1)	91(2.2)
4	0	-100	0.96(1)	13(2)	89(2.2)

A new technique for the precise manipulation of ion injection into a Penning trap has been developed and tested. It is used routinely in LEBIT's Penning trap mass spectrometer. Compared to the alternative method of magnetron preparation via dipolar excitation, it is less complicated and requires no additional preparation time. The Lorentz steerer offers complete control over the injection process and 360° placement of an ion cloud in the radial plane of a Penning trap. We expect that such

a Lorentz steerer is a likely successor to dipolar excitation for magnetron preparation in future Penning trap systems. It is already planned to be used in the TITAN [52] Penning trap mass spectrometer, presently under construction.

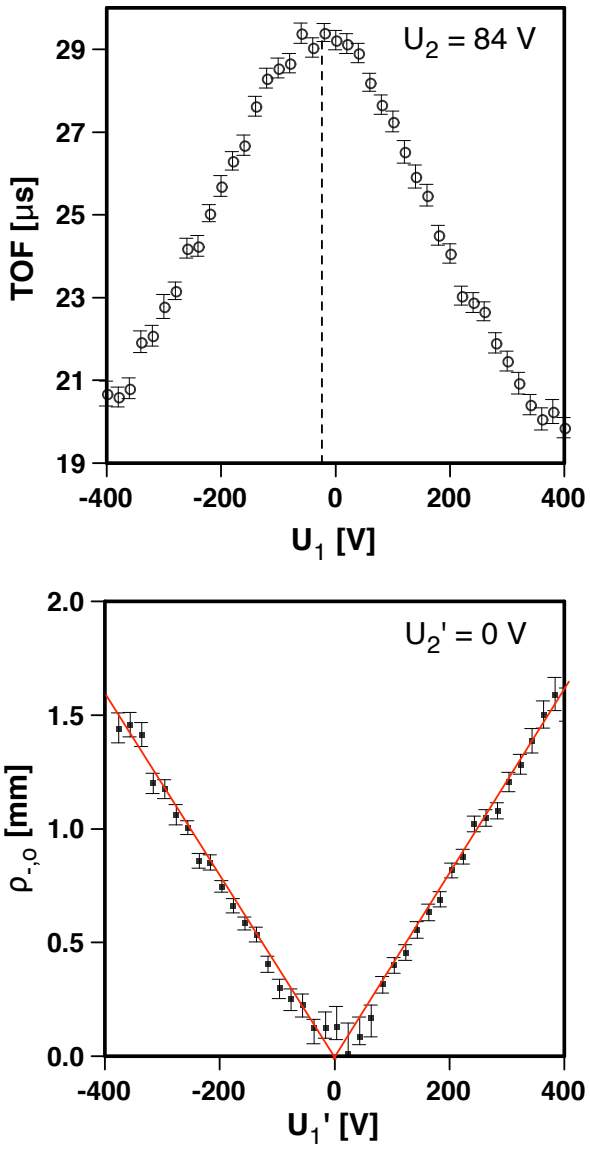

Figure 5.10. Top: Time of flight of $^{39}K^{+}$ ions ejected from the trap after being subjected to a quadrupolar RF field with a frequency ν_c as a function of U_1 with U_2 = 84 V.
Bottom: Initial magnetron amplitude, $\rho_{-,o}$, as calculated from the time-of-flight data shown above. $U_{1,2}$' are offset-corrected values of $U_{1,2}$ such that for $U_{1,2}$' = (0 V, 0 V) the value of $\rho_{-,o}$ is minimized. Lines are to guide the eye and to illustrate the linearity of steering with applied voltage.

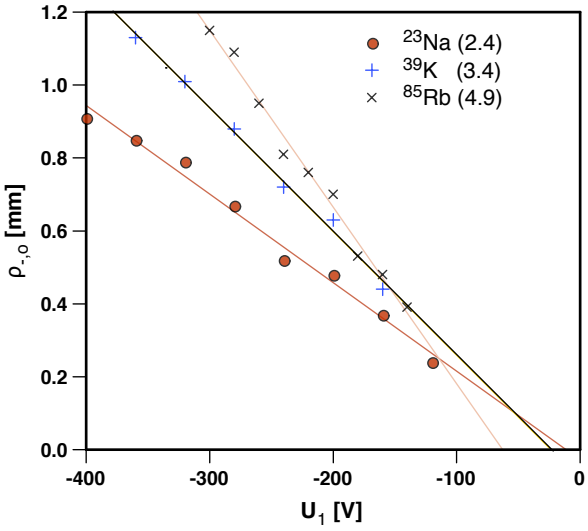

Figure 5.11. Initial ρ_- as a function of U_1 for three different ion species. The numbers in parentheses are the steering strength values in μm/V.

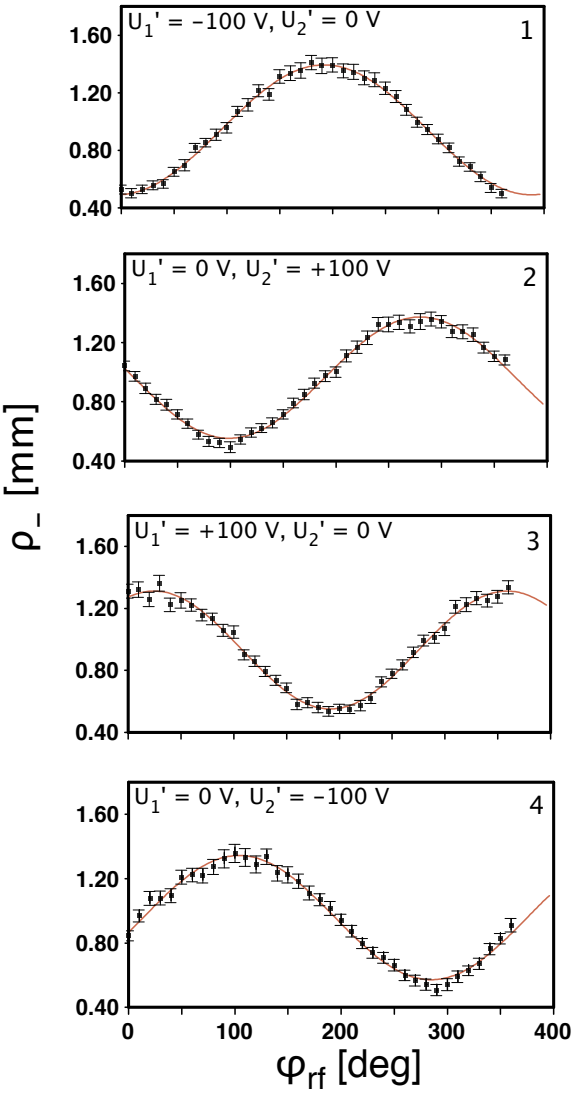

Figure 5.12. Magnetron amplitude ρ_- as a function of ϕ_{rf} of $^{39}K^+$ ions subjected to a dipolar RF field at frequency ν_- for an excitation time of $T_{rf} = 50$ ms. The choice of steering voltages is such that the ions should be captured on a circle at angles 90° apart. Solid lines are sinusoidal fits to the data. The fit results are summarized in Table 5.1.

CHAPTER 6

Mass Measurements of Stable Krypton Isotopes

Krypton beams from the test ion source have been used extensively to characterize the performance of the LEBIT Penning trap mass spectrometer in the regime of medium heavy masses. Mass measurements utilizing ^{86}Kr as a reference mass, measured to high precision by SMILETRAP [53], were performed on ^{78,80,82,83,84}Kr, revealing somewhat surprising results [54].

Initial LEBIT measurements had indicated that the AME03 [2] mass values of ^{83,84}Kr were too large. To explore this discrepancy in greater detail an additional series of measurement were performed in which 4-5 cyclotron frequency measurements were made of ^{78,80,82}Kr^{+} and 11 cyclotron frequency measurements were made of ^{83,84}Kr^{+}. Each of these individual measurements was bracketed by a cyclotron frequency measurement of the reference ion, ^{86}Kr^{+}. The time separating each reference measurement was approximately half an hour. During the measurement of any specific Kr isotope, possible contamination from the other isotopes was cleaned away via dipolar excitation as discussed in Section 3.1.3. Table 6.1 provides the frequency ratios obtained in the run with their statistical uncertainties in parentheses, and an

additional uncertainty of 1×10^{-8}, added in quadrature, in curled brackets. This additional uncertainty accounts for any additional systematic uncertainties that we have not been able to rule out.

Using the known mass value for ^{86}Kr and the frequency ratios obtained here, mass values for ^{78,80,82,83,84}Kr were obtained using an analysis application, SOMA, discussed in Appendix B, which I created to calculate final mass values from fits of the cyclotron resonances.

The final mass values are listed in Table 6.2 together with the AME03 [2] value and the difference between these values. This difference is shown as a function of mass number in Fig. 6.1.

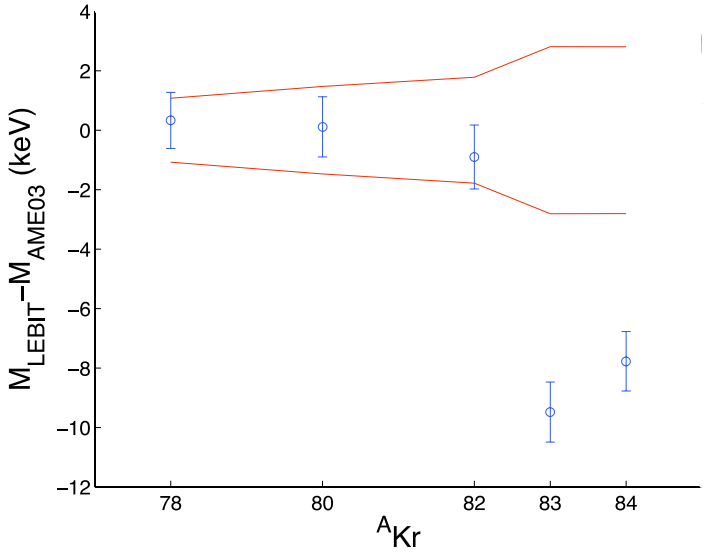

Figure 6.1. The difference between mass values measured with LEBIT and AME03 [2] for the stable krypton isotopes. The error band corresponds to the uncertainty of the literature values, the error bars to the uncertainty of the mass values determined in this work.

Excellent agreement is observed for the three isotopes ^{78,80,82}Kr within measurement uncertainties. The mass values for these isotopes are known with very high precision and are dominated by data from other Penning traps. A significant but

equally large deviation is observed for ^{83}Kr and ^{84}Kr for which the masses have been determined by many different and partially inconsistent data (discussed below). The observed averaged relative deviation of the LEBIT results from the AME03 values is less than 6×10^{-9}, if ^{83}Kr and ^{84}Kr are excluded. As a part of this measurement series, mass comparison of $^{86}Kr^{+}$ and $^{39}K^{+}$ yields a mass-dependent systematic effect of less than 10^{-9}/u.

An analysis of the data used in the Atomic Mass Evaluation [2] shows that mass values for ^{83}Kr and ^{84}Kr are determined via a network of Q-values from decays and reactions combined with data from doublet mass measurements. The mass values for ^{83}Kr and ^{84}Kr are linked strongly by an (n,γ) reaction [55] which has an uncertainty of 0.3 keV. The Q-value agrees within 1.5 σ with the value calculated from the LEBIT data. The absolute mass of ^{84}Kr is determined primarily by the Q-value of the β-decay ^{84}Rb(β^{+})^{84}Kr [56, 57], and the result of a doublet mass spectrometer measurement, C_6H_{12}-^{84}Kr [58]. The mass of ^{83}Kr is primarily determined by the link to ^{84}Kr, but also by a doublet mass measurement C_6H_{11}-^{83}Kr [58]. Two recent measurements of ^{84}Kr are not included in the AME03. One was made at Florida State University, FSU [59], and another [60] at ISOLTRAP [61].

Fig. 6.2 displays the deviation of mass excesses of ^{83,84}Kr, as determined by individual measurements, from AME03 values. The three measurements made using Penning traps, FSU, ISOLTRAP and LEBIT, of ^{84}Kr agree very well. The doublet measurements of both krypton isotopes in question also agree with the Penning trap measurements, but may have a slight systematic bias towards heavier masses. The mass excesses calculated from the results of the β decay measurements are obtained by using the AME03 values of the parent nuclei. The fact that they do not agree well with the Penning trap measurements could indicate that there is one or more incorrect input data used in the AME03 in the region of ^{84}Rb and ^{83}Br. Assuming that the AME03 mass values for ^{83}Kr and^{84}Kr are suspect, this provides great confidence in

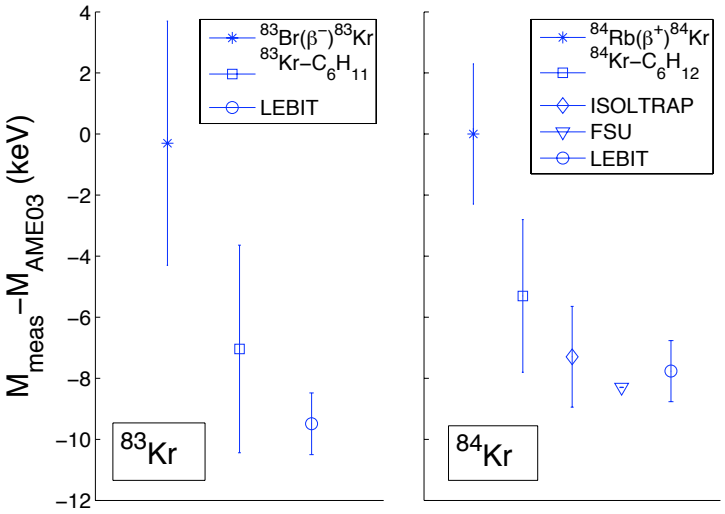

Figure 6.2. Deviation of individual mass measurements of ^{83,84}Kr from AME03. Values obtained from β decays use AME03 values for the masses of the parent nuclei.

the data obtained with LEBIT.

Table 6.1. Cyclotron frequency ratios $R = \nu(^{A}Kr^{+})/\nu(^{86}Kr^{+})$ obtained in this work. Column 1 contains the atomic number of the krypton isotope. Column two contains the weighted average of the measured ratios with the statistical uncertainties in parentheses and an additional 1×10^{-8} uncertainty, added in quadrature, in curled brackets.

A	$\bar{R}$
78	1.102 544 461(9){14}
80	1.075 006 812(9){14}
82	1.048 797 277(9){14}
83	1.036 139 857(9){14}
84	1.023 824 213(8){13}

Table 6.2. Mass excess values ME for krypton isotopes with mass number A as obtained from the measured frequency ratios and compared to their AME03 [2] values.

A	ME_{LEBIT} keV	ME_{AME03} keV	ΔME keV
78	-74179.4(0.9)	-74179.7(1.1)	0.3(1.4)
80	-77892.4(1.0)	-77892.5(1.5)	0.1(1.8)
82	-80590.4(1.1)	-80589.5(1.8)	-0.9(2.1)
83	-79991.2(1.0)	-79981.7(2.8)	-9.5(3.0)
84	-82438.8(1.0)	-82431.0(2.8)	-7.8(3.0)

CHAPTER 7

High-Precision Mass Measurement of ^{38}Ca and its Contribution to CVC Tests

The Conserved Vector Current (CVC) hypothesis asserts that the vector part of the weak interaction is independent of the nuclear interaction. This means that the vector coupling constant, G_v, is truly a constant and does not require renormalization. This constant, when combined with the purely leptonic muon decay constant, G_F, determines the up-down matrix element, V_{ud}, of the CKM quark-mixing matrix. Measuring the ft values of super-allowed $0^+ \rightarrow 0^+$ transitions allows G_v to be determined. A precise determination of V_{ud} has been, and continues to be, an important component in the test of the unitarity CKM quark-mixing matrix and the search for physics beyond the Standard Model. In order to determine the ft values the decay half life, the branching ratio for the $0^+ \rightarrow 0^+$ transition, and the Q_{EC} values need to be known. Small radiative and isospin-breaking corrections have to be applied to determine a corrected $\mathcal{F}$t value that can then be used for the test of CVC and the determination of V_{ud}.

To date there are 12 well-known CVC test candidates that provide an average $\mathcal{F}$t value with a relative uncertainty of 3.7×10^{-4}, as presented in a recent survey [1]. Nine of the candidates are close to the valley of stability and their Q_{EC} values were measured in reaction experiments. I will refer to these as classical candidates. Penning trap measurements of $0^+ \rightarrow 0^+$ emitters now allow us to determine high-precision Q_{EC} for isotopes which were inaccessible in the past. Three such species, ^{22}Mg [62, 63], ^{34}Ar [64] and ^{74}Rb [65], have recently been included in [1]. The addition of more candidates is important for testing the CVC hypothesis and for benchmarking the calculation of the theoretical corrections. Assuming CVC is true, the accuracy of the theoretical corrections to the ft values can be tested and their calculation can be improved. Nuclides with large theoretical corrections include the even-Z, $T_z = -1$ nuclei with $18 \leq A \leq 42$ and odd-Z, $T_z = 0$ nuclei with $A \geq 62$. ^{22}Mg, ^{34}Ar, ^{74}Rb, and ^{38}Ca, are among them. Penning trap mass measurements can also be used with advantage to revisit the classical cases. A Penning trap measurement of ^{46}V [66] with the CPT spectrometer at ANL found a significant deviation from the literature Q_{EC} value of the $0^+ \rightarrow 0^+$ decay of this nuclide, previously determined by an average of reaction measurements. A recent measurement with JYFLTRAP [67] validated CPT's result for ^{46}V. The JYFLTRAP group also measured the classical candidates ^{42}Sc, ^{26}Al^m and showed that speculations made in [66], that more reaction experiments might be wrong, could not be substantiated.

7.1 Experimental procedure

The data presented in this thesis were taken during two separate experiments in which the same primary beam was utilized. The first experiment was dedicated to studying the stopping and extraction of Ca ions from the gas cell, mass separation techniques, and identification of ^{38}Ca^{2+} ions in the Penning trap. A primary beam of ^{40}Ca at

140 MeV/u was produced by the CCF and reacted with a 460 mg/cm^2 beryllium target. The secondary beam was purified by the A1900 fragment separator [35] and delivered to the gas cell as a cocktail beam consisting of 50% ^{38}Ca, 35% ^{37}K and 15% ^{36}Ar. A series of range measurements were performed to study the stopping distribution of ions in the gas cell. A Si detector which can be positioned in the beam path was used to identify the ions passing through the gas cell by time of flight and energy loss. By varying the angle of the glass degrader the energy loss experienced by the ions passing through the degrader changes. Scanning the degrader angle and measuring the activity collected on the Si detector with and without buffer gas in the gas cell provided information on the fraction of the beam which was brought to rest in the gas cell.

After the optimal degrader angle was found the next step was to determine the chemical form of the ^{38}Ca activity extracted from the gas cell. Using the mass filter the activity was collected on the needle electrode as a function of the mass-to-charge ratio, A/Q, and the results are shown in Fig. 7.1. Peaks in the measured activity appeared at A/Q values of 28, 37, 46 and 55. This pattern is consistent with water molecules attached to $^{38}Ca^{2+}$ ions to form $[^{38}Ca(H_2O)_n]^{2+}$, with n = {1,2,3,4}. The appearance of water adducts was not particularly surprising due to the relatively-high water partial pressure in the gas cell resulting from an earlier venting and cleaning of the gas cell electrodes. The Q = +2 charge state is also to be expected as calcium has a second ionization energy of only 12 eV, while the first ionization energy of helium is 25 eV [68]. We chose the ions with A/Q = 28, corresponding to $^{38}Ca(H_2O)^{2+}$, to be transported to the cooler/buncher. It was found that collisions of the $^{38}Ca(H_2O)^{2+}$ ions with the helium gas in the cooler were energetic enough to dissociate the $^{38}Ca(H_2O)^{2+}$ ions into its constituent components, $^{38}Ca^{2+}$, A/Q = 19, and H_2O. This breakup allows for a very efficient suppression of undesired stable molecular ions with A/Q = 28 which were transported along with the $^{38}Ca(H_2O)^{2+}$

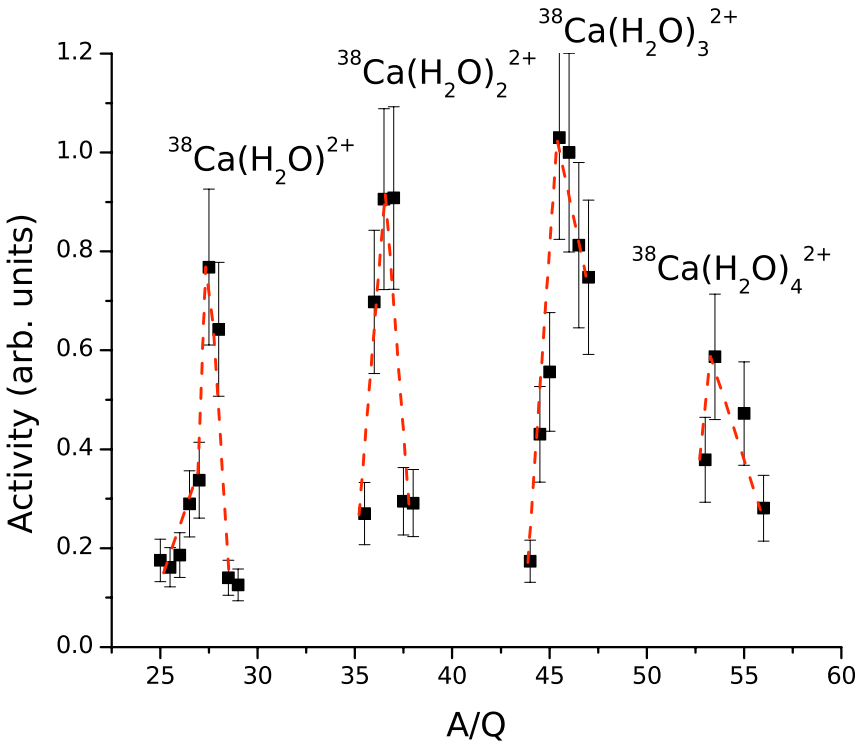

Figure 7.1. Activity as a function of the mass-to-charge ratio A/Q of ions extracted from the gas cell and selected with the mass filter. A ^{38}Ca secondary beam was stopped in the gas cell. Lines are to guide the eye. The radioactive molecular ions assigned to these peaks are indicated.

ions. The probability of a breakup of the contaminants into fragments with A/Q = 19 was found to be small. Therefore, the time-of-flight mass separation using the fast beam gate between the Penning trap and the cooler/buncher was very efficient. A few cyclotron resonance measurements of $^{38}Ca^{2+}$ were performed in the Penning trap during the first run to evaluate if a precision mass measurement of ^{38}Ca would be possible.

The second run was dedicated to the high-precision mass measurements of ^{37,38}Ca. Fig. 7.2 shows one of the $^{38}Ca^{2+}$ measurements taken during the second run. In this measurement an RF excitation time T_{rf} = 300 ms was used, which resulted in a resolving power of R = 2×10^6. A total of twenty-one resonance curves were obtained for $^{38}Ca^{2+}$. High-level contaminating molecules were identified by measuring

cyclotron frequencies over a broad frequency range and using SCM_Qt, described in Appendix C, to determine the molecules. In all of the $^{38}Ca^{2+}$ measurements, with the exception of the first seven measurements in this run, all conceivable contaminants were cleaned via dipolar excitation and the fast beam gate was used to suppress possible contaminating species with different A/Q values. Additionally, the number of ions simultaneously stored in the trap was kept at about 1 ion/cycle to avoid frequency shifts due to interactions with possible contaminants that were not being cleaned. Taking the MCP efficiency into consideration this was achieved by keeping the average number of ions detected per cycle to ≤ 0.4.

H_3O^+ ions from the gas cell were chosen as the reference species to calibrate the magnetic field. Alternating measurements of $^{38}Ca^{2+}$ and H_3O^+ were made. Because H_3O^+ has the same A/Q value as $^{38}Ca^{2+}$ it is an ideal reference species since it minimizes mass-dependent systematic effects. The same precautions were taken with for H_3O^+ cyclotron measurements as with the $^{38}Ca^{2+}$ measurements, such as cleaning of contaminants, single ion storage, etc. Reference measurements were taken on the order of every 20 minutes. The twenty one $^{38}Ca^{2+}$ measurements taken over a period of 22 hours were necessary to achieve the mass uncertainty required for a CVC test candidate. Each measurement consisted of the detection of approximately 300 ions.

7.2 Experimental results

As mentioned in Sec. 3.1.5, the primary experimental result of a mass measurement using the LEBIT mass spectrometer is the ratio, $R = \nu_c/\nu_{c,ref}$, of the measured cyclotron frequency, ν_c, of the ion of interest and that of the reference ion, $\nu_{c,ref}$. Each ν_c measurement should be bracketed by two $\nu_{c,ref}$ measurements which can be used to make a linear interpolation of the magnetic field. The cyclotron frequencies

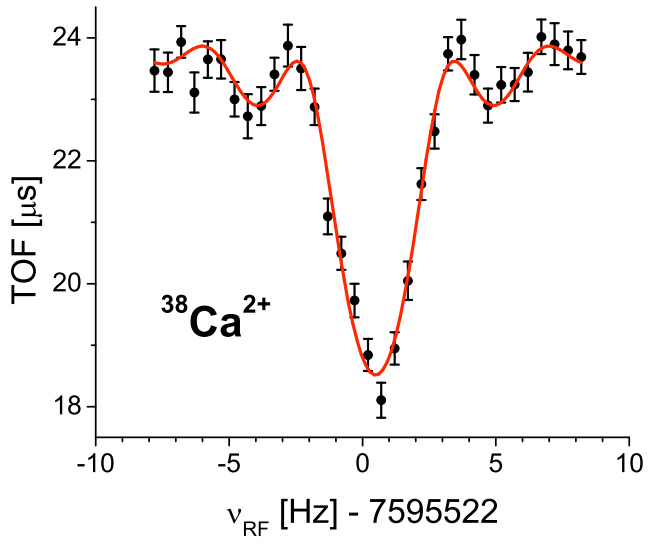

Figure 7.2. Cyclotron resonance of $^{38}Ca^{2+}$ measurement taken with an excitation time T_{rf} = 300 ms. The solid line is a fit of the theoretical line shape [3] to the data.

and their statistical uncertainties are determined by fitting the measured resonance curves using a theoretical line shape [3], as shown in Fig. 7.2. Other sources of uncertainty to be considered will be discussed later.

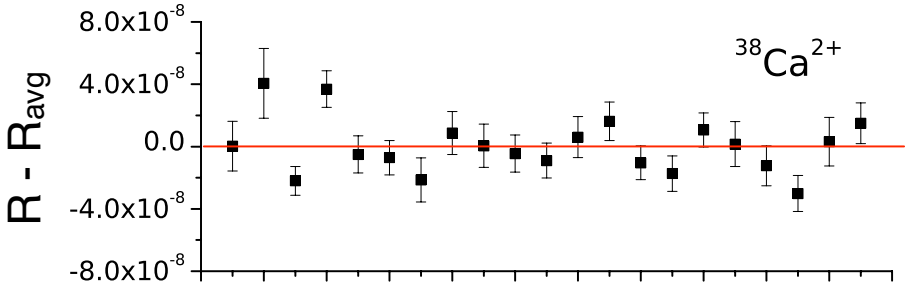

Figure 7.3. Deviation of individual frequency ratio measurements, R = $\nu_c/\nu_{c,ref}$, from the mean. The error bars correspond to the statistical uncertainty.

In the first run, which served as a feasibility test, $^{38}Ca^{2+}$ was identified in four cyclotron frequency measurements during the last 16 hours of the run. These data are not used in the final mass analysis since contaminants were not identified and cleaned. The fast beam gate had also not yet been installed, and the time separating

the reference measurements was on the order of hours.

An RF excitation time $T_{rf} = 200$ ms was used only on the first resonance taken during the second run. The remaining resonances were obtained using an RF excitation time $T_{rf} = 300$ ms. The first two resonances were also taken with the fast beam gate off and therefore exhibit a higher average rate of detected ions per cycle, $\overline{n} = 0.27, 0.37$ compared to a rate of $\overline{n} = 0.07 - 0.22$. During the 14 final measurements the cleaning scenario was in place and nothing was changed. Fig. 7.3 displays all of the frequency ratios obtained during the second $^{38}Ca^{2+}$ run. The mean value of all data taken during the second run, including those with larger count rates and incomplete cleaning is $\bar{R} = 1.001\ 592\ 097(3)$.

7.3 Uncertainty analysis

Experimental data obtained in various online and offline experiments were used to determine possible sources of uncertainty. The online data were analyzed for uncertainties associated with nonlinear magnetic field effects, systematic frequency shifts due to ion-ion interactions, and relativistic effects. The offline results include a mass measurement of $^{40}Ar^{2+}$ using $^{23}Na^{+}$ as a reference (both available from the test ion source), to test for any unforeseen uncertainties associated with mass measurements of doubly charged ions.

7.3.1 Analysis of online results

Magnetic field strength calibration

The linear interpolation of the magnetic field assumes that nonlinear magnetic field changes are insignificant. The greater the time span between reference measurements the greater the probability that nonlinear changes in the magnetic field become significant. Fig. 7.4 shows the magnetic field as a function of time, as determined

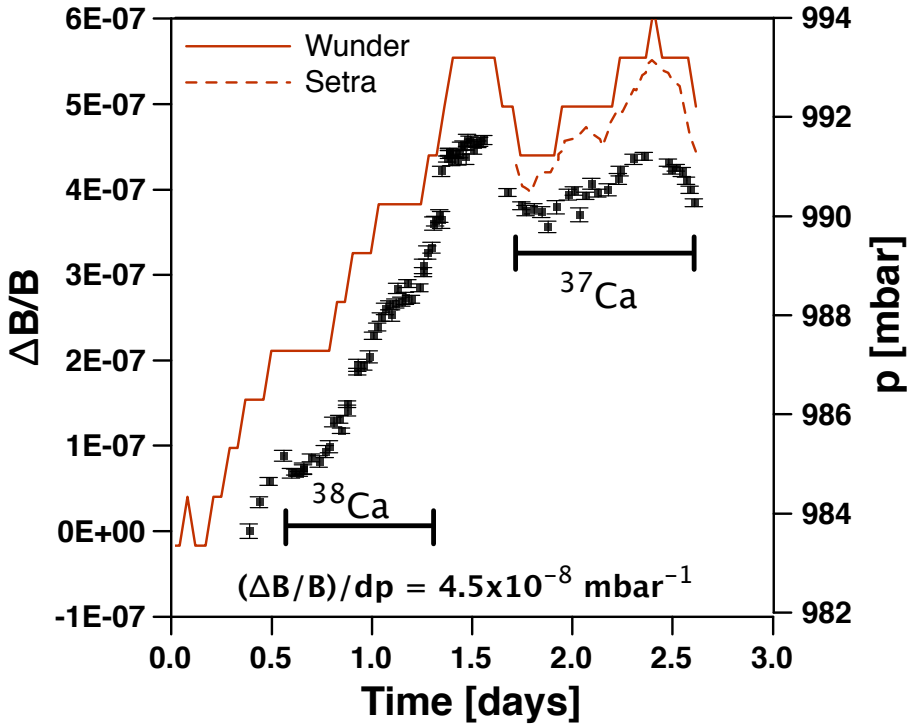

Figure 7.4. Variations of the magnetic field and atmospheric pressure vs. time. Data points are the relative change in the magnetic field as obtained from the reference measurements taken over the course of the second run. The Wunder line are pressure readings (obtained from a local weather station) near East Lansing, MI. The Setra line is pressure data taken with a precision barometer in the lab.

from cyclotron resonance measurements of the reference molecule, H_3O^+, over the course of the second run. The solid lines show the measured atmospheric pressure as a function of time obtained from a weather station and from a high-precision, absolute-pressure gauge brought into operation during the run. One can easily see that the magnetic field strength and the atmospheric pressure are correlated, an effect common to the type of superconducting magnet system used. Atmospheric pressure changes affect the internal pressure of the superconducting magnet's liquid helium bath. These pressure changes within the cryostat alter the boil-off rate of the helium, changing the temperature of the bath. It is suspected that this change in temperature changes the magnetic susceptibility of materials used in the construction of the

superconducting coils [69, 70], thus changing the total magnetic field strength. The atmospheric pressure dependence has since been removed by maintaining a constant pressure in the helium cryostat using an absolute-pressure gauge and electropneumatic valve operated on a PID loop. The internal pressure is now stable to about 10 ppm.

The uncertainty of the ratio of measured cyclotron frequencies due to the apparent nonlinearity in the temporal change of the magnetic field has been analyzed. The measured reference data were fitted with a polynomial function over the time span in which the $^{38}Ca^{2+}$ measurements were performed. Reference points were then generated for every minute along the fit line. Using these data points the deviation of the interpolated magnetic field strength B_{int} from the actual magnetic field strength B were determined. Choosing a time Δt between two reference measurements and stepping through the points the deviation $\Delta B = B - B_{int}$ was recorded. From the distribution of ΔB and including the statistical uncertainty of the cyclotron frequency determination a standard deviation $s(\Delta B)$ was obtained. Fig. 7.5 shows the variation of $s(\Delta B)/B$, as a function of the time Δt between any two reference measurements. For times $\leq$ 1 hr, $s(\Delta B)/B$ was found to be constant and is dominated by the statistical uncertainty of the cyclotron frequency measurement.

In order to obtain an estimate of the effect of non-linearities in the magnetic field changes a maximum time separation Δt = 1.5 h was chosen (note that ^{38}Ca reference measurements were performed every 20 min). A linear fit to the data at times less than 1.5 hr resulted in a slope of $2(1)\times10^{-10}$ hr^{-1}. The largest uncertainty yields a value of 3×10^{-10} as an estimate for the maximum systematic error, which is negligibly small.

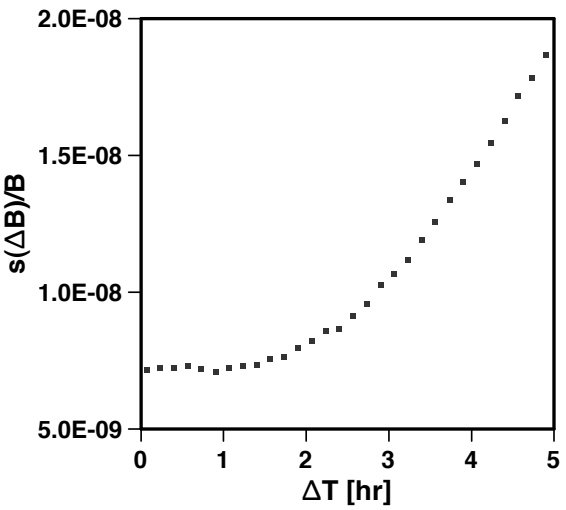

Figure 7.5. The magnetic field strength nonlinearity parameter, s(ΔB)/B, as a function of Δt between reference measurements.

Effects of contaminating ions and background events

Even though the number of detected ions per cycle was less than one for all of the $^{38}Ca^{2+}$ measurements in the second run, the first two $^{38}Ca^{2+}$ measurements in the second run did exhibit higher average counts per cycle. Fig. 7.6 displays the count rate information for the second ^{38}Ca run. The average number of counts/cycle for all of the measurements of $^{38}Ca^{2+} \approx 0.15$, while the maximum was ≈ 0.37. These measurements were sorted into count rate bins and used to calculate the mean frequency ratios. This procedure allowed identification of frequency shifts associated with residual contamination. Table 7.1 presents the mean frequency ratios obtained for the four bins. The frequency ratios in the first three bins, containing 19 of the 21 measurements, agree perfectly. The bin containing the measurements with the highest count rate exhibits a possible shift towards lower frequencies. A shift towards lower frequencies, i.e. heavier masses, has been found previously to be indicative of the presence of contaminating masses [71]. These two measurements with the highest count rate are among the first seven measurements of the second run. Evidence

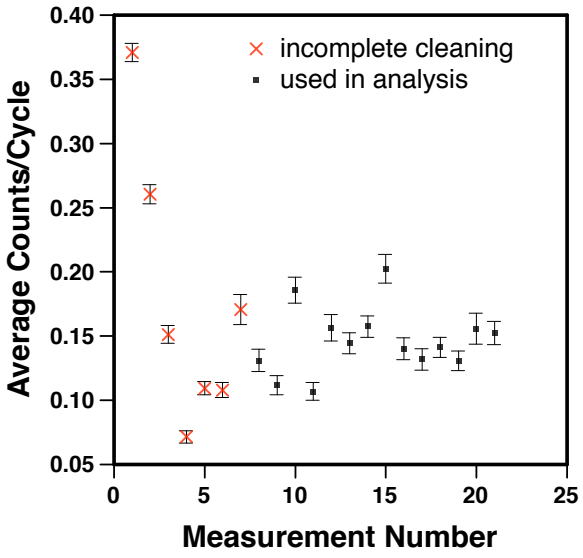

Figure 7.6. Average counts/cycle for each $^{38}Ca^{2+}$ measurement made in the second run. The first seven measurements have been excluded from the final analysis due to possible contamination and high count rates (see text).

of contamination disappeared after cleaning the possible contaminants via dipolar excitation was initiated. Therefore, we excluded the first seven measurements from the final mass analysis. A linear regression of the mean frequency ratios obtained from the three bins with the lowest count rates yields an additional uncertainty of 4×10^{-9} due to possible contamination.

Relativistic effects

Relativistic mass shifts will always occur to some degree in the cyclotron frequencies. As long as both the species of interest and the reference mass are a mass doublet and have the same initial magnetron radius, $\rho_{-,o}$, then the relativistic effects cancel in the determination of the frequency ratio. This should be the case as both $^{38}Ca^{2+}$ and H_3O^+ have the same A/Q = 19. The ion optics for the injection of the ions into the trap should be the same, and the ions should be captured into a magnetron orbit with the same amplitude. The initial magnetron radius is one of the parameters of the

Table 7.1. Count rate information for each $^{38}Ca^{2+}$ measurement of the second run. The bins are average counts/cycle. N is the number of measurements included in the bin.

Bin	N	$R = \frac{\nu_c}{\nu_{c,ref}}$
x≤0.11	5	1.001 592 097(11)
0.11<x≤0.15	8	1.001 592 098(10)
0.15<x≤0.20	6	1.001 592 097(12)
0.20<x	2	1.001 592 113(19)

theoretical line shape that is fitted to the resonance data. Fig. 7.7 shows the results for the initial magnetron radius for each H_3O^+ and $^{38}Ca^{2+}$ measurement. The average values for the initial magnetron radii obtained are $\bar{\rho}_{-,O} = 1.47(1)$ mm for the H_3O^+ and $\bar{\rho}_{-,O} = 1.46(10)$ mm for the $^{38}Ca^{2+}$ and agree within the uncertainties. The uncertainty in the value of the initial magnetron radius for the H_3O^+ is smaller due to the greater number of counts. Taking the uncertainty in the difference of the initial magnetron radii into consideration a maximum effect on the frequency ratios was calculated to be 3×10^{-9}.

7.3.2 Independent precision test with $^{23}Na^+$ and $^{40}Ar^{2+}$

Effects Due to Higher Charge States

A mass comparison of the stable, well-known ions $^{23}Na^+$ and $^{40}Ar^{2+}$ ions was performed as an independent test for possible systematic errors in the mass comparison of singly-to-doubly charged ions. The masses of these two nuclides are known with sub-ppb precision and are nearly a mass doublet which minimizes mass-dependent effects. Furthermore, ^{40}Ar has a second ionization energy of ≈ 28 eV [68], which is more sensitive to systematic charge exchange effects as compared to Ca which has a second ionization energy of only ≈ 12 eV.

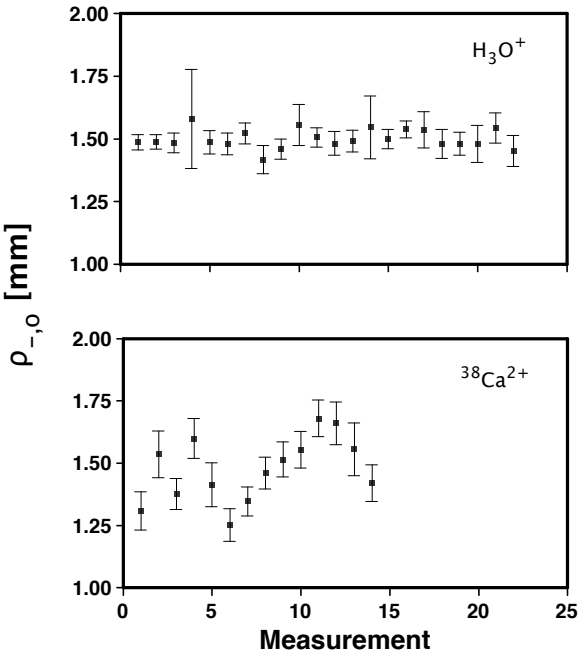

Figure 7.7. Initial magnetron radii, $\rho_{-,o}$, for $^{38}Ca^{2+}$ and H_3O^+ as determined from a theoretical fit to the cyclotron resonances.

Both $^{23}Na^+$ and $^{40}Ar^{2+}$ ions were obtained from the test ion source of LEBIT. Adjustments of the extracted beam current and the opening time of the ion source beam gate allowed the number of detected ions after the Penning trap to be maintained at < 1 count/cycle as in the calcium experiments. Also, a continuous dipolar cleaning of $^{40}Ar^+$ and He^+ was employed to remove potential charge-exchange products as they were created. Ten measurements were made in this test run, yielding a frequency ratio R = 1.150 574 623(5) resulting in an insignificant deviation of $3(5)\times10^{-9}$ from the ratio obtained from literature [2] values.

7.4 ^{38}Ca mass evaluation

A theoretical line shape [3] was fit to the $^{38}Ca^{2+}$ and H_30^+ cyclotron resonances, and the resulting fit files were entered into SOMA. Discarding the first seven mea-

surements of $^{38}Ca^{2+}$ of the second run and using the remaining 14 we obtain $\overline{R}$ = 1.001 592 097(3). Within rounding the same value obtained using all of the ^{38}Ca measurements. As an additional systematic error we quadratically add the sum of 3×10^{-9} for uncertainties in the magnetron radii and 4×10^{-9} for the presence of contaminating ions to the the statistical uncertainty and get a mean ratio of $\overline{R}$ = 1.001 592 097(8).

The atomic mass value of ^{38}Ca was then calculated by m(^{38}Ca)=2·$\overline{R}^{-1}$(m(H_3O)-m_e+b_1+2m_e-b_2), where b_1 = 5 eV [72] is the first ionization energy of H_3O, b_2 = 17 eV is the sum of the first and second ionization energies of ^{38}Ca, and m_e is the mass of the electron. The mass of H_3O is known with a precision of $\delta m/m < 10^{-9}$ and its uncertainty is negligible. The result is a mass excess for ^{38}Ca ME = -22058.53(28). This value agrees with the current literature value, ME = -22059.2(4.6) [2], but is over an order of magnitude more precise.

7.5 Impact of improved ^{38}Ca mass on the precision of the $\mathcal{F}$t value of the $0^+ \rightarrow 0^+$ decay

Using the mass excess of the $^{38}K^m$ 0^+ state from [1] an improved Q_{EC} = 6611.7(4) for the $0^+ \rightarrow 0^+$ transition of ^{38}Ca to $^{38}K^m$ can be calculated. The f value depends on the Q_{EC} value to the fifth power, so that the uncertainty is $(\delta f/f) \approx 5(\delta Q_{EC}/Q_{EC})$. The uncertainty in f introduced by the Q_{EC} using the improved ^{38}Ca mass value is only $\delta f/f = 3\times10^{-4}$, which is a factor of 12 smaller than the previous uncertainty. Fig. 7.8 shows the relative uncertainties in f, $\delta f/f$, of the 12 most precisely known $0^+ \rightarrow 0^+$ decays from Hardy and Towner's most recent survey [1], along with the relative uncertainty in f of the ^{38}Ca decay using the new LEBIT mass value. The new ^{38}Ca mass value reduces the relative uncertainty in f of the ^{38}Ca decay to the same order as that of the most precisely known super-allowed $0^+ \rightarrow 0^+$ decays.

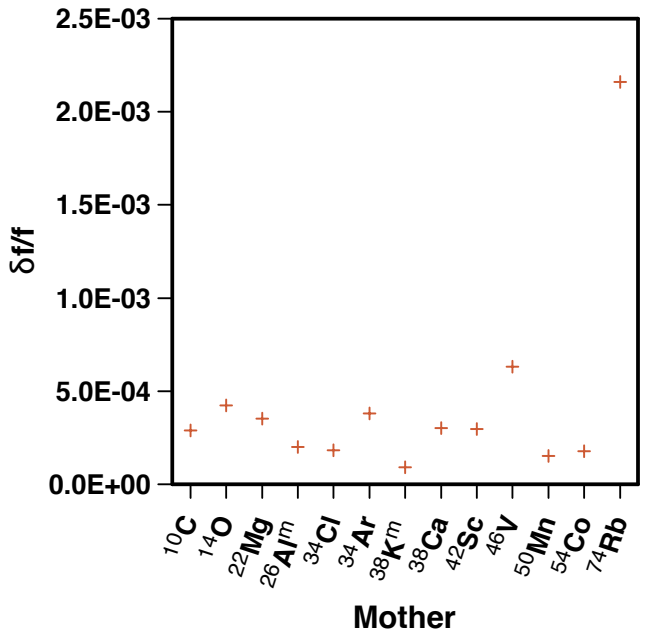

Figure 7.8. The relative uncertainties in f, δf/f, due to the uncertainties in the Q_{EC} value of the 12 most precisely known $0^+ \rightarrow 0^+$ decays [1] and ^{38}Ca using the new LEBIT mass value.

Fig. 7.9 shows the $\mathcal{F}$t values for the 12 most precisely known $0^+ \rightarrow 0^+$ decays. The solid lines represent the uncertainty in the mean $\mathcal{F}$t value calculated from these results. The precision limit of the $\mathcal{F}$t value for ^{38}Ca due to the improved mass value from this work is also shown. The absolute $\mathcal{F}$t value for ^{38}Ca is not yet determined as the branching ratio is unknown and the uncertainty in the half life is large. Results of measurements recently performed at Texas A&M [73] and ISOLDE [74] may reduce the half life uncertainty and determine the branching ratio. In the meantime, the mass of ^{38}Ca has been measured at ISOLTRAP with less precision [75], but the value agrees with the mass value obtained with LEBIT.

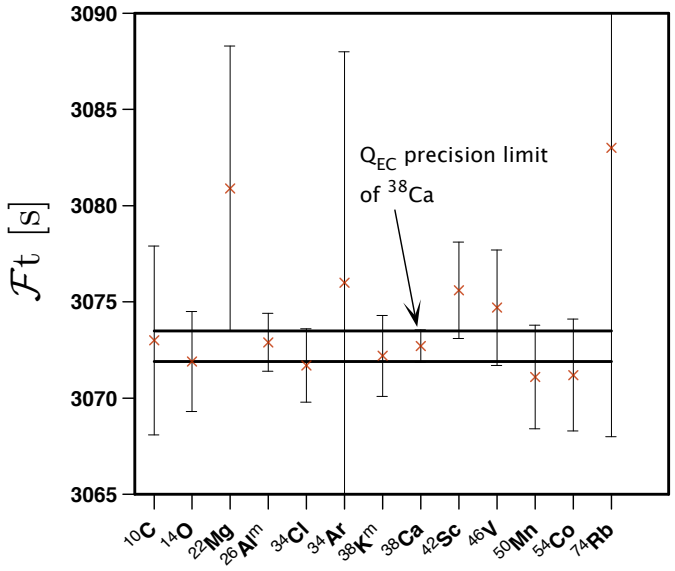

Figure 7.9. The 12 most precise $\mathcal{F}$t values from a recent review [1] along with the ^{38}Ca precision limit due to new mass value (see the text). Solid lines represent the uncertainty in the mean $\mathcal{F}$t value.

CHAPTER 8

Summary

In 2000 the initial design work on the Low Energy Beam and Ion Trap project at the Coupled Cyclotron Facility of the NSCL was begun. By 2004 the system was complete and commissioning of the entire apparatus was begun. In May of 2005 the first mass measurement of a radioactive species, ^{38}Ca, was performed. Thus it was proven that radioactive beams created via fast-beam fragmentation can be prepared with excellent beam properties and high purity which are required for high-precision mass measurements. In the future it is envisioned to make these low-energy purified beams available for other experiments such as laser spectroscopy for the study charge radii and moments of rare isotopes or for post-acceleration for nuclear astrophysics experiments.

In the five years required to bring LEBIT to its fully operational state, many students, post-docs and faculty have contributed to its success. My Ph.D. work emphasized the design, construction and commissioning of the LEBIT 9.4 T Penning trap system, the exploration of the octupolar RF excitation, the surprising ^{83,84}Kr mass measurement and the mass measurement of the short-lived $0^+ \rightarrow 0^+$ β emitter, ^{38}Ca.

The design of the LEBIT high-precision Penning trap required extensive simula-

tions to reduce the electric field imperfections while simultaneously minimizing the effects of magnetic field inhomogeneities introduced by the materials used to construct the trap. Several iterations and a close collaboration with the design department was required.

Many systematic studies of the 9.4 T Penning trap system were performed with stable species to assess the absolute accuracy achievable, and has been reduced to $\leq 10^{-9}$. Improvements were also made along the way to actively compensate the natural magnetic field decay during long measurements a counter-current introduced via a coil wrapped around the bore tube. Magnetic field changes were further reduced by stabilizing the pressure of the magnet's liquid helium bath.

The first radioactive mass measurement of ^{38}Ca was performed in May of 2005, followed up with another experiment in July 2005 where ^{37}Ca was also measured. The analysis of the ^{38}Ca data was presented in this thesis and a final mass excess of ME = -22058.52(17) was obtained, which agrees with the current literature value of ME = -22059.2(4.6), but is about 30 times more precise. An experiment at Texas A&M university, led by John Hardy, was recently performed to determine the half life and branching ratio of the ^{38}Ca β decay, which is necessary to calculate the $\mathcal{F}$t value. The results are forthcoming.

Since those first experiments the LEBIT group has been working hard to extend the mass measurement program. In a year and a half of operation a total of 26 radioactive masses have been measured: ^{37,38}Ca, ^{64,65,66}Ge, ^{40,41,42,43,44}S, ^{66,67,68,80}As, ^{29,34}P, ^{63,64}Ga, ^{68,69,70,81m,81g}Se, ^{33}Si, ^{70m,71}Br. This is a very successful beginning of a mass measurement program which is expected to contribute not only to our understanding of nuclear physics, but also to make important contributions to other fields, such as nucleosynthesis and tests of fundamental interactions and symmetries.

APPENDICES

APPENDIX A

Solution to the Electric Potential of an Infinite Quartered Cylinder

Here I present the solution of the electric potential of the infinite quartered cylinder. Using the solution an analytic expression for the electric field can be calculated and used as an approximation for the electric field produced by the Lorentz steerer introduced in Chapter 5. The easiest method for solving the electric potential of the quartered cylinder is to first solve for the halved-cylinder potential and then sum over four different orientations to arrive at the solution to the quartered cylinder. The process is illustrated in Fig. A.1

To begin, the general solution to the Laplace equation in polar coordinates is given by

$$V(r,\phi) = [a + b \cdot ln(r)][A + B \cdot \phi] + \sum_{n=1}^{\infty} \left[a_n r^n + b_n r^{-n}\right] [A_n \cos(n\phi) + B_n \sin(n\phi)] \,. \tag{A.1}$$

The following list of boundary conditions must be met in order to physically describe the system:

- *V is finite at the origin* $\rightarrow b = b_n = 0$.

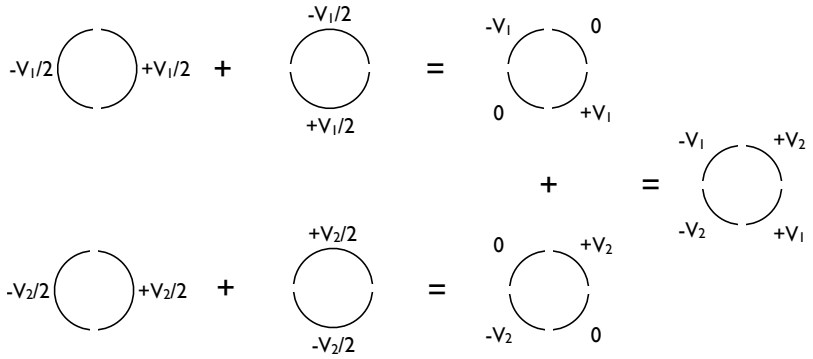

Figure A.1. Cartoon illustrating the method used to solve for the electric potential of a quartered cylinder.

- *V is an odd function of* $\phi \rightarrow A = A_n = 0$.
- *V(r,0) = V(r,2π) = 0* $\rightarrow$ *B=0 and n is integer.*

The application of these boundary conditions reduce Eq. A.1 to

$$V(r,\phi) = \sum_{n=1}^{\infty} B_n r^n \sin(n\phi). \tag{A.2}$$

By using the orthogonality of sin(nϕ)sin(mϕ) over the range of 0 to 2π the B_n coefficients can be solved for on the boundary of radius R at a potential $\pm V_1$.

$$B_n = \frac{\int V \sin(n\phi) d\phi}{R^n \int \sin^2(n\phi) d\phi} = \frac{\int_0^{\pi} V_1 \sin(n\phi) d\phi - \int_{\pi}^{2\pi} V_1 \sin(n\phi) d\phi}{R^n \int_0^{2\pi} \sin^2(n\phi) d\phi} = \frac{2V_1[1-\cos(n\phi)]}{R^n \pi n} \tag{A.3}$$

The first few terms of the expansion are

$$\begin{aligned} B_1 &= \frac{4V_1}{\pi R} \\ B_2 &= 0 \\ B_3 &= \frac{4V_1}{3\pi R^3} \\ B_4 &= 0 \\ B_5 &= \frac{4V_1}{5\pi R^5} \\ &. \\ &. \\ B_{2n} &= 0, n > 2 \\ B_{2n+1} &= \frac{4V_1}{(2n+1)\pi R^{2n+1}}, n > 2 \end{aligned} \tag{A.4}$$

Now use $(\mathrm{re}^{i\phi})^n$ - $(\mathrm{re}^{-i\phi})^n = 2\mathrm{ir}^n\sin(\mathrm{n}\phi)$ and rewrite Eq. A.2 as

$$V = \frac{4V_1}{2\pi i}\sum_{n=1}^{\infty}\frac{z^n - (z^n)^*}{n} \tag{A.5}$$

where $\mathrm{z} = (\mathrm{re}^{i\phi})$.

Using the sum

$$\frac{1}{2}\sum_{n=0}^{\infty} ln\left(\frac{1+n}{1-n}\right) = n + \frac{n^3}{3} + \frac{n^5}{5} + ... \tag{A.6}$$

allows us to rewrite Eq. A.5 as

$$V = \frac{2V_1}{\pi} Im\left[ln\left(\frac{1+z}{1-z}\right)\right], z = \frac{re^{i\phi}}{R}. \tag{A.7}$$

By summing over all of the configurations show in Fig. A.1 the final solution for the potential of a quartered cylinder is

$$\begin{aligned} V = \; & \frac{V_1}{\pi} Im\left[ln\left(\tfrac{1+z}{1-z}\right) + ln\left(\tfrac{1+y}{1-y}\right)\right] + \\ & \frac{V_2}{\pi} Im\left[ln\left(\tfrac{1+x}{1-x}\right) + ln\left(\tfrac{1+w}{1-w}\right)\right] \end{aligned} \tag{A.8}$$

where $\mathrm{z} = \mathrm{x} = \frac{re^{i\phi}}{R}$, $\mathrm{y} = \frac{re^{i(\phi-\pi/2)}}{R}$, $\mathrm{w} = \mathrm{y} = \frac{re^{i(\phi+\pi/2)}}{R}$.

Expanding the logarithm terms and converting back into cylindrical coordinates, the potential can be written as

$$\begin{aligned} V(r,\phi) = \quad & \frac{V_1}{\pi}\left[\tan^{-1}\left(\frac{2Rr\sin(\phi)}{R^2-r^2}\right) - \tan^{-1}\left(\frac{2Rr\cos(\phi)}{R^2-r^2}\right)\right] + \\ & \frac{V_2}{\pi}\left[\tan^{-1}\left(\frac{2Rr\sin(\phi)}{R^2-r^2}\right) + \tan^{-1}\left(\frac{2Rr\cos(\phi)}{R^2-r^2}\right)\right] \end{aligned} \tag{A.9}$$

APPENDIX B

SOMA documentation

B.1 Introduction

SOMA, Simple Online Mass Analysis, is a program designed for online analysis of Penning trap mass measurement data. Ease of use, accuracy of results and easy integration with software currently used at LEBIT, i.e., Mass Measure and Eva (maintained by Stefan Schwarz), were the primary design considerations. SOMA can be used independently of these pieces of software if the measurement data follows the Eva data formats.

With LEBIT there are three steps in the data acquisition and analysis processes:

- Use Mass Measure to collect time-of-flight spectra as a function of applied RF frequency and write the results to a data file.
- Use Eva to process the data files from Mass Measure and make fits of the time-of-flight spectra and write the results to a fit file.
- Use SOMA to process fit files from Eva to calculate a final mass value.

Eva outputs two ascii files from fits generated from data collected with Mass Measure, and use the extensions .log and .ft2. Either of these files can be used with

SOMA. The .log file contains more information, but none of it is used in the SOMA evaluation.

SOMA was written in Qt and has been compiled for Windows, OSX and Linux. Qt is a C++ development framework which is free for open source development and can be downloaded from www.trolltech.com.

A folder named massdata must be located in the same folder as the SOMA binary file. Within this folder are two text files which SOMA requires for operation. The awm03.txt file is the AME03 [2] data file and element_names.txt contains the elemental abbreviations and proton number. Both files must be present or an error will be presented upon opening SOMA.

B.2 Getting to Know SOMA

B.2.1 The main window

Upon opening SOMA the user is presented with the window shown in Fig. B.1. The main window is separated into two sections, the calibration menu on top and the measurement menu on the bottom. Valid calibration files, *.log and *.ft2 as provided by Eva, can be dragged and dropped into the *Calibration Menu*, or the *Load File* button can be used. When two or more calibration files have been loaded SOMA will display magnetic field decay information to the right of the data file list.

Any number of measurement species can be analyzed at one time. In order to load a new measurement species a new mass tab must be created. In the measurement menu use the *Add Tab* button to create a blank tab. Now drag the files corresponding to a single species into the newly created tab. Do this for each measurement species. Fig. B.1 shows that 25 $^{86}Kr^{+}$ files have been added to the *Calibration Menu* and 5 mass tabs have been added for the other stable krypton isotope measurements. Tabs can be removed using the *Remove Tab* button. Highlighting rows in either

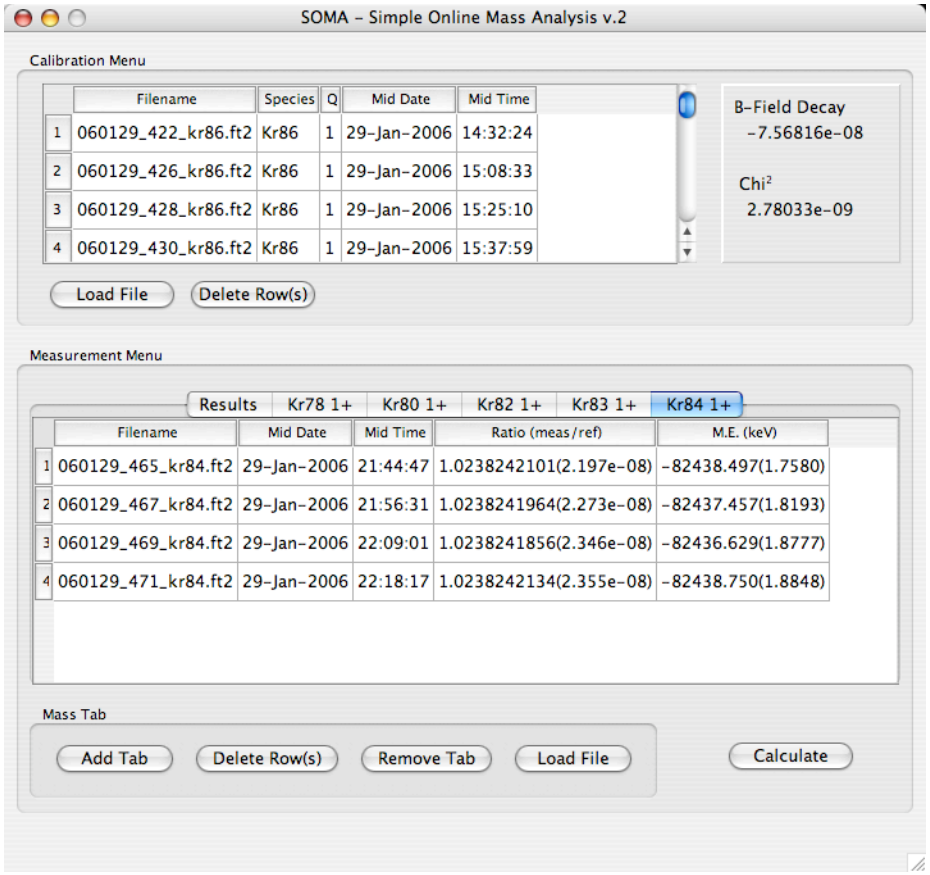

Figure B.1. The SOMA *Main Window* which is presented upon opening the application.

menu section and pushing the corresponding *Remove Row*(*s*) button removes the highlighted files.

Pressing the *Calculate* button will calculate the results of the mass measurements which have been loaded into SOMA. Each mass measurement must fall between two calibration measurements. If any mass measurement lays outside the range of the loaded calibration files then a warning will be displayed and that measurement will not be included in the final analysis. Due to the manner in which SOMA calculates the final mass, all measurements in a mass tab must have the same calibration species for the first calibration measurement. The second calibration measurement does not need to be the same element/molecule as the first measurement as the ratio of

frequencies is only calculated with the first calibration measurement. The first mass measurement in a mass tab determines the first calibration species. For any additional mass measurements in the tab which do not share the same first calibration species a warning will be displayed and that measurement will not be included in the final analysis.

If the user is interested in seeing how the final analysis changes by excluding certain calibrations or mass measurements, simply highlighting the rows containing the unwanted measurements and pressing the *Calculate* button will recalculate the results without having to remove the files from SOMA. To undo simply removing the highlighting and press the *Calculate* button again. The results of the mass analyses are presented in the results tab in the *Measurement Menu*.

There are two menus in the menu bar, *File* and *Tools*, each containing several actions. First I will cover the actions in the *File* menu. The *New* action clears out all files that are currently loaded into SOMA. *Save* will save an ascii file with a .par extension which contains all the files, uncertainties and electron binding energies that are currently loaded into SOMA. *Load* loads a .par file. *Export* will export data in an ascii format for importing into another program. Upon selection *Export* a dialog box with three check boxes is displayed. The check boxes available are *Calibrations*, *Measurements* and *Results*. Checking these boxes will choose what is to be exported. Pressing the *Save* button will opens another dialog where a base filename and location is to be chosen for the exported data. The *Tools* menu contains three actions, *Uncertainties*, *Info* and *Plots*. Each of these actions open a separate dialog box which will be covered in the next sections.

B.2.2 The uncertainty window

The uncertainty window (Fig. B.2) contains two tabs, *Uncertainties* and *Electron Binding Energies*. The *Uncertainties* tab contains a table with a row

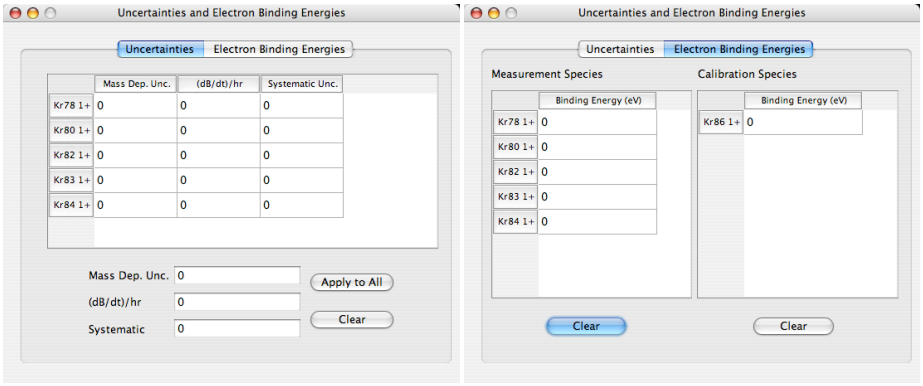

Figure B.2. The SOMA *Uncertainty Window* accessed through the *Tools* menu.

for each mass tab in the main window. There are three columns, *Mass Dep. Unc.*, $(dB/dt)/hr$ and *Systematic Unc.*. Each column represents a possible uncertainty which can be added into the final mass analysis. The *Mass Dep. Unc.* is in units of relative deviation per mass unit. This shifts the final mass value and adds an additional uncertainty to correct for identified mass-dependent effects. $(dB/dt)/hr$ accounts for magnetic field fluctuations over time as described in [30]. *Systematic Unc.* is an additional systematic uncertainty, such as the known precision limit of the spectrometer, applied to the final analysis and won't be reduced by additional statistics. Three line edits appear below the table and are used to apply the same values for each of the three types of uncertainties to each measurement species. The *Clear* button zeros out all uncertainties.

The *Electron Binding Energies* tab contains two separate tables, one for the calibrations and one for the mass measurements. Here you can enter the total electron binding energies for inclusion in the final mass analysis. Two *Clear* buttons zero out the entered values.

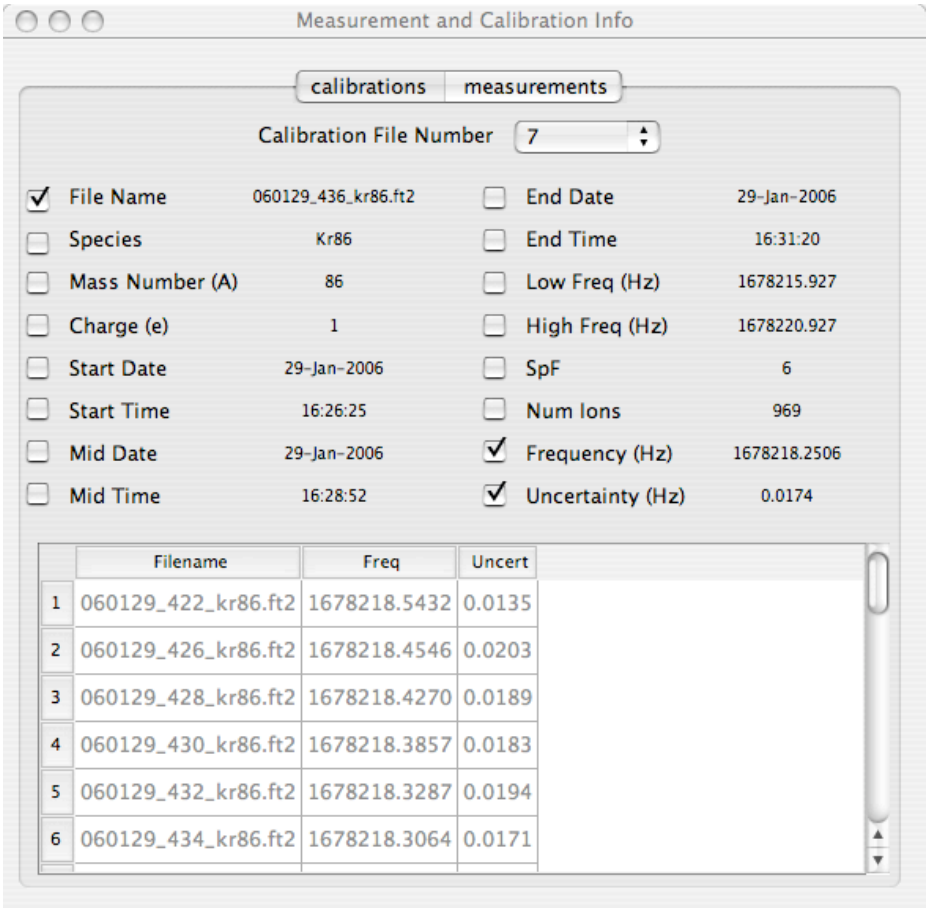

Figure B.3. The SOMA *Info Window* accessed through the *Tools* menu.

B.2.3 The info window

The info window (Fig. B.3) provides detailed information of the calibration and mass measurement files loaded into SOMA. There are two tabs at the top of the window, *Calibrations* and *Measurements*, which allow you to switch between the two file types. In order to view the measurement files the proper mass tab must be selected in the main window. In both cases, selecting a number in the combo box which corresponds to the number of the calibration or mass measurement as shown in their respective tables displays all the information for that given file. By checking the check boxes next to the parameter descriptions you can toggle if the information for all files is shown in the table.

B.2.4 The plot window

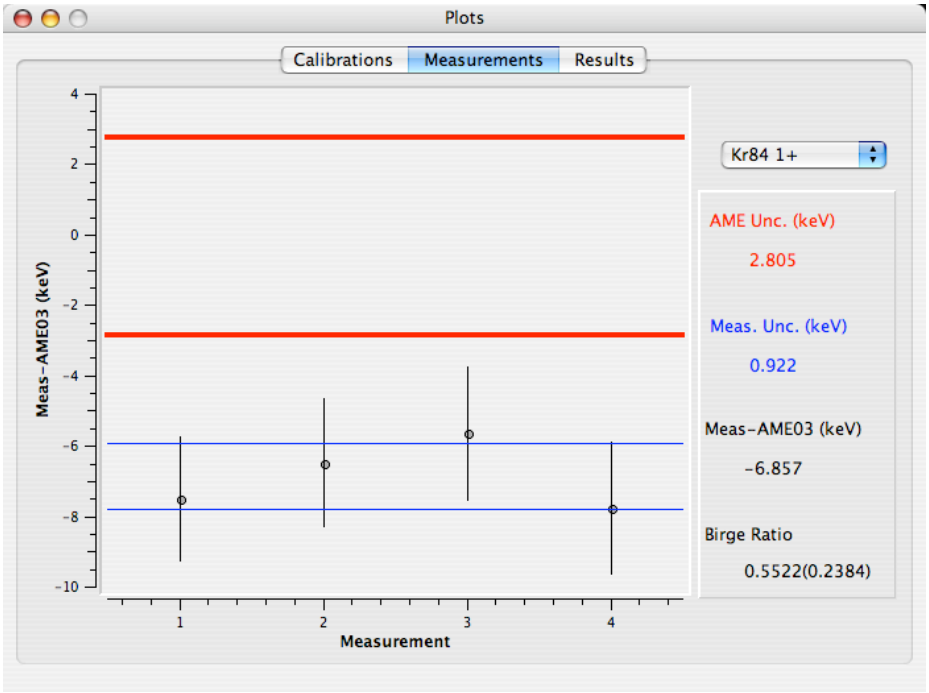

Figure B.4. The SOMA *Plot Window* accessed through the *Tools* menu.

The plot window contains three tabs, *Calibrations*, *Measurements* and *Results*, each of which displays a different plot. The calibration plot uses the calibration measurements to plot the decay of the magnetic field and fits it to a linear function. The measurement plot plots the individual measurements from each mass tab, shown in Fig. B.4. There is a combo box on the right hand side which can be used to switch between the different measurement species. The y-axis is the energy difference, in keV, of the measurement value minus the AME03 [2] value. The solid red lines represent the uncertainty in the AME03 value while the solid blue lines represent the uncertainty in the measurement mean value. A box to the right of the plot displays some relevant information, such as the AME uncertainty, the measurement uncertainty, the difference of the means and the Birge ratio [76] of the measured data. The results plot plots the final mass value for each mass tab along with the AME03

uncertainty. The y-axis is again the energy difference.

B.3 Analysis Methodology

In this section I will cover the methods SOMA uses to arrive at a final mass value given a set of measurement and calibration data. The mass calculation routine is a loop over all entries in an individual mass tab. If there are multiple mass tabs then the loop repeats until they have all been calculated. Table B.1 lists the constants and their hard-coded values which are used by SOMA.

Table B.1. SOMA constants and values

Constant	Value
π	3.14159265358979
m_e (keV)	510.99898565154
U (keV/amu)	931494.013

The first step in the analysis is to read the date and time of the measurement and find the two nearest reference measurements with respect to time, one before and one after. If the measurement does not lie between two references it is ignored and a warning is issued. Once the two references have been determined a linear interpolation of first reference's value of ν_c is performed based on the magnetic field defined by the ν_c's of the two references. The uncertainty associated with this interpolation is given by the uncertainty in the χ^2 fit [77] and will be labeled σ_{interp}. Next the ratio of the measurement and calibration frequencies calculated and defined as

$$R = \frac{\nu_{c(meas)}}{\nu_{c(ref)}}. \tag{B.1}$$

The uncertainty in this ratio is defined as

$$\sigma_R = R \cdot \sqrt{\left(\frac{\sigma_{interp}}{\nu_{c(interp)}}\right)^2 + \left(\frac{\sigma_{meas}}{\nu_{c(meas)}}\right)^2}. \tag{B.2}$$

An additional term must be taken into account when considering the uncertainty in the ratio. The nonlinear magnetic field term, $\sigma_{B(t)}$, described in Sec. B.2.2, is introduced in the corrected ratio uncertainty as

$$\sigma_{R(corr)} = \sqrt{\sigma_R^2 + (\Delta t \cdot \sigma_{B(t)} \cdot R)^2}, \tag{B.3}$$

where Δt is the time separation between the two reference measurements and $\sigma_{B(t)}$ is the mass-dependent uncertainty specified in the uncertainty window. Once this has been calculated for all measurements in a mass tab the mean ratio is calculated by

$$\bar{R} = \frac{\sum_{meas} \frac{R}{\sigma^2_{R(corr)}}}{\sum_{meas} \frac{1}{\sigma^2_{R(corr)}}}. \tag{B.4}$$

In order to determine if the measurement data scatter is statistical, the Birge ratio is calculated, defined by ratio of the outer over inner uncertainties. The outer and inner uncertainties are defined by

$$\sigma_{out} = \sqrt{\frac{\sum_{meas} \left(\frac{R - \bar{R}}{\sigma_{R(corr)}} \right)^2}{(N-1) \sum_{meas} \frac{1}{\sigma^2_{R(corr)}}}} \tag{B.5}$$

$$\sigma_{in} = \sqrt{\frac{1}{\sum_{meas} \frac{1}{\sigma^2_{R(corr)}}}}. \tag{B.6}$$

The uncertainty in the Birge ratio as given in [76] is $0.4769/\sqrt{n}$. A Birge ratio of 1 means that the measurement fluctuations are purely statistical. While if the ratio is greater than one it could indicate that there are additional systematic uncertainties which aren't accounted for. A Birge ratio of less than one could indicate that the uncertainties of the measurements have been overestimated.

The mean ratio, $\bar{R}$, needs to be corrected for any mass-dependent shifts inherent in the system, and is defined by

$$\bar{R}_{corr} = \bar{R} + \sigma_M \cdot \bar{R} \cdot (A_{meas} - A_{ref}), \tag{B.7}$$

where σ_M is the mass-dependent uncertainty. Using $\bar{R}_{corr}$ the corrected mass of the measurement species can be calculated as

$$M_{meas} = \frac{q_{meas}}{q_{ref}} \cdot \bar{R}_{corr} \cdot (M_{ref} - q_{ref} \cdot m_e + b_{ref}) + q_{meas} \cdot m_e - b_{meas}, \quad \text{(B.8)}$$

where q_{ref} is the charge state of the reference, b_{ref} is the total electron binding energy of the reference ion's missing electrons, q_{meas} is the charge state of the measurement species and b_{meas} is the total electron binding energy of the measurement ion's missing electrons. The absolute final uncertainty is given by

$$\sigma_{abs} = \sqrt{\sigma_{in}^2 + (\sigma_{sys} \cdot \bar{R})^2}, \quad \text{(B.9)}$$

where σ_{sys} is the additional systematic uncertainty specified in the uncertainty window. The final mass uncertainty is then

$$\sigma_M = \sqrt{(M_{ref} \cdot \sigma_{abs})^2 + (\bar{R}_{corr} \cdot \sigma_{M,ref})^2}, \quad \text{(B.10)}$$

where $\sigma_{M,ref}$ is the uncertainty in the mass of the reference species in amu.

APPENDIX C

SCM_Qt Documentation

C.1 SCM_Qt Intro

SCM_Qt (Search for Contaminant Masses) is a program designed to identify contaminants in a Penning trap. It is based on a similar command-line-based program first written by Stefan Schwarz. By measuring the cyclotron frequency ν_c of the contaminant ion and comparing it to a reference ion it is possible to generate a list of possible contaminants.

In order to run the *data_files* folder must be located in the same directory as the SCM binary. This directory contains four ascii files which SCM uses during normal operation. The awm03.txt is the AME03 [2] data, element_list.txt is a list of chosen elements and will be described later, element_names.txt contains the elemental abbreviations and proton number and nubtab03.txt which contains the NUBASE03 nuclear data compilation [78].

SCM_Qt was written in Qt and has been compiled for Windows, OSX and Linux. Qt is a C++ development framework which is free for open source development and can be downloaded from www.trolltech.com.

C.2 Using SCM_Qt

C.2.1 The main window

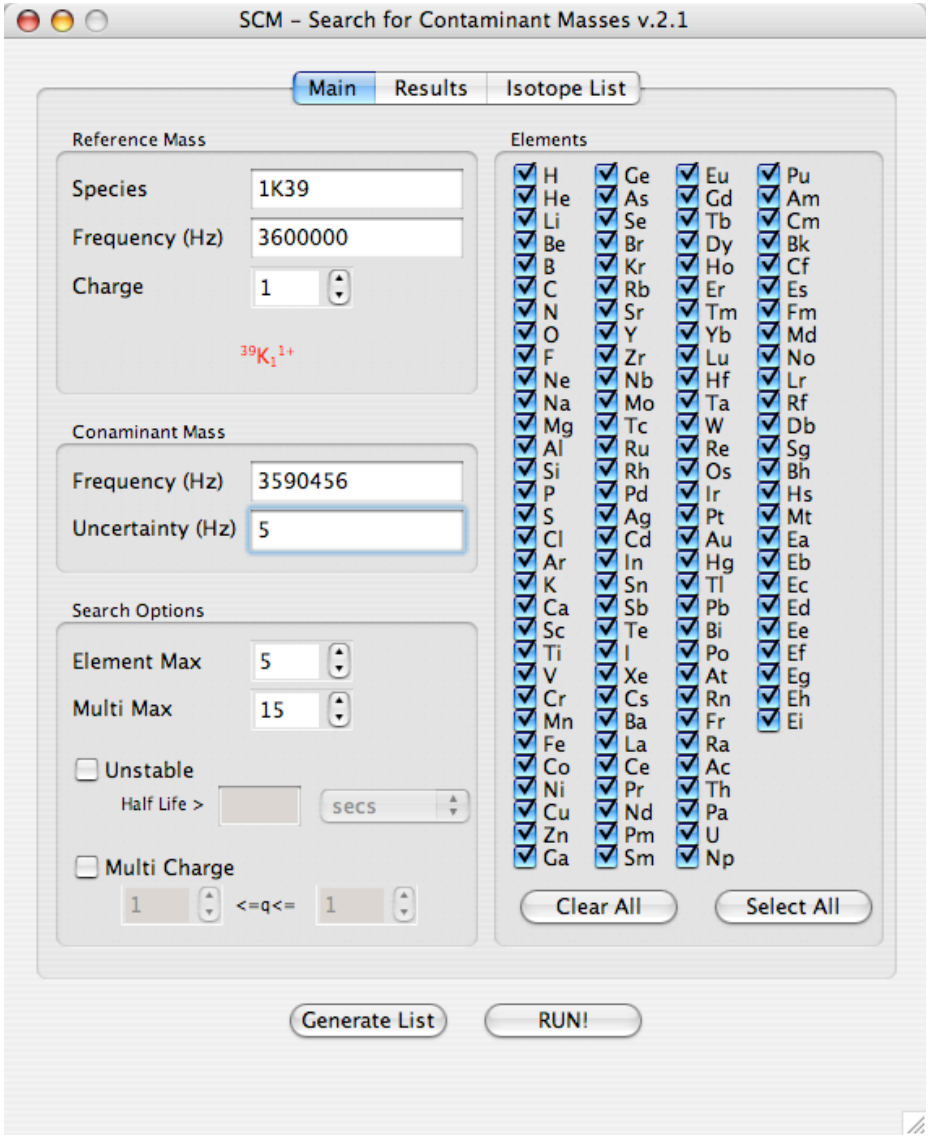

Figure C.1. The SCM_Qt *Main Window* which is presented when opening SCM_Qt.

The main window, as shown in Fig. C.1, is the first thing the user sees when launching SCM_Qt, and where most of the work will be done. The *Main Window* consists of 4 sub-areas: the *Reference Mass* area, the *Contaminant Mass* area, the *Search Options* area and the *Elements* area. Each of these sub-areas will be

described in full detail in the following sections.

The *Reference Mass* area is where the user enters information concerning the reference mass calibration which was in use when the contaminant mass frequency was determined. By comparing the ratio of the frequencies of the contaminant ion and the reference ion it is possible to determine the mass of the contaminant using the mass of the reference species. The reference species is entered using the Mass Measure convention N(El)A, where N is the number of atoms of one specific element, El is the elemental abbreviation (caps sensitive) and A is the atomic number. Elemental entries are separated by a colon. For example, if H_2O was the reference then in the species edit the user would enter 2H1:1O16. If the entry is valid then a formatted string will appear in the bottom of the *Reference Mass* sub-area displaying the nuclides' information. In the frequency edit the user enters the cyclotron frequency of the reference species. The charge box is used to select the charge state of the reference species.

The *Contaminant Mass* sub-area is used to enter information concerning the contaminant ion that the user would like to determine. In the frequency edit the user enters the cyclotron frequency of the unknown ion. The uncertainty in the frequency is then entered into the uncertainty edit.

The *Search Options* sub-area is where the search parameters are set. The element max box sets the maximum number of unique elements to be searched for and currently has a 5 element hard-coded limit. The multi-max box is used to the the maximum N value for each element in the search. If the user would like to add unstable isotopes to the search then they would check the unstable check box and enter the minimum half life for the isotope that they would like included. If the user would also like to search for multiply charged isotopes then they would check the multi-charge check box and set the minimum and maximum charge states to be searched. Note that the more options which are used will increase the time to complete the search.

The *Elements* sub-area determines the elemental species which will be included in the search. Upon opening the program all elements are chosen. Removing a check next to the element will remove it from the search. This applies to any unstable isotopes if they are included. The clear button removes all checks and the select all button applies checks to all elements. It is possible to save and load a set of elements. The *Save Elements* action in the *File* menu will write the checked elements to the element_names.txt file mentioned previously. The *Load Elements* action will reload the saved elements.

At the bottom of the main window are two buttons, *Generate List* and *RUN*!. The *Generate List* button list populates a list of searchable isotopes based on the search options settings and the checked elements. The *RUN*! button starts the search. One does not need to use the *Generate List* button previous to running the search, but doing so allows manual exclusion of individual isotopes and will be described in the next subsection.

C.2.2 The isotope list window

After the *Generate List* button in the *Main Window* has been pressed the *Isotope List Window* (Fig. C.2) displays all the isotopes to be used in the search, along with its half life and mass excess. To exclude individual isotopes in the list from the search simply highlight the row which contains its information. To include it in the search again, deselect the row.

C.2.3 The results window

After the *RUN*! button on the *MainWindow* has been pressed the matches appear in the *Results Window* (Fig. C.3). Since the search algorithm and the GUI run on separate threads the GUI is able to sort the matches as they're found. They are listed in descending order of distance from the cyclotron frequency of the contaminant ion

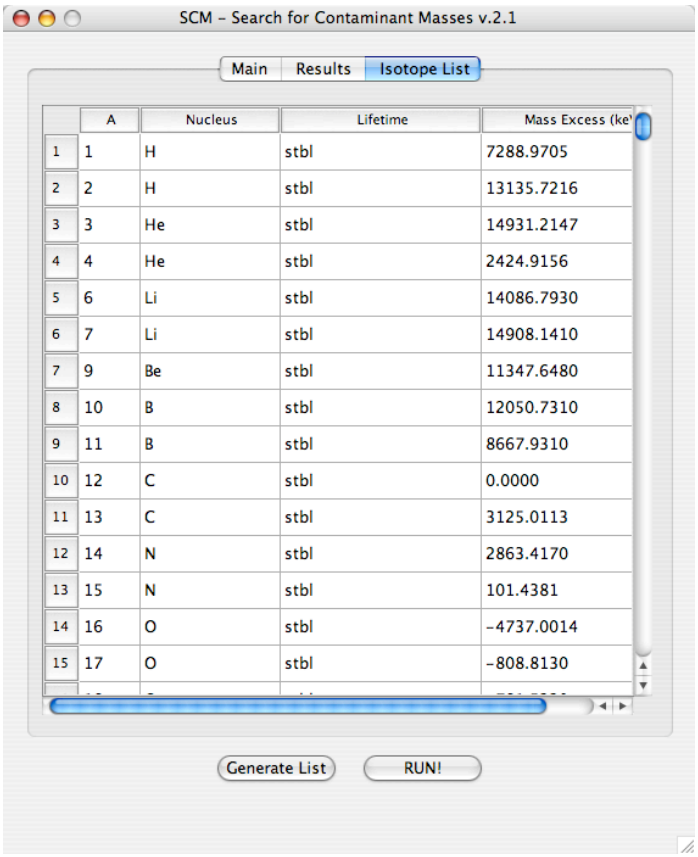

Figure C.2. The SCM_Qt *Isotope Window* which lists the isotopes to be used in the search.

specified in the *Contaminant Mass* sub-area on the *Main Window*. The matches are named using the Eva/Mass Measure convention so they can be copied and pasted into Mass Measure for cleaning, if necessary.

C.3 Additional Tools

C.3.1 The mass fragment calculator

The *Mass Fragment Calculator* (Fig. C.4) is used to determine what molecules are possible within a specified mass region. The user enters in a mass and tolerance, in amu, and presses the *RUN*! button on the *Mass Fragment Calculator Window* to

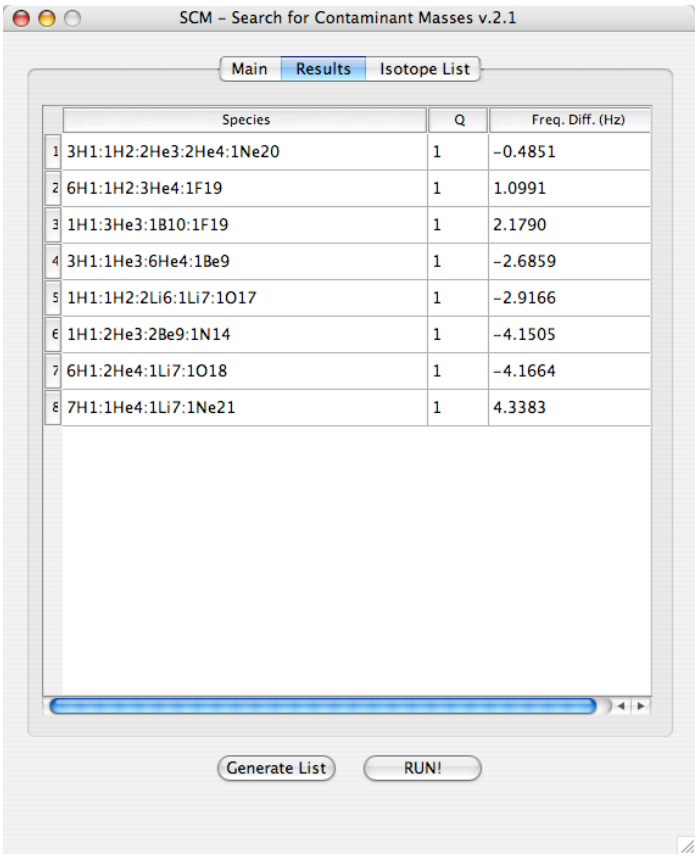

Figure C.3. The SCM_Qt *Results Window* which lists the matches generated by the search algorithm using the specified search parameters.

generate a list of molecules. The search options are specified in the *Main Window*, as covered previously. The same rules apply to isotope list generation and exclusion. It is a good idea to keep the isotope list as small as possible to reduce the total number of combinations returned.

C.3.2 The frequency separation window

The *Frequency Separation Window* (Fig. C.5) is used to calculate the difference in the cyclotron frequencies, and mass in keV, of two species. The first species used is that which appears in the *Reference Mass* sub-area in the *Main Window*, and is also shown in the *Reference Species* sub-area in the *Frequency Separation Window*.

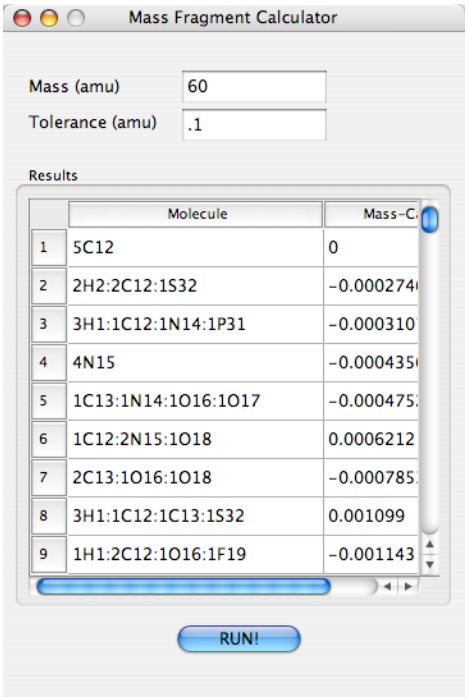

Figure C.4. The SCM_Qt *Mass Fragment Calculator Window* calculates which molecules fall within a given mass range.

The other species is entered in the line edit in the *Measurement Species* sub-area. If a valid string is entered then the *Calculate* button will be enabled and pressing it will calculate the results.

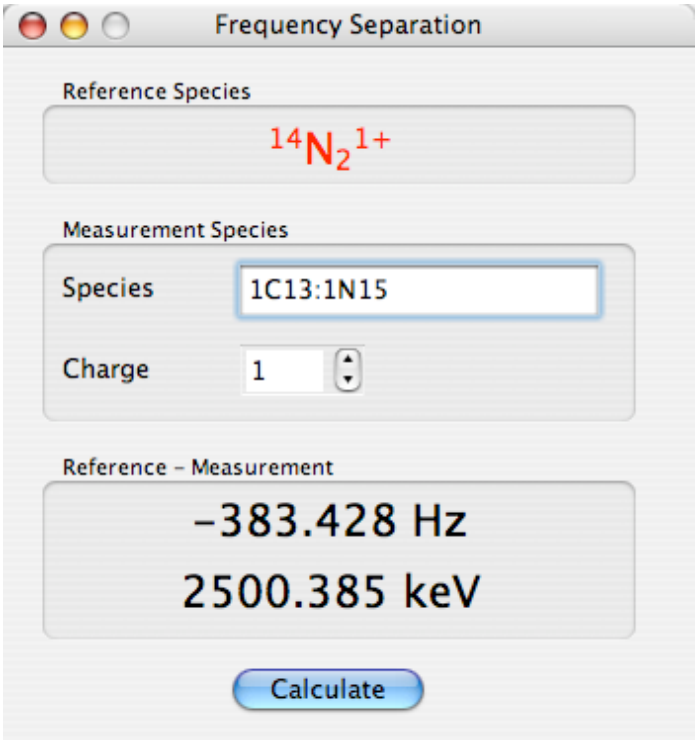

Figure C.5. The SCM_Qt *Frequency Separation Window* which calculates the difference in the cyclotron frequencies between two species, as well as the energy separation.

APPENDIX D

Fit procedure to minimize higher-order electric field terms

The optimum voltages to be applied to the Penning trap electrodes are found by a fitting routine. It is a variant of the traditional χ^2 fitting routine [77] where a variable function is fit to a data set. Here we have data sets which correspond to the potentials along the trap axis from each electrode pair with 1 V applied. Each data set can be multiplied by an arbitrary factor corresponding to an applied voltage. The total potential along the trap axis for any given point is

$$V(z_i) = \sum_{k=1}^{4} a_k X_k(z_i), \tag{D.1}$$

where X_k are the SIMION potentials and a_k are the unknown scaling factors. A perfect electric quadrupole field would be purely quadratic along the trap axis. So the unknown scaling factors must be determined such that data is fit to a quadratic function.

To begin, a pure quadratic function is given by

$$y = \frac{z^2}{z_o^2} + c, \ for \ z \leq z_o \tag{D.2}$$

The normal definition of χ^2 is:

$$\chi^2 = \sum_{i=1}^{N} \left(y_i - \sum_{k=1}^{4} a_k X_k(z_i) \right)^2 \tag{D.3}$$

where y_i are curve fit points. The first sum is over each value of z, and the second sum is over the unknown potentials. The best fit is that which minimizes Eq. D.3. This is found by solving

$$0 = \frac{\partial}{\partial a_k}\chi^2 = \sum_{i=1}^{N} \left[y_i - \sum_{j=1}^{4} a_j X_j(z_i) \right] X_k(x_i) \tag{D.4}$$

Now we let $A_{ij} = X_j(z_i)$, $b_i = y_i$ and $\mathbf{a} = (a_1,a_2,a_3,a_4)$. Substituting these back into Eq. D.4 yields

$$0 = \sum_{i=1}^{N} \left[y_i X_k(z_i) - \sum_{j=1}^{4} a_j X_j(z_i) X_k(z_i) \right] = A^T - (A^T \cdot A) \cdot a \tag{D.5}$$

We can then solve for a and obtain

$$a = \left(A^T \cdot A \right)^{-1} \cdot \left(A^T \cdot b \right) \tag{D.6}$$

Provided that the inverse exists we have a method for calculating the optimum electrode potentials.

BIBLIOGRAPHY

BIBLIOGRAPHY

[1] J. Hardy, I. Towner, Phys. Rev. C. 71 (2005) 055501.

[2] G. Audi, A. H. Wapstra, C. Thibault, Nucl. Phys. A 729 (2003) 129.

[3] M. König, G. Bollen, H.-J. Kluge, T. Otto, J. Szerypo, Int. J. Mass Spec. Ion. Proc. 142 (1995) 95.

[4] M. Bradley, J. Porto, S. Rainville, J. Thompson, D. Pritchard, Phys. Rev. Lett. 83 (1999) 4510.

[5] C. Thibault, R. Klapisch, C. Rigaud, A. M. Poskanzer, R. Prieels, W. Reisdorf, Phys. Rev. C 12 (1975) 644.

[6] P. Hansen, A. Jensen, B. Jonson, Annu. Rev. Nucl. Part. Sci. 45 (591).

[7] C. Bachelet, G. Audi, C. Gaulard, C. Guénaut, F. Herfurth, D. Lunney, M. De Saint Simon, C. Thibault, Eur. Phys. J. A S1 (2005) 31.

[8] W. Satula, D. J. Dean, J. Gary, S. Mizutori, W. Nazarewicz, Phys. Lett. B 407(2) (2000) 103.

[9] P. Schury, Ph.D dissertation, Ph.D. thesis, Michigan State University (2007).

[10] W. O. Milligan (Ed.), Proceedings of the Robert A. Welch Foundation Conference on Chemical Research, 1957.

[11] T. Sun, High precision mass measurement of ^{37}Ca and developments for LEBIT, Ph.D. thesis, Michigan State University (2006).

[12] E. Burbidge, G. Burbidge, F. Fowler, F. Hoyle, Rev. Mod. Phys. 29 (1957) 547.

[13] A. Cameron, Annu. Rev. Nucl. Sci. 8 (1957) 299.

[14] R. K. Wallace, S. E. Woosley, Astrophys. Jour. Supp. 45 (1981) 389.

[15] D. Lunney, J. Pearson, C. Thibault, Rev. Mod. Phys. 75 (2003) 1021.

[16] A. Kjellberg, G. Rudstam (Eds.), The ISOLDE isotope separator facility at CERN, CERN 70-3, 1970.

[17] S. Hofmann, G. Münzenberg, Rev. Mod. Phys. 72 (2000) 733.

[18] P. Dendooven, Nucl. Instr. and Meth. in Phys. Res. B 126 (1997) 182.

[19] R. Klapisch, R. Prieels, C. Thibault, A. M. Poskanzer, C. Rigaud, E. Roeckl, Phys. Rev. Lett. 31 (1973) 118.

[20] D. M. Moltz, K. S. Toth, R. E. Tribble, R. E. Neese, J. P. Sullivan, Phys. Rev. C 26.

[21] H. Savajols, Hyperfine Int. 132 (2001) 243.

[22] J. M. Wouters, D. J. Vieira, H. Wollnick, G. W. Butler, R. H. Kraus, K. Vaziri, Nucl. Instr. and Meth. B 26 (1987) 286.

[23] D. Bazin, J. A. Caggiano, B. M. Sherrill, J. Yurkon, A. Zeller, Nucl. Instr. and Meth. in Phys. Res. B 204 (2000) 629.

[24] M. Matos, in: A. Woehr, A. Aprahamian (Eds.), Proceedings of the 12th International Symposium on Capture Gamma-Ray Spectroscopy and Related Topics, AIP, 2006, p. 164.

[25] A. S. Lalleman, G. Auger, W. Mittig, M. Chabert, M. Chartier, J. Fermé, A. Gillbert, A. Lépine-Szily, M. Lewitowicz, M. H. Moscatello, N. A. Orr, G. Politi, F. Sarazin, H. Savajols, P. Van Isacker, A. C. C. Villari, Hyperfine Int. 132 (2001) 313.

[26] S. Issmer, M. Fruneau, J. A. Pinston, M. Ashgar, D. Barnéoud, J. Genevey, T. Kerscher, K. E. G. Löbner, Eur. Phys. J. A 2 (1998) 173.

[27] J. Stadlmann, M. Hausmann, F. Attallah, K. Beckert, P. Beller, F. Bosch, H. Eickhoff, M. Falch, B. Franczak, B. Franzke, Phys. Lett. B 586 (2004) 27.

[28] B. Schlitt, K. Beckert, T. Beha, H. Eickhoff, B. Franzke, H. Geissel, H. Irnich, H. C. Jung, T. F. Kerscher, O. Klepper, K. E. G. Löbner, G. Münzenberg, F. Nolden, Y. Novikov, T. Radon, H. Reick, A. Schwinn, M. Steck, T. Sümmerer, Winkler, H. Wollnick, Hyperfine Int. 99 (1996) 117.

[29] G. Bollen, D. Davies, M. Facina, J. Huikari, E. Kwan, P. A. Lofy, D. J. Morrissey, A. Prinke, R. Ringle, J. Savory, P. Schury, S. Schwarz, C. Sumithrarachchi, T. Sun, L. Weissman, Phys. Rev. Lett. 96 (2006) 152501.

[30] A. Kellerbauer, K. Blaum, G. Bollen, F. Herfurth, H.-J. Kluge, M. Kuckein, E. Sauvan, C. Scheidenberger, L. Schweikhard, Eur. Phys. J. D 22 (2003) 53.

[31] G. Bollen, S. Becker, H.-J. Kluge, M. König, R. Moore, T. Otto, H. Raimbault-Hartmann, G. Savard, L. Schweikhard, H. Stolzenberg, Nucl. Instrum. Methods A 368 (1996) 675.

[32] V. S. Kolhinen, T. Eronen, J. Hakala, A. Jokinen, S. Kopecky, S. Rinta-Antila, J. Szerypo, J. Äystö, Nucl. Instrum and Methods in Phys. Res. B 204 (2003) 502.

[33] G. Savard, R. C. Barber, D. Beeching, F. Buchinger, J. E. Crawford, S. Gulick, X. Feng, E. Hagberg, J. Hardy, V. T. Koslowsky, J. K. P. Lee, R. Moore, K. S. Sharma, M. Watson, Nucl. Phys. A 368 (1997) 353.

[34] G. Sikler, D. Ackermann, G. Bollen, F. Attallah, D. Beck, J. Dilling, S. A. Eliseev, H. Geissel, D. Habs, S. Heinz, F. Herfurth, Nucl. Instr. and Meth. B 204 (2002) 482.

[35] D. Morrissey, B. Sherrill, A. Stolz, I. Wiedenhoever, Nucl. Instr. and Meth. B204 (2003) 90.

[36] L. Weissman, D. J. Morrissey, G. Bollen, D. Davies, E. Kwan, P. A. Lofy, P. Schury, S. Schwarz, C. Sumithrarachchi, T. Sun, R. Ringle, Nucl. Instr. and Meth. A540 (2005) 245.

[37] T. Sun, S. Schwarz, G. Bollen, D. Lawton, R. Ringle, P. Schury, Eur. Phys. J. A 25(S1) (2005) 61.

[38] G. Bollen, S. Schwarz, D. Davies, P. Lofy, D. Morrissey, R. Ringle, P. Schury, T. Sun, L. Weissman, Nucl. Instr. and Meth. A 532 (2004) 203.

[39] R. Moore, G. Rouleau, J. Mod. Optics 39 (1992) 361.

[40] S. Schwarz, Nucl. Instr. and Meth. A 566 (2006) 233.

[41] L. Brown, G. Gabrielse, Rev. Mod. Phys. 58 (1986) 233.

[42] G. Bollen, R. Moore, G. Savard, H. Stolzenberg, J. Appl. Phys. 68 (1990) 4355.

[43] H. Raimbault-Hartmann, D. Beck, G. Bollen, M. König, H.-J. Kluge, E. Schark, J. Stein, S. Schwarz, J. Szerypo, Nucl. Instr. and Meth. B 126 (1998) 378.

[44] G. Gräff, H. Kalinowsky, J. Traut, Z. Phys. A297 (1980) 35.

[45] G. Bollen, H.-J. Kluge, T. Otto, G. Savard, L. Schweikhard, H. Stolzenberg, G. Audi, R. Moore, G. Rouleau, J. Mod. Optics 39 (1992) 257.

[46] G. Gabrielse, J. Tan, J. Appl. Phys. 63 (1988) 5143.

[47] N. Daly, Rev. Sci. Instrum. 31 (1960) 264.

[48] S. Schwarz, Aufbau und test einer laserdesorptionsquelle für das cern-massenexperiment, Ph.D. thesis, University of Mainz (1993).

[49] W. H. Press, S. A. Teukolsky, W. T. Vetterling, B. P. Flannery, Numerical Recipes in C++: The Art of Scientific Computing, Cambridge University Press, 2002.

[50] D. Dahl, Int. J. Mass Spec. 200 (2000) 3.

[51] R. Ringle, G. Bollen, P. Schury, S. Schwarz, T. Sun, Int. J. Mass Spec. in publication.

[52] J. Dilling, R. Baartman, P. Bricault, M. Brodeur, L. Blomeley, F. Buchinger, J. Crawford, J. Crespo López-Urrutia, P. Delheij, M. Froese, G. Gwinner, Z. Ke, J. K. P. Lee, R. Moore, V. Ryjkov, G. Sikler, M. Smith, J. Ullrich, J. Vaz, Int. J. Mass Spec. 251 (2006) 198.

[53] I. Bergström, C. Carlberg, T. Fritioff, G. Douysset, J. Schonfelder, R. Schuch, Nucl. Instrum. Methods A 487 (2002) 618.

[54] R. Ringle, P. Schury, T. Sun, G. Bollen, D. Davies, J. Huikari, E. Kwan, D. Morrissey, A. Prinke, J. Savory, S. Schwarz, C. Sumithrarachchi, Int. J. Mass Spec. 251 (2-3) (2006) 300.

[55] R. Firestone, R. Lindstrom, G. Molnar, S. Mughabghab, A. Reddy, Z. Revay, V. Tan, C. Zhou, R. Paviotti-Corcuera, IAEA-Tecdoc.

[56] L. Langer, E. Spejewski, D. Wortman, Phys. Rev. B 133 (1964) 1145.

[57] H. Booij, E. Van Hoek, H. Van der Molen, W. Slot, J. Blok, J. Borggreen, E. Hyde, Nuc. Phys. A 160 (1971) 337.

[58] R. Ries, R. Damerow, W. Johnson Jr., Phys. Rev. 132 (1963) 1662.

[59] W. Shi, M. Redshaw, E. Meyers, Phys. Rev. A 72 (2005) 022510.

[60] P. Delahaye et al., ISOLTRAP Collaboration, (2006) in preparation.

[61] K. Blaum, G. Audi, D. Beck, G. Bollen, F. Herfurth, A. Kellerbauer, H.-J. Kluge, E. Sauvan, S. Schwarz, Phys. Rev. Lett. 91 (260801).

[62] M. Mukherjee, A. Kellerbauer, D. Beck, K. Blaum, G. Bollen, F. Carrel, P. Delahaye, J. Dilling, S. George, C. Guénaut, F. Herfurth, A. Herlert, H.-J. Kluge, U. Köster, D. Lunney, S. Schwarz, L. Schweikhard, C. Yazidjian, Phys. Rev. Lett. 93 (2004) 150801.

[63] G. Savard, J. A. Clark, F. Buchinger, J. E. Crawford, S. Gulick, J. C. Hardy, A. A. Hecht, V. E. Iacob, J. K. P. Lee, A. F. Levand, F. Lundgren, N. D. Scielzo, K. S. Sharma, I. Tanihata, I. S. Towner, W. Trimble, J. C. Wang, Y. Wang, Z. Zhou, Phys. Rev. C 70 (2004) 042501.

[64] F. Herfurth, J. Dilling, A. Kellerbauer, G. Audi, D. Beck, G. Bollen, H.-J. Kluge, D. Lunney, R. Moore, C. Scheidenberger, S. Schwarz, G. Sikler, J. Szerypo, Phys. Rev. Lett. 87 (2001) 142501.

[65] A. Kellerbauer, G. Audi, D. Beck, K. Blaum, G. Bollen, B. A. Brown, P. Delahaye, C. Guénaut, F. Herfurth, H.-J. Kluge, D. Lunney, S. Schwarz, L. Schweikhard, C. Yazidjian, Phys. Rev. Lett. 93 (2004) 072502.

[66] G. Savard, F. Buchinger, J. A. Clark, J. E. Crawford, S. Gulick, J. C. Hardy, A. A. Hecht, J. K. P. Lee, A. F. Levand, N. D. Scielzo, H. Sharma, K. S. Sharma, I. Tanihata, A. C. C. Villari, Y. Wang, Phys. Rev. Lett. 95 (2005) 102501.

[67] T. Eronen, V. Elomaa, U. Hager, J. Hakala, A. Jokinen, A. Kankainen, I. Moore, H. Penttilä, S. Rahaman, J. Rissanen, A. Saastamoinen, J. Äystö, J. C. Hardy, V. S. Kolhinen, Phys. Rev. Lett.

[68] D. R. Lide (Ed.), CRC Handbook of Chemistry and Physics, CRC Press, 2006.

[69] S. Brunner, T. Engel, G. Werth, Meas. Sci. Technol. 6 (1995) 222.

[70] R. S. Van Dyck Jr., D. L. Farnham, S. L. Zafonte, P. B. Schwinberg, Rev. Sci. Instrum. 70 (3) (1999) 1665.

[71] G. Bollen, H.-J. Kluge, M. König, T. Otto, G. Savard, H. Stolzenberg, R. Moore, G. Rouleau, G. Audi, Phys. Rev. C 46 (R2140).

[72] J. Melin, J. V. Ortiz, I. Martin, A. M. Velasco, C. Lavin, J. Chem. Phys. 122 (2005) 234417.

[73] J. C. Hardy, private communication.

[74] B. Blank, private communication.

[75] S. George, private communication.

[76] R. T. Birge, Phys. Rev. 40 (1932) 207.

[77] P. R. Bevington, D. K. Robinson, Data Reduction and Error Analysis for the Physical Sciences, McGraw Hill, 2003.

[78] G. Audi, O. Bersillon, J. Blachot, A. H. Wapstra, Nucl. Phys. A 729 (2003) 3.